# IONS NEAR CURVED OIL-WATER INTERFACES: TOWARDS A MICROSCOPIC THEORY FOR PICKERING EMULSIONS

J. de Graaf

June 20, 2008

Universiteit Utrecht

Master's Thesis
Institute for Theoretical Physics
Utrecht University
Supervisor: dr. R. van Roij

# Contents

# Prologue

Emulsions of water droplets in oil or oil droplets in water play a key role in many aspects of life. One only needs to think of such every day items as milk, lipstick and hair conditioner, to name but a few. These oil-water emulsions are characterised by a tendency to demix. The small droplets in the emulsion coalesce into larger droplets, driven by a need to minimise the oil-water interface. Eventually, the system separates into an oil phase and a water phase, with a single contact-layer. The wide-spread use of emulsions in the food, cosmetics and health industries and the desire of these industries to have stable emulsions, has been a driving force in research. In 1907 Pickering discovered that droplet coalescence could be postponed by introducing colloidal particles into the emulsion [1]. Colloidal particles are mesoscopic particles, i.e. they are larger than most molecules, but still small enough to experience Brownian motion. Colloids adsorb to the oil-water interface in these so-called Pickering Emulsions, reducing the oil-water contact and thus the tendency to demix. These emulsions are known to eventually phase-separate though. Therefore, other stabilising factors, called surfactants, are used to create stable emulsions. Use of surfactants dominates todays industrial emulsion processes.

However, recent experimental work performed in Utrecht by the groups of prof. Kegel [2] and prof. Van Blaaderen [3], has prompted renewed interest in the behaviour of Pickering Emulsions [4, 5]. It has been observed that certain Pickering Emulsions are thermodynamically stable [2], i.e. they do *not* have a tendency to demix. Furthermore, it is suggested that by adding certain salts and homogeneously charged colloids to a phase-separated system of oil and water, spontaneous emulsification will occur [6]. This is in stark contrast with the established belief that thermodynamic stability and spontaneous emulsification are not possible for Pickering Emulsions. In this thesis we will investigate, using the tools of modern statistical mechanics, several of the aforementioned experimental results. Starting form the meta-stable case of oil-water emulsions with only salt added, we will expand our investigation to cover these thermodynamically stable Pickering Emulsions and their spontaneous emulsification.

As said, the first part of this thesis covers saline emulsions. These systems are related to the experiments described in Ref. [3], where the water droplets in certain water-oil emulsions appear to form (meta-)stable crystalline structures. The the work of Bier and Zwanikken, Ref. [7], lays the theoretical foundation for the description of such systems in the so-called planar geometry. From this planar case we extend the results to droplets in the spherical geometry and quantify the effects of curvature and finite droplet packing-fraction. We also consider crystal formation and it will be shown that the observed stability in Ref. [3] is not a thermodynamical stability in the strict sense of the word.

The second part of the thesis builds on the knowledge and insight gained in the first part. Here we will add colloids to a saline emulsion of spherical droplets, in the hope of understanding from a microscopic picture the behaviour observed in Refs. [2, 3, 6]. It should be noted that in the experiments described in these papers two essentially different types of Pickering Emulsion are studied. In Ref. [3] 1-2 $\mu$m sized colloids are considered, which absorb to the curved oil-water interfaces and have a finite colloid density in the oil bulk phase. In this bulk phase a colloidal crystal is formed, which is separated form the oil-water interface by a large colloid-free exclusion zone. In Refs. [2, 6] 10-25 nm sized colloids were used, which are all absorbed at the interface of the emulsion, i.e. there are no free colloids.

A theoretical model describing the emulsions of Ref. [3] has been formulated in the planar geometry [5]. We will extend this model to include the effects of curvature. We will also formulate a model to describe the results of Refs. [2, 6] in the spherical geometry. This model will have remarkable similarity to that used to describe saline emulsions, and it will have a range of applicability which extends beyond that of Pickering Emulsions. Since the droplet size in the emulsions of Refs. [2, 6] is of the order of 100-250 nm, we believe that curvature will be an essential ingredient in formulating an accurate theoretical description. We will not go into the results one can obtain by numerically solving the equations in the aforementioned models, however, simply because there was not enough time to treat both saline emulsions and Pickering Emulsions in depth.

It is a pleasure to thank the following people for having contributed to the final form of this Master's Thesis. First and foremost my supervisor dr. René van Roij, who guided my thesis research. He often aided me by lending his expertise to give insight in the physical processes, which underlie the results obtained by studying the mathematical properties of the model. I would also like to thank him for proof-reading on more than one occasion the sizeable amount of text and results which constitute this thesis and for the helpful suggestions he made to improve its quality. Secondly, I would like to thank dr. Markus Bier and drs. Jos Zwanikken, for their contribution to my understanding of the behaviour of emulsions in the planar approximation; their assistance in setting up numerical schemes, programming in the C++ language and producing Gnuplot graphs; and investing quite a bit of their time. Finally, I would like to extend my gratitude towards dr. Miriam Leunissen, dr. Stefano Sacanna and prof. Willem Kegel for allowing me to reproduce some of the graphs from their respective publications in this thesis.

# Part I

# Saline Emulsions

# Chapter 1

# Introduction

In this part we will treat saline emulsions of oil and water in the spherical geometry, i.e. spherical droplets of one medium in a continuum of the other. We do so in order to gain understanding of the systems described in Ref. [3], which reports the experimental findings concerning charge-stabilised additive free emulsions of water droplets in oil, in this case CHB, cyclohexyl bromide, see fig. 1.1.

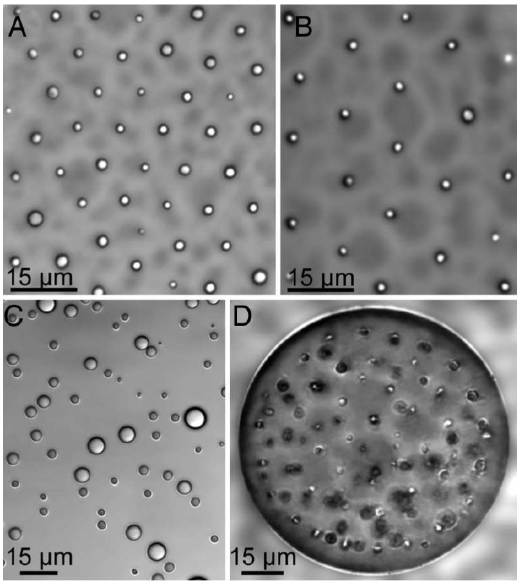

**Figure 1.1:** *Bright-field transmission images of charge-stabilised, additive-free emulsions. (A and B) Water droplets in CHB (A) and CHB-decalin (B) after 2 min of sonication, near the top wall of the sample cell (this is one layer of the 3D crystal). (C) CHB droplets in water, near the bottom of the sample cell. (D) Wigner crystal of small water droplets inside a bigger CHB droplet (in water). Note that curvature effects distort the image and that some droplets are not in focus.* Reproduced from Ref. [3] with the author's permission.

In fig. 1.1 A & B, the repulsive interactions, induced by the preferential partitioning of the stabilising ions are sufficiently long range to cause crystal formation. The salt concentration in the water droplets and the oil medium is unknown. Self-dissociation of the CHB imposes the ion density in oil, but it is subsequently modified by ion drainage from the oil into the water. There is no experimental data on these concentrations. The relative dielectric constant of the CHB is approximately 5.6, although stable droplet arrays were observed for oils with relative dielectric constant between 4 and 10. The ions which charge-stabilise the emulsion are $H^+$ and $Br^-$, with ionic radius in water of 2.8 Å and 3.0 Å respectively as estimated in Ref. [8]. These ions originate from the partial dissociation of the HBr decomposition product of CHB. The droplet radius is in the order of 1 $\mu$m, although there is a large polydispersity with radii up to 1.5 $\mu$m, and the observed inter-droplet separation is roughly 10.0 $\mu$m. Therefore, the droplet volume fraction in this Wigner crystal is roughly 0.001.

In the upcoming chapters we set up a Density Functional Theory to model the saline emulsions of Ref. [3]. In the formulation of this model we include the difference in dielectric constant between oil and water and the difference in ion size between $H^+$ and $Br^-$ to describe the preferential partitioning of ions. We do so by considering the Born self-energy of these ions in oil and in water and use the difference in self-energy between the two media as a measure for ion drainage into the water. Since both species of ion have a different size, their self-energies will be different, this will be the underlying mechanism of preferential partitioning. A consequence of this partitioning is the formation of an ionic double-layer around the oil-water interface and the self-charging of the water and oil. These charged water droplets in oil interact such that the repulsive inter-droplet potential can prevent coalescence and can even be sufficiently strong and long-range to cause crystallisation. All of these effects will follow from/be included in the Grand Potential Functional by which we will model generic saline oil-in-water and water-in-oil emulsions. From the Grand Potential we derive the Poisson-Boltzmann Equation for these systems, which can be solved for given system parameters to yield the electrostatic properties of the emulsion, including the charge, the excess surface tension and the plasma-parameter, as introduced in Refs. [9, 10].

Using the theoretical and analytical tools at our disposal, these emulsive systems will be analysed by means of a planar limit approximation and a numerical solution to the Poisson Equation in the spherical geometry. The results we obtain in spherical geometry will be compared to those in the planar geometry, which had previously been used to calculate physical quantities for such emulsions. We will show that curvature significantly modifies these quantities with respect to those calculated for a flat interface, justifying our two-part approach. We will study the effect of such curvature and derive a means by which we can quantify it. Planar and spherical systems can to an extent be related to each other via a polynomial expansion in terms of the inverse droplet radius and the Debye length in oil. We will examine the range of validity of this expansion and the way in which it can be used to clarify the results we obtain in the spherical geometry. The planar limit will prove useful as a means to analyse the system in certain regimes, whereas the full spherically geometric calculation has other ranges of application. The polynomial expansion we present attempts to find the middle ground between the relative ease of calculations in the planar geometry and the precision of the spherical geometry.

The effects of curvature for finite droplets in finite Wigner-Seitz cells will prove quite dramatic, especially when we consider the plasma parameter and the system's ability to crystallise. Our focus will lie with the effects which are not explained by the planar theory. We will improve upon the knowledge of crystallisation as presented in Ref. [5] and go into the differences with the spherical geometry. It turns out that the observations in Ref. [3] can be explained by examining the plasma-parameter. Furthermore, our results show that such crystallisation is not easily achieved, which explains why this phenomena was only recently observed. We will also show that the crystals which were found are not thermodynamically stable even though they are reported to remain unchanged over a period of many months. The observed crystals are predicted to be merely meta-stable. To determine their stability we have used the excess or ionic surface tension as a measure of the thermodynamic properties of the system. Although this investigation of the properties of saline oil-water emulsions is quite exhaustive, it has by no means covered all possibilities. At the end of part I we will have gained enough insight in the behaviour of saline emulsions to use as a stepping stone for the formulation of theoretical models used to describe Pickering Emulsions in the second part of the thesis.

# Chapter 2

# Theoretical Foundation

## 2.1 Approach

In this chapter, we describe the statistical mechanical background required to treat saline oil-water (OW) and water-oil (WO) emulsions. We begin with a characterisation of the Wigner-Seitz approximation scheme. Then we determine the Grand Potential for such systems by means of Density Functional Theory (DFT). From it we derive the Poisson-Boltzmann Equation, which describes the electrostatic potential in a mean field approximation. By solving the Poisson Equation we can ascertain the behaviour of these emulsive systems. Unfortunately the Poisson Equation with the boundary conditions for this system cannot be solved analytically in general. In the following chapters we study it using various approximation techniques.

## 2.2 Wigner-Seitz Cell Model for Emulsions

We are interested in the behaviour of OW and WO emulsions with (monovalent) anions and cations. These emulsions are characterised by droplets of water in an oil medium or oil droplets in a water medium. We consider an emulsion of total volume $V$ containing $N$ droplets with average radius $a$ and average inter droplet distance $R$, as measured from the centre-of-mass. The droplets are therefore typically separated by surface-surface distance $R - 2a$. These saline emulsions are four component mixtures of water molecules, oil molecules and ions as illustrated in fig. 2.1. Note that the picture is not to scale, since the size asymmetry between the various molecules and ions can be much more extreme than depicted.

It is impossible to perform calculations to describe the macroscopic emulsion phenomena based on a fully molecular approach. We therefore require two methods of simplification in order to reduce the complexity of the problem to more manageable proportions, namely coarse-graining and the cell model. We coarse-grain both media, i.e. oil and water, and the ionic degrees of freedom. That is to say, that we no longer keep track of the position and motion of each individual constituent of the emulsion, instead we consider their density profiles. The media are considered to be incompressible linear dielectrics, which means that the solvent background can be characterised by its dielectric constant alone. The ions undergo another level of coarse-graining, they are described by density profiles $\rho_{\pm}(\mathbf{r})$, which are position dependent. We thus

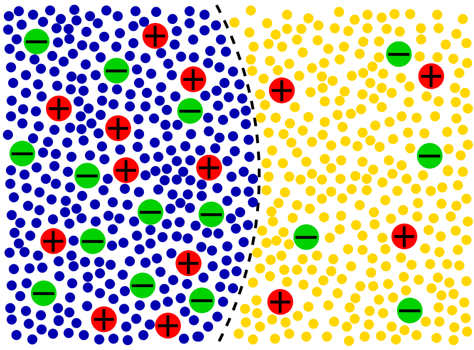

**Figure 2.1:** A graphical representation of a four-component WO emulsion with ions. The oil molecules are indicated in yellow, the water molecules in blue and the ions have been labelled with plus and minus signs. Note that this is the molecular picture and not the coarse-grained model we will be working with. The oil-water interface has been represented with a dashed line. We will see below that a higher concentration of ions is to be expected in water compared to oil.

have a $N$-droplet problem with unknown ionic density profiles and $N \gg 1$. In the Wigner-Seitz cell approximation scheme the character of the problem (fig. 2.2a) is retained at the expense of replacing the multi-centred droplet system by a spherically symmetric problem for a single droplet (fig. 2.2d). The full emulsion (fig. 2.2a) is partitioned into charge neutral Wigner-cells (fig. 2.2b), which are conveniently symmetrised (fig. 2.2c). Under the assumption that the emulsion is sufficiently 'homogeneous', we may restrict our attention to one cell and the ion distribution within (fig. 2.2d). In this thesis we consider a Wigner cell with radius $R$, centred around a droplet with radius $a$, such that we have the droplet volume $V_d = 4\pi a^3 N/3$ and the total volume $V = 4\pi R^3 N/3$. Thus, the droplet fraction in the spherical system is given by $x \equiv (a/R)^3$, whereas the droplet-to-medium volume ratio is $a^3 : (R^3 - a^3)$.

Note that by the spherical nature of the problem and hence the Wigner-cell, we may write the ion distributions in a single cell as $\rho_\pm(r)$, with $r$ the radial distance from the midpoint of the cell. The equilibrium ionic profiles are governed by Coulombic interactions only. Inter-ionic interactions depend on the charge and the electric field, whereas the presence of the media is taken into account via the self-energy of the ions. This self-energy is also Coulombic in nature and only medium dependent. For the emulsive systems studied here it will enter the DFT through the external potential term in the Grand Potential Functional. Note that there are no hard-core interactions in this part, the ions are considered point-like and the droplets will coalesce when they come into contact.

## 2.3 The Solvent Induced External Potential for Ions

### 2.3.1 The Born Self-Energy

The task at hand is to find an explicit expression for the Grand Potential of the ions in these emulsive systems. To make this more general, the theory we will set up below is valid for generic emulsions. The droplet, referred to as **(area 1)**, has relative electric permittivity $\epsilon_1$, whereas the medium, **(area 2)**, has relative electric permittivity $\epsilon_2$. The relative permittivity of the

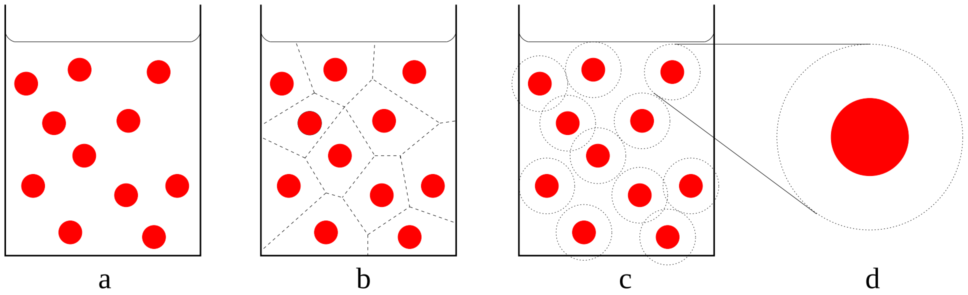

**Figure 2.2:** The Wigner-Seitz Cell approximation scheme for an OW or a WO system. The ions are not shown in this picture and the solutes have been coarse-grained.

water is denoted by $\epsilon_w$ and that of the oil is $\epsilon_o$. Let $a$ be the radius of the droplet and $R$ be the radius of the Wigner-Seitz cell, which is spherically symmetric in this case, see fig. 2.3. The oil-water interface is located at $r = a$.

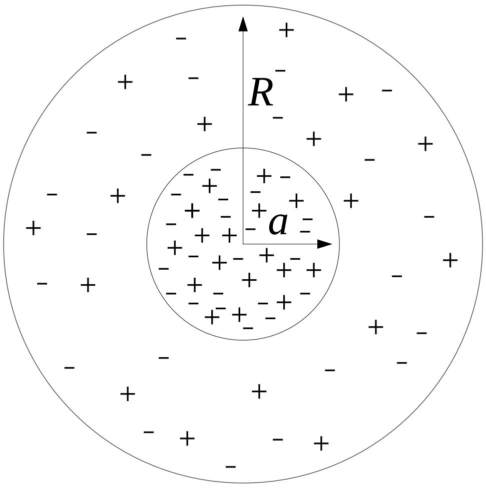

**Figure 2.3:** The spherically approximated Wigner-Seitz cell, with positive and negative ions. Henceforth, $a$ is the radius of the droplet and $R$ is the radius of the cell.

We have cations and anions with valencies $q_\pm = \pm 1$ and ionic radii $a_\pm$. The dielectric constant of vacuum is given by $\epsilon_v$. We now introduce a step-function, which we assume to describe the dielectric properties the whole Wigner-cell

$$\epsilon(r) = \begin{cases} \epsilon_1 & \text{if } 0 < r < a; \\ \epsilon_2 & \text{if } a < r < R, \end{cases}$$

where $(\epsilon_1, \epsilon_2)$ is $(\epsilon_w, \epsilon_o)$ and $(\epsilon_o, \epsilon_w)$ for a WO and an OW emulsion respectively. Note that all functions here have only radial dependence, because of the spherical symmetry of the problem.

Ions have a much higher solubility in water than in oil. To differentiate between the two media in a Density Functional approach, we introduce an external potential on the ions as induced by the solvent. We say there is a difference in the self-energies of the ions in water w.r.t. the energies of the ions in oil. An ion in water will generally have a lower self-energy than one in oil. We take the difference of the two self-energies and call them $k_BTf_+$ and $k_BTf_-$ for positively and negatively charged ions, respectively, where $k_BT$ it the thermal energy unit. We have that $f_+$ and $f_-$ are dimensionless. The external potentials imposed on ions in the system, are then given by

$$\beta V_\pm(r) = \begin{cases} 0 & \text{if } 0 < r < a; \\ f_\pm & \text{if } a < r < R, \end{cases}$$

if $\epsilon_1 > \epsilon_2$ and

$$= \begin{cases} f_\pm & \text{if } 0 < r < a; \\ 0 & \text{if } a < r < R, \end{cases} \tag{2.1}$$

if $\epsilon_1 < \epsilon_2$, where $\beta = 1/k_BT$, with $k_B$ is the Boltzmann constant and $T$ the temperature. In the cases we are interested in $f_+$ and $f_-$ will have the same sign. A crude estimate for this self-energy difference can be obtained using the Born self-energy formula. The self-energy of an ion in a dielectric medium, with relative permittivity $\epsilon$, is given by $E_{\text{self}} = e^2/(8\pi\epsilon_v\epsilon a_\pm)$. Here we consider the ion a homogeneously charged spherical shell, with charge $e$ and radius $a_\pm$, typically of the order of a couple of Angstrom. The Bjerrum length of vacuum is given by

$$\lambda_B = \frac{\beta e^2}{4\pi\epsilon_v}. \tag{2.2}$$

The Bjerrum length of vacuum is approximately 56 nm at room temperature, $T \approx 293.25$ K. Now the above may be written as $\beta E_{\text{self}} = \lambda_B/(2\epsilon a_\pm)$, in this approximation we have

$$f_\pm = \frac{\lambda_B}{2a_\pm}\left|\frac{1}{\epsilon_1} - \frac{1}{\epsilon_2}\right|.$$

The Born approximation is rather crude as it neglects solvent specific effects, such as molecular structure and dipole moment. This means that the actual self-energies may differ substantially form those we calculate in this approximation. However, for the purposes of this research, such deviations will not be relevant. We are mostly interested in qualitative behaviour and generating techniques, which could be used to obtain a semi-quantitative results. Henceforth, we will use the Born approximation, unless otherwise specified.

### 2.3.2 Self-Energy Potential Modifications

Note that in the above external potential, Eq. (2.1), the ions are point particles characterised by their centre-of-mass only. It will prove important to include finite size effects for ions to obtain better correspondence between theory and experiment, as is demonstrated in the work of M. Bier, Ref. [7], where it it is shown that a slight shift of the step-function self-energy potential w.r.t. the interface can drastically alter physical quantities such as the excess surface tension. Such a shift in the step-potential can be attributed to a variety of effects, among others finite ion size and/or the formation of a hydration shell around the ion. In this thesis we have chosen not to shift, but to weight our self-energy potential. This choice is based on geometric arguments. The weighting approach does produce a similar correspondence between theory and experiment as we will show later. See Ref. [11] for a more in-depth account of ion absorption at interfaces.

We still treat the ions as point particles with radius $a_\pm$ for Born self-energy purposes. However, at the interface the difference in self-energy will be weighted according to the effective ionic

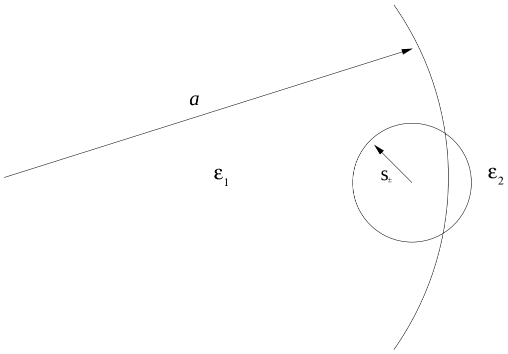

**Figure 2.4:** An ion with effective radius $s_\pm$ partially absorbed to the curved interface of a droplet with radius $a$. The volume fraction of the part of the ion which is in area 2, is used to modify the self-energy step function. Suppose that $\epsilon_1 > \epsilon_2$. If the effective ion is completely immersed in area 1, $0 < r < (a - s_\pm)$, the potential is given by $V_\pm(r) = 0$. If, on the other hand, it is in area 2, $(a + s_\pm) < r < R$, the potential is given by $V_\pm(r) = f_\pm$. For $(a - s_\pm) < r < (a + s_\pm)$ the potential is given by $f_\pm V_\pm / V$, where $V_\pm$ is the volume of the effective ion in area 2 and $V = 4\pi s_\pm^3/3$ is the total effective volume.

volume in both areas, see fig. 2.4 for this procedure. To assign an effective volume to an ion we will work with an effective ionic radius $s_\pm$. This effective radius need not be equal to the ionic radius $a_\pm$, because of for instance hydration shell effects. We will henceforth refer to $s_\pm$ as shell-parameters. Some basic calculus gives us the following for $\epsilon_1 > \epsilon_2$

$$\beta V_\pm(r) = \begin{cases} 0 & \text{if } 0 < r < (a - s_\pm); \\ f_\pm \frac{(r+s_\pm-a)^2(3a^2-2a(r-3s_\pm)-(r+s_\pm)(r-3s_\pm))}{16 r s_\pm^3} & \text{if } (a - s_\pm) < r < (a + s_\pm); \\ f_\pm & \text{if } (a + s_\pm) < r < R, \end{cases}$$

and for $\epsilon_1 < \epsilon_2$

$$= \begin{cases} f_\pm & \text{if } 0 < r < (a - s_\pm); \\ f_\pm \frac{(r-s_\pm-a)^2(2a(r+3s_\pm)+(r-s_\pm)(r+3s_\pm)-3a^2)}{16 r s_\pm^3} & \text{if } (a - s_\pm) < r < (a + s_\pm); \\ 0 & \text{if } (a + s_\pm) < r < R. \end{cases} \tag{2.3}$$

Note that the curved interface will induce an asymmetry between area 1 and area 2, i.e. the weighted self-energy potential would lie point symmetric around a flat interface. This asymmetry will not prove significant on the scales we will consider in this thesis, namely micron sized droplets and effective ion radii in the Angstrom range. See for instance fig. 2.5 for an example of a weighted self-energy potential, on the scale of the figure there is no discernable asymmetry due to curvature effects.

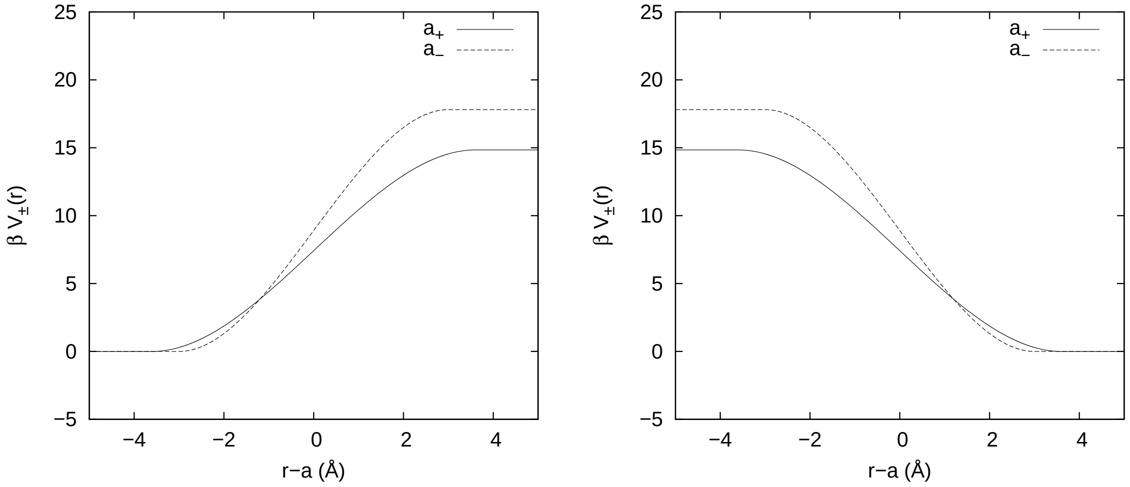

**Figure 2.5:** The weighted self-energy distributions for a WO (left) and an OW emulsion (right) close to the interface. The solid line corresponds to the self-energy potential for the positive ions, and the dashed line to that of the negative ions. Here we have the droplet radius $a = 1.0\ \mu$m, the dielectric constant of the oil $\epsilon_o = 5$, the positive ion radius $a_+ = 3.6$ Å, the negative ion radius $a_- = 3.0$ Å and the shell-parameters $s_\pm = a_\pm$.

## 2.4 The Grand Potential

Now that we have defined the external potential, we can consider the Grand Potential Functional and use DFT to find the equilibrium Grand Potential, by minimisation w.r.t. the variational ionic density profiles. For this system we obtain the variational functional of a single cell, given by

$$\begin{aligned}\beta\Omega[\rho_\pm] &= \beta\mathcal{F}[\rho_\pm] + \beta\sum_{i=\pm}\int \mathrm{d}\mathbf{r}\rho_i(r)(V_{\mathrm{ext,i}}(r) - \mu_i) \\ &= \sum_{i=\pm}\int \mathrm{d}\mathbf{r}\rho_i(r)\left(\log(\rho_i(r)\Lambda_i^3) - 1 + \frac{1}{2}q_i\phi(r,[\rho_\pm]) + \beta V_i(r) - \beta\mu_i\right) \\ &= \sum_{i=\pm}\int \mathrm{d}\mathbf{r}\rho_i(r)\left(\log\left(\frac{\rho_i(r)}{z_i}\right) - 1 + \frac{1}{2}q_i\phi(r,[\rho_\pm]) + \beta V_i(r)\right), \end{aligned} \tag{2.4}$$

where the integration boundaries are implicit. The integration is to be taken over the entire Wigner-cell, unless otherwise specified. We have introduced the fugacities $z_i = \exp(\beta\mu_i)/\Lambda_i^3$ in order to ease notation. The external potential term in Eq. (2.4) contains only the self-energy function. The Density Functional $\mathcal{F}[\rho_\pm]$ is comprised of an ideal gas and a Coulombic part which is given by the function $\phi(r,[\rho_\pm])$, i.e. the dimensionless electric potential caused by the presence of cations and anions. This electric potential is given by the Coulomb law

$$\phi(r,[\rho_\pm]) = \int \mathrm{d}\mathbf{r}'\sum_{i=\pm} q_i\rho_i(r')G(r,r')\ , \tag{2.5}$$

where $G(r,r')$ is a Greens function, such that it satisfies the Poisson Equation

$$\nabla_\mathbf{r}\cdot(\epsilon(r)\nabla_\mathbf{r}G(r,r')) = -4\pi\lambda_B\delta(r-r'). \tag{2.6}$$

Minimising the Grand Potential w.r.t. the density profiles yields

$$\begin{aligned}\left.\frac{\delta\beta\Omega[\rho_\pm]}{\delta\rho_i(r)}\right|_{\bar{\rho}_\pm} &= \log\left(\frac{\bar{\rho}_i(r)}{z_i}\right) + \beta V_i(r) + q_i\phi(r,[\bar{\rho}_\pm]) \\ &\equiv \log\left(\frac{\bar{\rho}_i(r)}{z_i}\right) + \beta V_i(r) + q_i\bar{\phi}(r) \\ &= 0. \end{aligned} \tag{2.7}$$

where factor 1/2 in front of the $\phi(r,[\bar{\rho}_\pm])$ term in Eq. (2.4) is cancelled by taking the density dependence of the electric potential into account, which also yields a $(1/2)\bar{\phi}(r)$ term when taking the functional derivative. To see this we apply a functional derivative of $\rho_k(r)$ on Eq. (2.5) to find

$$\begin{aligned} \sum_{i=\pm}\frac{1}{2}q_i\int \mathrm{d}\mathbf{r}'\rho_i(r')\frac{\delta}{\delta\rho_k(r)}\phi(r',[\rho_\pm])\bigg|_{\bar{\rho}_\pm} &= \\ \sum_{i=\pm}\frac{1}{2}q_i\int \mathrm{d}\mathbf{r}'\rho_i(r')\frac{\delta}{\delta\rho_k(r)}\int \mathrm{d}\mathbf{r}''\sum_{j=\pm}q_j\rho_j(r'')G(r',r'')\bigg|_{\bar{\rho}_\pm} &= \\ \sum_{i=\pm}\frac{1}{2}q_i\int \mathrm{d}\mathbf{r}'\rho_i(r')\int \mathrm{d}\mathbf{r}''\sum_{j=\pm}q_j\delta(r-r'')\delta_{kj}G(r',r'')\bigg|_{\bar{\rho}_\pm} &= \\ \sum_{i=\pm}\frac{1}{2}q_i\int \mathrm{d}\mathbf{r}'\rho_i(r')q_kG(r',r)\bigg|_{\bar{\rho}_\pm} &= \\ \frac{1}{2}q_k\phi(r,[\rho_\pm])\bigg|_{\bar{\rho}_\pm} &= \\ \frac{1}{2}q_k\bar{\phi}(r). & \end{aligned}$$

Using the fact that the equilibrium conditions minimise the Grand Potential, i.e. $(\delta\Omega/\delta\rho)|_{\bar{\rho}} = 0$, we obtain

$$\beta\Omega[\bar{\rho}_\pm] \;=\; -\sum_{i=\pm}\int \mathrm{d}\mathbf{r}\bar{\rho}_i(r)\left(1+\frac{1}{2}q_i\bar{\phi}(r)\right). \tag{2.8}$$

By applying relation (2.7) we find the following expression for the equilibrium densities

$$\bar{\rho}_i(r) \;=\; z_i\exp\left[-\beta V_i(r) - q_i\bar{\phi}(r)\right]. \tag{2.9}$$

We now define the 'ionic density' as

$$\begin{aligned}\bar{\rho}_s(r) &\equiv \sqrt{\bar{\rho}_+(r)\bar{\rho}_-(r)} \\ &= \sqrt{z_+z_-}\exp\left[-\beta\left(\frac{V_+(r)+V_-(r)}{2}\right)\right] \\ &= \begin{cases}\rho_{s,1} & \text{if } 0<r<(a-\max(s_\pm)); \\ \rho_{s,2} & \text{if } (a+\max(s_\pm))<r<R.\end{cases}\end{aligned} \tag{2.10}$$

Note that $\rho_{s,1}$ and $\rho_{s,2}$ are indeed spatial constants in their respective areas, and that $\rho_s(r)$ is a step-function if $s_\pm = 0$. Henceforth we will call the $\rho_{s,i}$ bulk densities, we will come back to this terminology later. Next, we introduce the modified and dimensionless electrostatic potential

$$\psi(r) \;\equiv\; \bar{\phi}(r) - \frac{1}{2}\log\left(\frac{z_+}{z_-}\right) + \phi_c(r), \tag{2.11}$$

where

$$\phi_c(r) \equiv \beta\frac{V_+(r) - V_-(r)}{2},$$

such that, by Eq. (2.9), (2.10) and (2.11)

$$\bar{\rho}_i(r) = \rho_s(r)\exp(-q_i\psi(r)). \tag{2.12}$$

The fugacities, $z_+$ and $z_-$, can without loss of generality be taken to be the same so that Eq. (2.11) reduces to

$$\psi(r) = \bar{\phi}(r) + \phi_c(r).$$

This modified electrostatic potential has notational and computational advantages in certain systems, whereas $\bar{\phi}(r)$ is more suitable for others. We will be using both $\bar{\phi}(r)$ and $\psi(r)$ in this thesis, because they are interchangeable via $\phi_c(r)$. Sometimes we will even apply both modified and regular potential at the same time, if this works better then using only one of the above. Thus we have found expression (2.12) for the equilibrium densities in terms of the electrostatic potential and the bulk densities. In the next section we derive the form of this potential.

## 2.5 Poisson Equation for Saline Emulsions

### 2.5.1 Derivation

In the following computation we apply Gauss' Law to the electric field $\bar{\phi}(r)$ corresponding to the electrostatic potential, via the electric displacement $\mathbf{D}(r) \equiv -\epsilon(r)\nabla_{\mathbf{r}}\bar{\phi}(r)$. Using Eq. (2.6) we obtain

$$\begin{aligned}
\nabla_{\mathbf{r}}\cdot\mathbf{D}(r) &= -\nabla_{\mathbf{r}}\cdot(\epsilon(r)\nabla_{\mathbf{r}}\bar{\phi}(r)) \\
&= -\nabla_{\mathbf{r}}\cdot\left(\epsilon(r)\nabla_{\mathbf{r}}\int \mathrm{d}\mathbf{r}'\sum_{i=\pm} q_i\bar{\rho}_i(r')G(r,r')\right) \\
&= -\int \mathrm{d}\mathbf{r}'\sum_{i=\pm} q_i\bar{\rho}_i(r')\nabla_{\mathbf{r}}\cdot\big(\epsilon(r)\nabla_{\mathbf{r}}G(r,r')\big) \\
&= 4\pi\lambda_B\int \mathrm{d}\mathbf{r}'\sum_{i=\pm} q_i\bar{\rho}_i(r')\delta(r-r') \\
&= 4\pi\lambda_B\sum_{i=\pm} q_i\bar{\rho}_i(r) \\
&= 4\pi\lambda_B\sum_{i=\pm} q_i\rho_s(r)\exp(-q_i\psi(r)) \\
&= -8\pi\lambda_B\rho_s(r)\sinh(\psi(r)).
\end{aligned} \tag{2.13}$$

By applying local commutativity of $\epsilon(r)$ and $\nabla_{\mathbf{r}}$ we may rewrite Eq. (2.13) as

$$\nabla^2_{\mathbf{r}}\bar{\phi}(r) = 8\pi\frac{\lambda_B}{\epsilon(r)}\rho_s(r)\sinh(\psi(r)). \tag{2.14}$$

This is the Poisson-Boltzmann Equation for the emulsive systems we are studying in the cell model employed in this thesis. Now introduce

$$\kappa^2(r) = \frac{8\pi\lambda_B\rho_s(r)}{\epsilon(r)} = \begin{cases} \kappa_1^2 & \text{if } 0 < r < (a - \max(s_\pm)); \\ \kappa_2^2 & \text{if } (a + \max(s_\pm)) < r < R, \end{cases}$$

where $\lambda_B$ is as in Eq. (2.2) and

$$\kappa_i^2 = \frac{8\pi\lambda_B\rho_{s,i}}{\epsilon_i}.$$

The quantity $\kappa^{-1}$ is called the 'Debye-length' or screening length of the solvent, where the index $i$ indicates the medium. Note that

$$\frac{\kappa_2^{-1}}{\kappa_1^{-1}} = \sqrt{\frac{\epsilon_2}{\epsilon_1}}\exp\left(\pm\frac{1}{4}(f_+ + f_-)\right),$$

which relates the screening lengths in both media via the relative electric permittivity and ionic self-energies. The plus-sign holds for $\epsilon_1 > \epsilon_2$ and the minus-sign for $\epsilon_1 < \epsilon_2$. Using $\nabla^2\psi = \nabla^2\bar{\phi}$ for the $s_\pm = 0$ system we may rewrite Eq. (2.14) in the following elegant and compact form

$$\nabla_{\mathbf{r}}^2\psi(r) = \kappa^2(r)\sinh(\psi(r)). \tag{2.15}$$

In the case that $s_\pm \neq 0$, it proves convenient to write it as

$$\nabla_{\mathbf{r}}^2\bar{\phi}(r) = \kappa^2(r)\sinh\left(\bar{\phi}(r) + \phi_c(r)\right). \tag{2.16}$$

### 2.5.2 Boundary Conditions

For this system we have the following boundary conditions for the Poisson-Boltzmann Equation, denoted here by BC.

- BC1: By radial symmetry of the problem we require that

  $$(\nabla_{\mathbf{r}}\bar{\phi})(0) = 0,$$

  i.e. there is no cusp at the origin. Or alternatively

  $$(\nabla_{\mathbf{r}}\psi)(0) = (\nabla_{\mathbf{r}}\phi_c(0)) = 0 \text{ if } a > \max(s_\pm).$$

- BC2: There is no free surface charge

  $$\begin{aligned} \lim_{r\uparrow a}\epsilon(r)\nabla_{\mathbf{r}}\bar{\phi}(r) &= \lim_{r\downarrow a}\epsilon(r)\nabla_{\mathbf{r}}\bar{\phi}(r), \\ \epsilon_1\lim_{r\uparrow a}\nabla_{\mathbf{r}}\psi(r) - \epsilon_1\lim_{r\uparrow a}\nabla_{\mathbf{r}}\phi_c(r) &= \epsilon_2\lim_{r\downarrow a}\nabla_{\mathbf{r}}\psi(r) - \epsilon_2\lim_{r\downarrow a}\nabla_{\mathbf{r}}\phi_c(r). \end{aligned}$$

- BC3: The electrostatic potential is continuous everywhere, therefore it is continuous at the interface, which implies

  $$\begin{aligned} \lim_{r\downarrow a}\bar{\phi}(r) &= \lim_{r\uparrow a}\bar{\phi}(r), \\ \lim_{r\downarrow a}\psi(r) - \lim_{r\downarrow a}\phi_c(r) &= \lim_{r\uparrow a}\psi(r) - \lim_{r\uparrow a}\phi_c(r). \end{aligned}$$

- BC4: The Wigner-Seitz cells are charge neutral, hence

$$\begin{aligned}(\nabla_{\mathbf{r}}\bar{\phi})(R) &= 0, \\ (\nabla_{\mathbf{r}}\psi)(R) &= (\nabla_{\mathbf{r}}\phi_c)(R) = 0 \text{ if } a + \max(s_\pm) < R.\end{aligned}$$

Using these boundary conditions we can in principle solve the Poisson Equation and find the equilibrium density profiles. The boundary conditions for the $\psi$ function seem to be more complicated in their general form. For the $s_\pm = 0$ system, however, they will reduce to an elegant set, as we will see in the next chapter. Solving this equation for these emulsive systems is not possible algebraically and we therefore require approximation techniques, algebraic and numeric, which will be discussed in the following chapters.

# Chapter 3

# Poisson Equation in Planar Limit Approximation

## 3.1 Introduction

From the previous chapter we know that the system is determined by solving the modified electrostatic equation from the Poisson Equation. We will only consider the shell-less ion system here, i.e. $s_\pm = 0$. Then we may rewrite Eq. (2.15) as

$$\begin{aligned} \nabla^2_{\mathbf{r}}\psi(r) &= \kappa^2(r)\sinh(\psi(r)) \quad \Rightarrow \\ \frac{1}{r^2}\frac{\partial}{\partial r}\left(r^2\frac{\partial}{\partial r}\right)\psi(r) &= \kappa^2(r)\sinh(\psi(r)). \end{aligned} \tag{3.1}$$

By the spherical symmetry of the problem $\psi(r)$ does not contain any angular terms, hence we may write only the radial part of the Laplacian. In this chapter we will consider a special case of this equation, where the droplet size w.r.t. the electrostatic screening lengths is such that the curvature effects of the interface can be neglected. When such effects can be neglected the system is said to be in the 'planar limit'. It will be shown that the condition for this to hold is $\kappa_1 a$, $\kappa_2 a$, $\kappa_1 R$ and $\kappa_2 R \gg 1$. The results we obtain for this system can be applied to the planar system with weighted self-energy potential in those areas where the external potential is constant, i.e. $r \notin [a - \max(s_\pm), a + \max(s_\pm)]$.

## 3.2 Analytic Results

In the planar limit we can rewrite the differential equation (3.1) as

$$\frac{\partial^2}{\partial z^2}\psi(z) = \kappa^2(z)\sinh(\psi(z)), \tag{3.2}$$

where $z = r - a$, so that the interface is located at the origin, $z = 0$, hence $\psi(z) = \psi(r - a)$ and $\kappa(z) = \kappa(r - a)$. The spherical Laplacian has been replaced with the Cartesian Laplacian, because in the planar limit one can neglect curvature effects, i.e we are working with a flat interface. The boundary conditions for this $s_\pm = 0$ system reduce to

- BC1:

$$\frac{\partial}{\partial z}\psi(-\infty) \quad = \quad 0;$$

- BC2:

$$\epsilon_1 \lim_{z\uparrow 0} \frac{\partial}{\partial z}\psi(z) \quad = \quad \epsilon_2 \lim_{z\downarrow 0} \frac{\partial}{\partial z}\psi(z);$$

- BC3:

$$\lim_{z\downarrow 0} \psi(z) - \lim_{z\uparrow 0} \psi(z) \quad = \quad \pm\frac{f_+ - f_-}{2} \ ;$$

  where the plus-sign corresponds to $\epsilon_1 > \epsilon_2$ and the minus-sign to $\epsilon_1 < \epsilon_2$,

- BC4:

$$\frac{\partial}{\partial z}\psi(\infty) \quad = \quad 0.$$

Note the drastic simplification w.r.t. the general boundary conditions in section 2.5.2. It is possible to solve this differential system algebraically, see for instance Ref. [12]. We obtain the following solution

$$\psi(z) \quad = \quad \begin{cases} 2\log\left(\frac{1+C_1 e^{\kappa_1 z}}{1-C_1 e^{\kappa_1 z}}\right) & \text{if } z < 0; \\ \\ -2\log\left(\frac{1+C_2 e^{-\kappa_2 z}}{1-C_2 e^{-\kappa_2 z}}\right) & \text{if } z > 0. \end{cases} \tag{3.3}$$

Note that the equation already satisfies BC1 and BC4. $C_1$ and $C_2$ can be determined using BC2 and BC3, such that

$$\begin{aligned} C_1 &= \frac{k + \cosh(\phi_c/2) - l}{\sinh(\phi_c/2)}, \\ C_2 &= \frac{1 + k\cosh(\phi_c/2) - l}{k\sinh(\phi_c/2)} \ , \end{aligned}$$

with

$$\begin{aligned} \phi_c &\equiv \pm\frac{f_+ - f_-}{2}, \\ k &= \frac{\kappa_1\epsilon_1}{\kappa_2\epsilon_2}, \\ l &= \sqrt{k^2 + 2k\cosh(\phi_c/2) + 1} \ . \end{aligned} \tag{3.4}$$

We have taken the negative branch of the root in Eq. (3.4), i.e. the minus sign in front of $l$, in order to ensure that $-1 < C_i < 1$. Alternatively, one can write

$$\begin{aligned} C_1 &= \tanh\left(\frac{\phi_0}{4}\right), \\ C_2 &= \tanh\left(\frac{\phi_c - \phi_0}{4}\right), \end{aligned}$$

with $\phi_0 = \phi(0)$.

## 3.3 Physical Quantities

### 3.3.1 Density Profiles, Grand Potential and Surface Tension

We introduce the following variable substitution, $x = C_1 e^{\kappa_1 z}$ and $y = C_2 e^{-\kappa_2 z}$ to rewrite Eq. (3.3) as

$$\psi(z) = \begin{cases} 2\log\left(\frac{1+x}{1-x}\right) & \text{if } z < 0; \\ \\ -2\log\left(\frac{1+y}{1-y}\right) & \text{if } z > 0. \end{cases} \tag{3.5}$$

Using Eq. (2.12) and Eq. (3.5) we determine the salt density profiles near the oil-water interface

$$\rho_{\pm}(z) = \begin{cases} \rho_{s,1}\left(\frac{1\mp x}{1\pm x}\right)^2 & \text{if } z < 0; \\ \\ \rho_{s,2}\left(\frac{1\pm y}{1\mp y}\right)^2 & \text{if } z > 0, \end{cases} \tag{3.6}$$

with

$$\rho_{s,1} = \rho_{s,2}\exp\left(\phi_c\right).$$

We find $\lim_{z\to-\infty}\rho_{\pm}(z) = \rho_{s,1}$ and $\lim_{z\to\infty}\rho_{\pm}(z) = \rho_{s,2}$. This is the reason why we call $\rho_{s,1}$ and $\rho_{s,2}$ bulk ion densities, as they are the densities in the 'bulk' of the system. The only place where the densities differ appreciably form their bulk values is near the interface, within a couple of screening lengths, $\kappa_1^{-1}$ and $\kappa_2^{-1}$ respectively. In the spherical geometry we have the same bulk densities, but because the droplet and Wigner-Seitz cell are finite the bulk value is usually not assumed at $r = 0$ or $r = R$. In the spherical geometry we impose that the water bulk value is assumed at $r = 0$ for WO and at $r = R$ for OW systems. Note that in the planar limit $\psi(-\infty) = \psi(\infty) = 0$, whereas for finite cells $\psi(0) = 0$ or $\psi(R) = 0$ rarely holds. However, if $\psi(0)$ approximates zero well and $\psi(R)$ is also very close to zero, then there is hardly any added contribution to physical quantities by extending the cell to infinity. That is to say, the cell and droplet are of sufficient size to permit the planar approximation. From the differential equation it is not hard to see that the behaviour of $\psi$ is dominated by exponential terms, which decay with characteristic length $\kappa_1^{-1}$ and $\kappa_2^{-1}$. Hence, we find that $\kappa_1 a$, $\kappa_2 a$, $\kappa_1 R$ and $\kappa_2 R \gg 1$ is a sufficient condition to assume the planar limit. In this regime the curvature effects of the interface become negligible.

In the planar limit the equilibrium Grand Potential is given from Eq. (2.8) by

$$\begin{aligned} \beta\Omega[\bar{\rho}_{\pm}] &= -4\pi a^2 \sum_{i=\pm}\int_{-\infty}^{\infty} \mathrm{d}z\ \rho_i(z)\left(1 + \frac{1}{2}q_i\bar{\phi}(z)\right) \\ &= -4\pi a^2 \int_{-\infty}^{0} \mathrm{d}z\ \rho_{s,1}\left[2\cosh(\psi(z)) - \sinh(\psi(z))\psi(z)\right] + \\ &\quad -4\pi a^2 \int_{0}^{\infty} \mathrm{d}z\ \rho_{s,2}\left[2\cosh(\psi(z)) - \sinh(\psi(z))\left(\psi(z) - \phi_c\right)\right] \\ &= -4\pi a^2 \int_{-\infty}^{0} \mathrm{d}z\ \rho_{s,1}\left[2\frac{1+6x^2+x^4}{(1-x^2)^2} - 8\frac{x+x^3}{(1-x^2)^2}\log\left(\frac{1+x}{1-x}\right)\right] + \end{aligned}$$

$$\begin{aligned}
&-4\pi a^2 \int_0^\infty \mathrm{d}z\ \rho_{s,2} \left[ 2\frac{1+6y^2+y^4}{(1-y^2)^2} - 8\frac{y+y^3}{(1-y^2)^2} \left( \log\left(\frac{1+y}{1-y}\right) + \frac{\phi_c}{2} \right) \right] \\
= & -4\pi a^2 \sum_{i=1,2} \int_0^{C_i} \mathrm{d}x\ \frac{\rho_{s,i}}{\kappa_i} \left[ 2\frac{1+6x^2+x^4}{x(1-x^2)^2} - 8\frac{1+x^2}{(1-x^2)^2} \log\left(\frac{1+x}{1-x}\right) \right] + \\
& 4\pi a^2 \phi_c \int_0^{C_2} \mathrm{d}y\ \frac{4\rho_{s,2}}{\kappa_2} \frac{1+y^2}{(1-y^2)^2} \\
= & \ 4\pi a^2 \sum_{i=1,2} \frac{8\rho_{s,i}}{\kappa_i} \frac{1}{1-C_i^2} \left( C_i \log\left(\frac{1+C_i}{1-C_i}\right) - 2C_i^2 \right) - \\
& 4\pi a^2 \phi_c \frac{4\rho_{s,2}}{\kappa_2} \frac{C_2}{1-C_2^2} - 4\pi a^2 \sum_{i=1,2} \frac{2\rho_{s,i}}{\kappa_i} \left[ \log(C_i) - \log(0) \right].
\end{aligned}$$

This is a divergent quantity. The divergence can be found in the $\log(0)$ term, which appears as a result of the pressure volume dependence of the Grand Potential, i.e. $\Omega = -PV + \gamma A$. Here $A$ is the surface area of the droplet and $\gamma$ is the surface tension caused by the presence of the ions. Since the volume, $x \in [-\infty, \infty]$, is infinite, it is pointless to talk about the equilibrium Grand Potential for this system. We can shift the equilibrium density profiles in such a way that this divergence does not occur, by subtracting the system's bulk densities in both areas. This eliminates the osmotic pressure term, which is responsible for the divergences. We only have the $\gamma A$ term left. By subtracting the bulk density from the density profiles via the Grand Potential we may write $\gamma \equiv (\Omega[\bar{\rho}_\pm] - \Omega[\rho_{\mathrm{bulk}}])/(4\pi a^2)$, and find

$$\begin{aligned}
\beta\gamma &= \sum_{i=\pm} \int_{-\infty}^{\infty} \mathrm{d}z \ \left( \rho_i(z) - \rho_s(z) + \frac{1}{2} q_i \rho_i(z) \bar{\phi}(r) \right) \\
&= \sum_{i=1,2} \frac{8\rho_{s,i}}{\kappa_i} \frac{1}{1-C_i^2} \left( C_i \log\left(\frac{1+C_i}{1-C_i}\right) - 2C_i^2 \right) - \\
& \quad \phi_c \frac{4\rho_{s,2}}{\kappa_2} \frac{C_2}{1-C_2^2} \ . \qquad (3.7)
\end{aligned}$$

The electric surface tension contributes to the total surface tension, hence it is sometimes called excess surface tension. There is always a surface tension at any interface, and the oil-water interface is no exception. The addition of ions to the emulsion will modify this existing surface tension by the amount calculated above, Eq. (3.7). It will turn out that this contribution is negligible compared to the zero-salt tension, as we will see when we discuss the results. The surface tension quantifies the system's tendency to coarsen by e.g. coalescence of droplets. Negative surface tension results in mixing whereas positive surface tension results in demixing. For a negative surface tension, the system will tend to maximise the surface area of the interface, which results in many small droplets with a large total surface area. Positive surface tension will drive the system to form one (a few) large droplet(s) with a relatively small contact area between oil and water.

### 3.3.2 Surface Charge and Inter-Droplet Interactions

Finally we examine the surface charge of the droplets and the electric part of the DLVO (Derjaguin, Landau, Verwey and Overbeek) potential. Because the density profiles of positive and negative ions are usually not the same, the droplets and medium will both incur an equal and opposite net charge, $Z_i$. This is caused by a phenomena referred to as preferential partitioning. Preferential partitioning can be explained as follows. Both species of ions prefer the water and 'dislike' the oil, which is quantified by the self-energy difference. Entropy favours a system with ions in both the water and the oil. However, adding an ion of the species with the highest self-energy difference to the oil will increase the system's energy more than by adding an ion of the other species. The system will tend to minimise its energy. When the system equilibrates the interplay of energy and entropy causes a difference in ionic density, which induces a charge in both areas. Although, the local charge neutrality is violated, global charge neutrality is conserved.

We call the charge a surface charge, because for small screening lengths it is located close to the interface, especially in the water area, i.e. a double-layer is formed. For a spherical droplet the charge can be determined by integration over the ion density difference. The corresponding surface charge is then calculated by dividing by $4\pi a^2$. However, in the planar limit the interface is flat, corresponding to an infinite droplet with an infinite charge. Hence, we need to talk about surface charges, which are always finite, rather than charges, if we want to compare the planar and spherical geometry. This is the second reason why we speak of surface charges instead of charges in the planar limit. One can approximate the charge of a droplet with a finite $a$ as $Z \approx 4\pi a^2 \sigma_{\mathrm{pl}}$, where $\sigma_{\mathrm{pl}}$ is the planar surface charge. The charge we find in this way will, however, differ form the charge one obtains by performing the full calculation in the spherical geometry. The surface charges are given by $\sigma_i = Z_i/(4\pi a^2)$, yielding

$$\begin{aligned}
\sigma_1 &= \frac{1}{4\pi a^2}\sum_{i=\pm}\int_0^a \mathrm{d}\mathbf{r} q_i \bar{\rho}_i(r) \\
&= -\frac{1}{2\pi a^2}\rho_{s,1}\int_0^a \mathrm{d}\mathbf{r}\sinh(\psi(r)) && (3.8) \\
\sigma_2 &= -\frac{1}{2\pi a^2}\rho_{s,2}\int_a^R \mathrm{d}\mathbf{r}\sinh(\psi(r)). && (3.9)
\end{aligned}$$

In the planar limit Eq. (3.8) and (3.9) reduce to

$$\begin{aligned}
\sigma_1 &= -2\rho_{s,1}\int_{-\infty}^0 \mathrm{d}z\sinh(\psi(z)) \\
&= -\frac{8\rho_{s,1}}{\kappa_1}\frac{C_1}{1-C_1^2} && (3.10) \\
\sigma_2 &= -\frac{8\rho_{s,2}}{\kappa_2}\frac{C_2}{1-C_2^2}, && (3.11)
\end{aligned}$$

where BC2 implies that $\sigma_1 = -\sigma_2$.

The droplet has a charge and hence an electric field, which is screened by the presence of ions in the medium. The electric interaction potential between two droplets is given by the electric part of the DLVO potential. Note that the electric potential only contributes for $r > 2a$, because the inter droplet distance is at least $2a$, measured from the centre of mass of each droplet. If we assume that all droplets are of the same size, we find

$$\beta U_{121}(r) = \frac{\lambda_B Z_1^2}{\epsilon_2}\left(\frac{\exp(\kappa_2 a)}{1+\kappa_2 a}\right)^2 \frac{\exp(-\kappa_2 r)}{r}.$$

Here the subscript in $U_{121}$ indicates that we have an interaction between two droplets with relative dielectric constant $\epsilon_1$ over a medium with $\epsilon_2$. Henceforth, this will be abbreviated as

$U(r) \equiv U_{121}(r)$. Normally the DLVO potential would also contain a Van-der-Waals component, however, it will prove irrelevant the droplet separations of interest in this investigation. We have set up the theoretical tools for the planar limit, in the special case that $s_{\pm} = 0$. However, outside the range $[-\max(s_{\pm}), \max(s_{\pm})]$ most of the above results hold for or can be modified to be used for a planar system with $s_{\pm} \neq 0$. For the range $[-\max(s_{\pm}), \max(s_{\pm})]$ we must solve the differential equation, Eq. (3.1), by means of numerical techniques. Since we will discuss numerical techniques for spherical systems in the next chapter, we will not go into this here.

# Chapter 4

# Poisson Equation in the Spherical Geometry

## 4.1 Introduction

Now that we have solved the system in the planar limit, let us examine the properties of the system in the spherical geometry. The differential equation, Eq. (2.16), for the electrostatic potential

$$\begin{aligned} \nabla^2_{\mathbf{r}}\bar{\phi}(r) &= \kappa^2(r)\sinh\left(\bar{\phi}(r)+\phi_c(r)\right) \Rightarrow \\ \frac{1}{r^2}\frac{\partial}{\partial r}\left(r^2\frac{\partial}{\partial r}\right)\bar{\phi}(r) &= \kappa^2(r)\sinh\left(\bar{\phi}(r)+\phi_c(r)\right), \end{aligned} \tag{4.1}$$

cannot be solved algebraically. It can, however, be solved using a numerical approach on an $r$-grid by standard iterative methods on desktop PC's. Typically, we use several thousand non-equidistant grid points, with a relatively small grid spacing close to the interface. In this chapter we will treat the numerical techniques used to solve this differential equation and discuss the expressions for the system quantities in the spherical geometry.

## 4.2 Numerical Integration Schemes

### 4.2.1 Differential Equations

Let us assume that we have a non-equidistant $r$-grid, with grid points labelled $r_i$, where $i \in \{0, \ldots, N\}$ for some $N$. We may then rewrite the Laplacian in Eq. (4.1) as

$$\nabla^2_{\mathbf{r}}\bar{\phi}(r_i) = \left(\frac{\partial^2}{\partial r_i^2}+\frac{2}{r_i}\frac{\partial}{\partial r_i}\right)\bar{\phi}(r_i)$$

Now we use the following non-equidistant approximation schemes for the first and second derivative

$$\bar{\phi}'(r_i) = \frac{\bar{\phi}(r_{i+1})-\bar{\phi}(r_{i-1})}{r_{i+1}-r_{i-1}}$$

$$
\begin{aligned}
\bar{\phi}''(r_i) &= \frac{2\bar{\phi}(r_{i+1})}{(r_{i+1}-r_i)(r_{i+1}-r_{i-1})} - \frac{2\bar{\phi}(r_i)}{(r_{i+1}-r_i)(r_i-r_{i-1})} + \\
&\quad \frac{2\bar{\phi}(r_{i-1})}{(r_{i+1}-r_{i-1})(r_i-r_{i-1})},
\end{aligned}
$$

which in the equidistant case reduce to the well-known formulas for these derivatives. Using these equations we may write

$$
\begin{aligned}
\bar{\phi}(r_{i+1}) &= \frac{r_i}{r_{i+1}}\frac{r_{i+1}-r_{i-1}}{r_i-r_{i-1}}\bar{\phi}(r_i) + \\
&\quad \frac{\kappa(r_i)^2}{2}\frac{r_i}{r_{i+1}}(r_{i+1}-r_i)(r_{i+1}-r_{i-1})\sinh\left(\bar{\phi}(r_i)+\phi_c(r_i)\right) - \\
&\quad \frac{r_{i-1}}{r_{i+1}}\frac{r_{i+1}-r_i}{r_i-r_{i-1}}\bar{\phi}(r_{i-1}),
\end{aligned}
$$

or alternatively

$$
\begin{aligned}
\bar{\phi}(r_{i-1}) &= \frac{r_i}{r_{i-1}}\frac{r_{i+1}-r_{i-1}}{r_{i+1}-r_i}\bar{\phi}(r_i) + \\
&\quad \frac{\kappa(r_i)^2}{2}\frac{r_i}{r_{i-1}}(r_{i+1}-r_{i-1})(r_i-r_{i-1})\sinh\left(\bar{\phi}(r_i)+\phi_c(r_i)\right) - \\
&\quad \frac{r_{i+1}}{r_{i-1}}\frac{r_i-r_{i-1}}{r_{i+1}-r_i}\bar{\phi}(r_{i+1}).
\end{aligned}
$$

With these recursive relations we must use the discretised version of the boundary conditions as described in section 2.5.2 to fix the solution.

### 4.2.2 Modified Boundary Conditions

We implement a shooting type method to extract the full solution. The form of the recursion requires two initial values, in the first case $\bar{\phi}(r_{i-1})$ and $\bar{\phi}(r_i)$, to start the recursive process. Using the boundary conditions one can easily see that the entire problem is determined by $\bar{\phi}(0)$, or $\bar{\phi}(R)$ respectively.

- BC1: The derivative at the origin is zero, i.e. for $r_0 = 0$ and sufficiently small $r_1 - r_0$ we have $\bar{\phi}(r_1) = \bar{\phi}(r_0)$. This gives us sufficient information to start our recursion in area 1.
- BC2: For some $j \neq 0, N$ we have $r_j = a$ and $r_{j+1} = a$, so that

  $$\bar{\phi}'(r_{j+1}) = \frac{\epsilon_1}{\epsilon_2}\frac{\bar{\phi}(r_j)-\bar{\phi}(r_{j-1})}{r_j - r_{j-1}}.$$

  The choice to repeat the interfacial radius $r = a$ for two consecutive grid points enables us to cope with the discontinuity in $\bar{\phi}'(r)$ in a relatively elegant manner.
- BC3: We have

  $$\bar{\phi}(r_{j+1}) = \bar{\phi}(r_j),$$

  which together with BC2 yields

  $$\bar{\phi}(r_{j+2}) = \bar{\phi}(r_{j+1}) + (r_{j+2}-r_{j+1})\bar{\phi}'(r_{j+1}).$$

  These two points, $\bar{\phi}(r_{j+1})$ and $\bar{\phi}(r_{j+2})$, are enough to start the recursion in area 2.

- BC4: Finally we use

  $$\bar{\phi}'(r_N = R) \quad = \quad 0,$$

  to find an appropriate initial guess for $\bar{\phi}(0)$, because there is only one $\bar{\phi}(0)$ for which $\bar{\phi}'(r_N) = 0$. A half-value routine is implemented to determine this root.

Alternatively one can set the boundary conditions the other way around for backward recursion. It has proven useful to implement both techniques, forward and backward recursion, in order to perform numerical integration starting in the area with the lowest dielectric constant. Doing so gives greater numerical stability in the solution routines. In principle this integration technique should give exact results for a vanishing grid-size, in practice the shooting technique is fraught with numerical difficulties, which we have attempted to eliminate to the best of our ability.

### 4.2.3 Linearised Poisson Equation

It turns out that we can perform two approximations to overcome many of these difficulties. For small values of $x$ we have $\sinh(x) \approx x$. Hence, we may expand the differential equation for $|\psi(r)| \ll 1$ as follows

$$\begin{aligned} \left(\frac{\partial^2}{\partial r_i^2} + \frac{2}{r_i}\frac{\partial}{\partial r_i}\right)\psi(r_i) &= \kappa_j^2 \sinh(\psi(r_i)) \\ &\approx \kappa_j^2 \psi(r_i). \end{aligned} \tag{4.2}$$

Recall that $\psi$ drops off to zero. Using $\psi$ we can then determine the limiting behaviour of $\bar{\phi}$ via $\psi = \bar{\phi} + \phi_c$. Note that we are sufficiently far away from the interface to work with the bulk $\kappa$. When we assume that $\psi(0) = 0$ and that $\psi$ is sufficiently small in the range $[0, a^*]$ the solution of Eq. (4.2) is given by

$$\psi(r) \quad = \quad \psi(a^*)\frac{a^*}{r}\frac{\sinh(\kappa_1 r)}{\sinh(\kappa_1 a^*)} \quad \text{if } 0 < r < a^* \ .$$

Empirically it is justified to use $a^* = a - \max(s_\pm)$ for WO emulsions discussed in this thesis. Since $\psi(0)$ tends to zero close to the planar limit, the above expression is instrumental in overcoming some of the numerical problems in the shooting method for nearly planar systems. In order to describe infinite Wigner-Seitz cells with a finite droplet in them, it can be useful to truncate the numerical integration in area 2 at some $R^*$, for which $|\psi(r)| \ll 1$ if $r > R^*$. We know that $\psi(\infty) = 0$, hence we write

$$\psi(r) \quad = \quad \psi(R^*)\frac{R^*}{r}e^{-\kappa_2(r-R^*)} \quad \text{if } r > R^* \ .$$

In the case of OW emulsions we may use this formula for $R^* = a + \max(s_\pm)$. Applying the aforementioned numerical integration techniques we find the electrostatic potential, $\bar{\phi}$, or equivalently $\psi$. We can then use this to determine the system properties, which we will discuss in the next section.

## 4.3 Physical Quantities

The salt density profiles in the spherical geometry are given by Eq. (2.12), i.e

$$\bar{\rho}_{\pm}(r) \quad = \quad \rho_s(r)\exp(\mp\psi(r)). \tag{4.3}$$

The corresponding equilibrium Grand Potential of one cell is

$$\begin{aligned}\beta\Omega[\bar{\rho}_{\pm}] &= -4\pi\sum_{i=\pm}\int_0^R \mathrm{d}r\ r^2\rho_i(r)\left(1+\frac{1}{2}q_i\bar{\phi}(r)\right)\\ &= -4\pi\int_0^R \mathrm{d}r\ r^2\rho_s(r)\left[2\cosh(\psi(r))-\sinh(\psi(r))\left(\psi(r)-\phi_c(r)\right)\right],\end{aligned}$$

which is finite in the spherical geometry for finite Wigner-cells. The surface tension is given by

$$\beta\gamma \quad = \quad -\frac{1}{a^2}\sum_{i=\pm}\int_0^R \mathrm{d}r\ r^2\left(\rho_i(r)-\rho_{\mathrm{bulk}}(r)+\frac{1}{2}q_i\rho_i(r)\bar{\phi}(r)\right), \tag{4.4}$$

with $\rho_{\mathrm{bulk}}(r)=\rho_{s,1}$ if $0<r<a$ and $\rho_{\mathrm{bulk}}(r)=\rho_{s,2}$ if $a<r<R$. For non-planar droplets $\bar{\rho}_{\pm}(R)$ need not be equal to $\rho_{s,2}$ if we require that $\bar{\rho}_{\pm}(0)=\rho_{s,1}$ and vice versa. Hence, subtracting the bulk densities to remove the divergent osmotic pressure terms in the equilibrium Grand Potential is not quite as natural as it is in the planar limit approximation. Using Eq. (3.8) and (3.9) we find that the surface charge densities are given by

$$\sigma_1 \quad = \quad -\frac{2}{a^2}\int_0^a \mathrm{d}r\ r^2\rho_s(r)\sinh(\psi(r)) \tag{4.5}$$

$$\sigma_2 \quad = \quad -\frac{2}{a^2}\int_a^R \mathrm{d}r\ r^2\rho_s(r)\sinh(\psi(r)). \tag{4.6}$$

The electric DLVO potential of the two droplets at separation $r>2a$ is given by

$$\beta U(r) \quad = \quad \frac{\lambda_B Z_1^2}{\epsilon_2}\left(\frac{\exp(\kappa_2 a)}{1+\kappa_2 a}\right)^2\frac{\exp(-\kappa_2 r)}{r}, \tag{4.7}$$

which is a Yukawa potential. Here $Z_i=4\pi a^2\sigma_i$. It proves useful to relate this potential to the system's ability to crystallise, see Refs. [5, 9, 10]. To that end we introduce the coupling parameter

$$\Gamma \quad \equiv \quad \beta U(R)\left(1+\kappa_2 R+\frac{1}{2}(\kappa_2 R)^2\right). \tag{4.8}$$

$\Gamma$ is commonly referred to as the 'plasma-parameter'. In Ref. [10] it has been shown that a Yukawa system with $\Gamma>106$ crystallises. Now that we have expressions for the relevant physical quantities in the spherical geometry, Eq. (4.3)-(4.8), and the planar limit, Eq. (3.6)-(3.11), we can compare the results in the following chapters.

## Prelude to the Analysis

The discussion of the results obtained using our analytical and numerical approaches to solving the Poisson Equation in the spherical geometry can be be divided into two parts. In the first part, planar results are compared to the case of a droplet in an infinite Wigner-cell, which is a model for emulsions with very low oil/water ratio. In the second part we examine droplets in a finite Wigner-Seitz cell, i.e. a finite volume fraction. This part is subdivided into a section which treats the surface charge and plasma-parameter and a section which treats the surface tension. We have considered the planar system to gain insight into the parameter dependence of physical quantities in the spherical geometry. Also, we have attempted to examine parts of parameter space in the spherical geometry, which show interesting behaviour in the planar limit, as far as this was numerically possible.

# Chapter 5

# The Dilute Droplet Limit

## 5.1 Introduction

In this part we will examine emulsions which have a very low oil-water or water-oil ratio. These emulsions can be modelled with an infinitely dilute system, i.e. a one droplet emulsion, when the inter-droplet separation is such that each droplet and its surroundings can be considered an independent system. In this dilute limit we will focus on the surface charge and surface tension properties of emulsions. Since crystallisation cannot occur in the dilute limit, we will not consider the plasma-parameter in this chapter. It proves necessary to switch between the surface charge, $\sigma$, and charge, $Z$, on the one hand and surface tension, $\gamma$, and surface energy, $E_s \equiv 4\pi a^2\gamma$, on the other during the course of discussion. The elements in these sets of physical quantities are interchangeable, which will be useful in formulating mathematical relations.

It is important to note that our parameter space is at least 8-dimensional. That is to say, we have the droplet radius $a$, the Wigner-cell radius $R$, the bulk ion concentration in water $\rho_w$, the relative dielectric constant of the oil $\epsilon_o$, the positive ion radius $a_+$, the negative ion radius $a_-$, the positive shell-parameter $s_+$, the negative shell-parameter $s_-$ and the temperature $T$, which are independent. We have therefore made some judicious choices to analyse only part of the parameter space. These choices are for the most part inspired by known experimental parameters, see Ref. [3] or physical quantities which are considered reasonable.

Unless stated otherwise we will keep the following fixed: $T = 293.25$ K, $a_+ = 3.6$ Å, $a_- = 3.0$ Å and $s_+ = s_- = 0.0$ Å for the step self-energy potential, or $s_\pm = a_\pm$ for the weighted self-energy potential. The values for the ion size are based on the ionic radius of sodium and bromide in water respectively. Recall that the ions in the emulsions used in were $\mathrm{H}^+$ and $\mathrm{Br}^-$, with radii $a_+ = 2.8$ Å and $a_- = 3.0$ respectively. We have chosen not to use these radii, since the ions are so similar in size that the algorithms we use will encounter numerical difficulties, as we will see in the course of our investigation. Moreover, the ion size is merely a tool which via the Born approximation ensures that the self-energies scale correctly with changing $\epsilon_o$. In certain cases we will vary $s_\pm$ and $a_\pm$ in the $0 - 1$ nm range. We consider $2 < \epsilon_o < 10$ a reasonable range for the relative dielectric constant of oil used in experiments. However, we will sometimes extend this to the larger domain, $\epsilon_o = 1 - 80$, for completeness. The ion concentration in water is restricted between $10^{-7}$ M and 10 M. The lower limit is that of pure water with a pH of 7 imposed by the self-dissociation of the water molecules into $H^+$ and $OH^-$, whereas the upper limit is due to the finite solubility of salt in water. We will often work with $\rho_w = 1$ mM, which is roughly in the middle of the specified ion density range.

The aim of this chapter is threefold. One, to familiarise the reader with the effects of curvature on physical quantities w.r.t. the the same quantities determined in a planar limit approximation. Two, to discuss the physics behind the observed differences. Three, to model these differences. We will begin by examining the $a \rightarrow \infty$ limit, in order to establish the correctness of our numerical techniques and to gain insight into the effects of curvature. From our investigation of the properties of $\sigma$, $Z$, $\gamma$ and $E_s$, we are able to formulate a model which relates the spherical value for the surface charge and tension to the planar value by means of a polynomial expansion in terms of $1/(\kappa_o a)$.

It will become apparent that both the planar and the spherical geometry have pros and cons. A calculation in the planar limit has the benefit of being analytic and hence parameter dependencies can be more readily determined. This does come at a price, namely that the values of the physical quantities one determines in this limit can differ dramatically from those of the actual/spherical system. Solving the Poisson Equation in the spherical geometry will naturally yield more accurate results, however, determining the parameter dependence requires lengthy, tedious numerical calculations, which lose their insightfulness.

Careful examination of the data will show that there is a middle ground between the relative ease and speed with which quantities can be determined in the planar limit and the precision of the calculations in the spherical geometry. This middle ground is found by using the polynomial expansion in $1/(\kappa_o a)$ alluded to earlier. In our investigation of dependence of the physical quantities on the system parameters, we will also spend considerable attention to this expansion technique and we will show that the expansion coefficients are extremely well-behaved.

## 5.2 Surface Charge and Tension

In fig. 5.1 one can see the dependence of the surface charge on the inverse droplet radius for several values of $\epsilon_o$. The surface charge of the system with self-energy step and that of the system with weighted self-energy function do not differ substantially, this proves to hold in general. The limiting value for $a \rightarrow \infty$ is indeed the planar value. For planar surface charges the only difference between oil-water (OW) and water-oil (WO) is the sign, which follows from preferential partitioning, whereas for the spherical geometry there are two definite asymmetries between the OW and WO emulsions.

Fig. 5.2 shows the surface tension as a function of the inverse droplet radius for the step and weighted self-energy potential for the same series of $\epsilon_o$. The surface tension of the system with self-energy step and that of the system with weighted self-energy function differ significantly. This also proves to hold in general, where naturally the difference becomes smaller as $s_\pm$ approaches zero. However, the deviation from the planar value of $\gamma$ is similar for both systems, indicating a common curvature effect. The difference in value, i.e. negative $\gamma$s in the nN/m range for $s_\pm = 0$ and positive $\gamma$s in the $\mu$N/m range for $s_\pm = a_\pm$, can be explained by the fact that weighted potential gives a fixed contribution to the surface tension, which is almost independent of the electrostatics of the system. In other words, there is a curvature independent component to $\gamma$ related to the self-energy potential which induces the difference in value, whereas curvature only significantly influences the electrostatic part excess surface

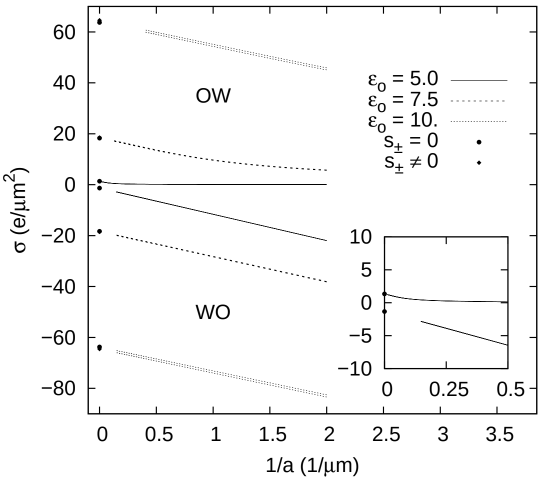

**Figure 5.1:** The surface charge, $\sigma$, in elementary charges per square micrometre as a function of the inverse droplet radius, $1/a$, for a series of $\epsilon_o$ at $\rho_w = 1.0$ mM. The dots indicate the planar value for the system with $s_+ = s_- = 0.0$ Å and the diamonds indicate the planar value for the system with $s_+ = 3.6$ Å and $s_- = 3.0$ Å. Oil droplets in water are positively charged and water droplets in oil are negatively charged, because of the preferential partitioning of the positive and negative ions.

tension, which acts as a perturbation on the weighted contribution. This can be easily seen by examining the planar limit.

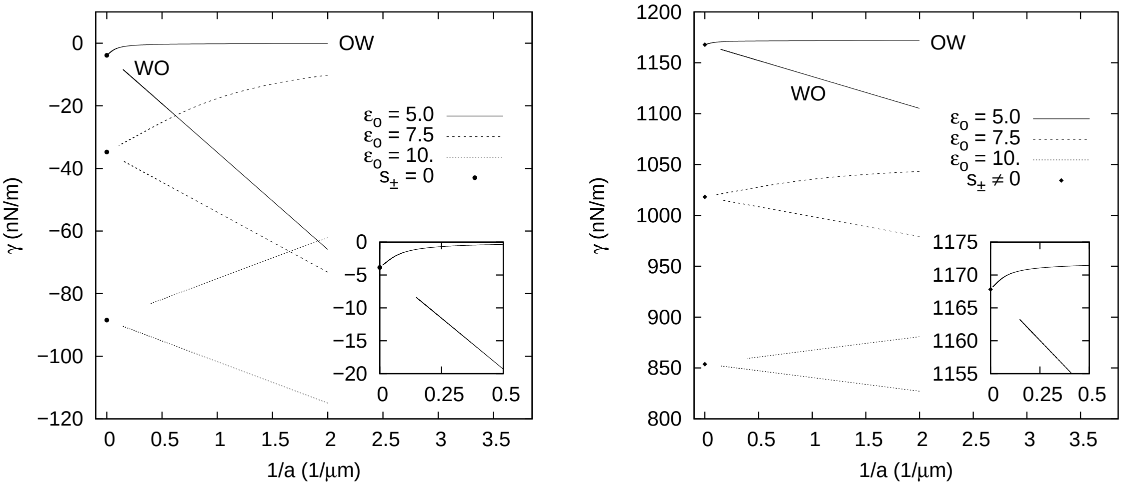

**Figure 5.2:** The surface tension, $\gamma$, in nano-Newtons per meter as a function of the inverse droplet radius, $1/a$. The systems correspond to those in fig. 5.1. We have $s_\pm = 0$ (left) and $s_\pm = a_\pm$ (right).

From figures 5.1 and 5.2, we can also see that the effect of the spherical geometry for finite droplets is to increase $|\sigma|$ and $|\gamma|$ w.r.t. the planar value for WO emulsions and to decrease these quantities for OW emulsions. We should re-emphasise that we recognise two types of asymmetry here, the one described above, which we will call the increase-decrease asymmetry and the one, which we will call the behaviour asymmetry. The behaviour asymmetry refers to the linear deviation form the planar value in terms of $1/a$ for WO systems and the highly non-linear deviation from the planar value for OW systems. We will come back to this in the next chapter. The increase-decrease asymmetry can be explained solely by the curvature of the interface. In the planar geometry we have exponential decay of the potential and the density profiles near the interface, i.e. $\exp(-\kappa z)$, whereas in the spherical geometry this is modified to $\exp(-\kappa r)/r$. This means that the part of the double-layer inside the droplet is 'compressed' and the part outside the droplet is 'stretched out'. For $\sigma$ as well as $\gamma$ we may conclude that the oil area has a dominant contribution to the value of these quantities. OW systems have a compressed oil part of the double-layer and corresponding decrease in $|\sigma|$ and $|\gamma|$ and WO systems we have a stretched oil part of the double-layer and a corresponding increase. For larger droplets this stretching and compressing effect becomes smaller, because locally the interface appears flatter.

Note that both self-energy functions, i.e. step and weighted, have relatively small values for $\gamma$, in the 1 nN/m to 10 $\mu$N/m range, whereas the regular surface tension of an oil-water interface is of the order of $1-10$ mN/m. Therefore, the contribution of the electrostatic part of the surface tension is insignificant compared to the regular surface tension. Although there is a marked increase in $\gamma$ for the shell system w.r.t. the $s_{\pm}=0$ system, the values are still insufficient to influence the regular oil water surface tension. In fact, the contribution of the excess surface tension has a positive sign for the weighted self-energy potential instead of a negative sign, eliminating any possibility of inducing a thermodynamically stable situation. Since the regular surface tension is also positive one hopes that by adding a negative ionic contribution one is able to find a global Grand Potential minimum other than that of a demixed system. However, with a positive electrostatic surface tension an emulsion is more likely to demix. At the end of this chapter it should be clear to the reader that for any reasonable system configuration, with either a step or a weighted self-energy potential, there is no discernable effect in raising or lowering the regular surface tension within the confines of our model.

## 5.3 Curvature Expansion for the Spherical Geometry

### 5.3.1 Preliminary Model

Examination of the data we have accumulated during our research leads us to conclude that we may describe the surface charge and tension in the spherical geometry for an infinite Wigner-cell according to a polynomial expansion in $1/(\kappa a)$ around the planar value. Equivalently we may expand the charge and surface energy around zero using a polynomial in $\kappa a$ of degree two. We have chosen to perform an expansion in terms of $1/(\kappa a)$ and $\kappa a$ respectively, since this is a dimensionless quantity. Let us illustrate this polynomial expansion using figures 5.1 and 5.2. From these figures we can see that there is an initially linear, followed by a quadratic, deviation form the planar value in terms of $1/a$. This statement applies to both WO and OW emulsions, however, for the latter it only holds for much larger droplet radii than is the case for WO emulsion. Alternatively, we can examine the charge and the surface energy dependence on the droplet radius. See figures figures 5.3 and 5.4 for $Z$ and $E_s$ corresponding to figures 5.1 and 5.2, but now as a function of $a$ with $a \in [0, 0.5]$ $\mu$m, keeping the other parameters fixed. Note that the charge and surface energy scale as polynomials of degree 2 with $a$.

Based in part on these four figures and in part on the results described in the upcoming sections,

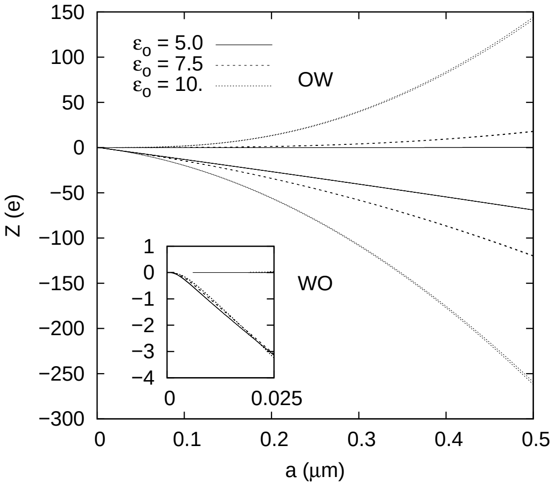

**Figure 5.3:** The charge, $Z$, in elementary charges as a function of the droplet radius, $a$. The systems are otherwise identical to the ones in fig. 5.1. The insert has been included to indicate that the charge indeed vanishes for $a \to 0$. The charge $Z$ behaves as a polynomial of degree two in $a$. Some lines terminate before reaching $a = 0$, see the inset, due to numerical instability.

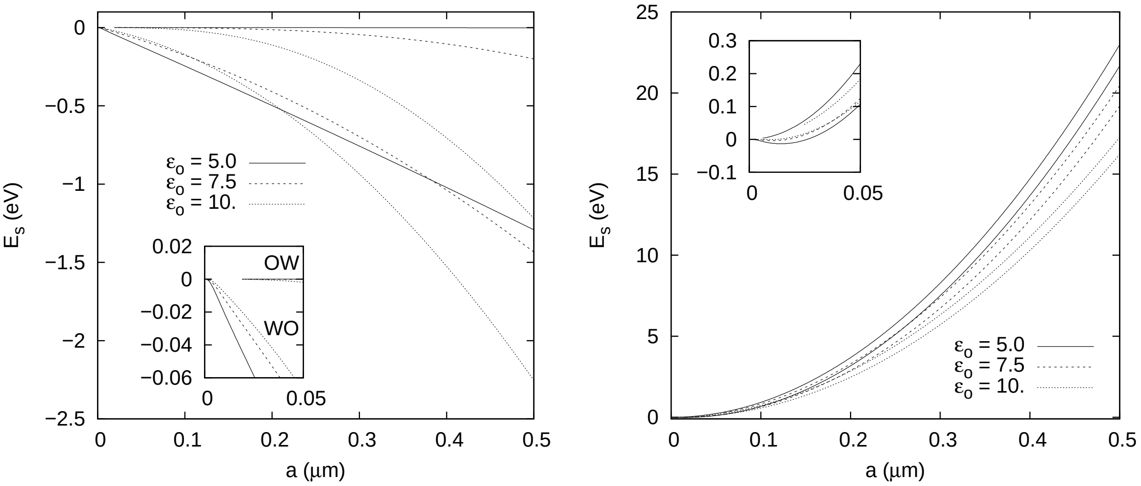

**Figure 5.4:** The surface energy, $E_s$, in eV as a function of the droplet radius, $a$. The systems are otherwise the same as in fig. 5.2, $s_\pm = 0$ (left) and $s_\pm = a_\pm$ (right). In the figure on the right we have that the OW system's lines are the top ones and the WO system's lines are the bottom ones. The need to use (eV) on the $E_s$ scale is another strong indication that the surface tension terms are indeed quite small. The surface energy also scales as a polynomial of degree 2 with $a$.

we may set up the following expansion approach. Let $V$ be either $Z$ or $E_s$ and let $v$ be the corresponding $\sigma$ or $\gamma$. Let the subscript $s_\pm$ indicate the fact that $V$ and $v$ are both dependent on the shell-parameters. The subscript $s_\pm = 0$ in $V_{(s_\pm=0)}$ and $v_{(s_\pm=0)}$, then indicates that $V$ or $v$ is the physical quantity as found for the step self-energy potential with all other system parameters the same as for $V_{s_\pm}$ and $v_{s_\pm}$ respectively. Let $\tilde{c}_{i,j}$ be the $i$-th expansion coefficient corresponding to the quantity $j \in \{v, V\}$. Furthermore, let $v(a)$ be the value determined by solving the Poisson Equation in the spherical geometry with droplet radius $a$ and $v(\infty)$ the value found by means of the planar approximation. Using the above definitions we may write

$$V_{s_\pm}(a) \quad = \quad \tilde{c}_{0,V} + \tilde{c}_{1,V}(\kappa_o a + \kappa_w a) + \tilde{c}_{2,V}((\kappa_o a)^2 + (\kappa_w a)^2) + \text{h.o.t.},$$

where 'h.o.t.' stands for those terms which are non-polynomial in $a$. These higher order terms become significant for 'small' sized droplets, where the definition of small depends on the system we consider, but they may otherwise be neglected. Note that, because the planar values for $\sigma = \lim_{a\to\infty} Z(a)/(4\pi a^2)$ and $\gamma = \lim_{a\to\infty} E_s(a)/(4\pi a^2)$ are finite, the highest order term must at most scale with $a^2$. This means that all contributions contained in the h.o.t. are in fact non-polynomial and of order strictly less than $a^2$ in the limit $a \to \infty$. From the above expansion we can derive the corresponding expansion for $v(a)$, namely

$$v_{s_\pm}(a) \quad = \quad \tilde{c}_{0,v} + \tilde{c}_{1,v}\left(\frac{1}{\kappa_o a} + \frac{1}{\kappa_w a}\right) + \tilde{c}_{2,v}\left(\left(\frac{1}{\kappa_o a}\right)^2 + \left(\frac{1}{\kappa_w a}\right)^2\right) + \text{h.o.t.},$$

where the h.o.t. are non polynomial in $1/a$. Since $4\pi a^2 v(a) = V(a)$, we have the following identities

$$\begin{aligned} 4\pi(\kappa_o^2 + \kappa_w^2)\tilde{c}_{2,v} &= \kappa_o^2\kappa_w^2\tilde{c}_{0,V}; \\ 4\pi\tilde{c}_{1,v} &= \kappa_o\kappa_w\tilde{c}_{1,V}; \\ 4\pi\tilde{c}_{0,v} &= (\kappa_o^2 + \kappa_w^2)\tilde{c}_{2,V}, \end{aligned}$$

which relate the two types of expansion coefficient.

### 5.3.2 Approximations and Derivation of the Final Model

In most situations we may neglect the $1/(\kappa_w a)$ term, since it is much smaller than 1 and $1/(\kappa_o a)$. In that case we may rewrite the above as

$$\begin{aligned} V_{s_\pm}(a) &= \tilde{c}_{0,V} + \tilde{c}_{1,V}(\kappa_o a) + \tilde{c}_{2,V}(\kappa_o a)^2 + \text{h.o.t.}; \\ v_{s_\pm}(a) &= \tilde{c}_{0,v} + \tilde{c}_{1,v}\left(\frac{1}{\kappa_o a}\right) + \tilde{c}_{2,v}\left(\frac{1}{\kappa_o a}\right)^2 + \text{h.o.t.}, \end{aligned}$$

where the expansion coefficients are appropriately modified and we have the following identities

$$\begin{aligned} 4\pi\tilde{c}_{2,v} &= \kappa_o^2\tilde{c}_{0,V}; \\ 4\pi\tilde{c}_{1,v} &= \kappa_o^2\tilde{c}_{1,V}; \\ 4\pi\tilde{c}_{0,v} &= \kappa_o^2\tilde{c}_{2,V}. \end{aligned}$$

Empirically, it turns out that we can rewrite this to

$$V_{s_\pm}(a) \quad = \quad \pm c_{0,V} \pm c_{1,V}(\kappa_o a) + c_{2,V}(\kappa_o a)^2; \tag{5.1}$$

$$v_{s_\pm}(a) \quad = \quad v_{s_\pm}(\infty) \pm v_{(s_\pm=0)}(\infty)\left(c_{1,v}\left(\frac{1}{\kappa_o a}\right) + c_{2,v}\left(\frac{1}{\kappa_o a}\right)^2\right), \tag{5.2}$$

with

$$\begin{aligned} 4\pi v_{(s_\pm=0)}(\infty)c_{2,v} &= \kappa_o^2 c_{0,V}; \\ 4\pi v_{(s_\pm=0)}(\infty)c_{1,v} &= \kappa_o^2 c_{1,V}; \\ 4\pi v_{s_\pm}(\infty) &= \kappa_o^2 c_{2,V}. \end{aligned}$$

The plus-minus signs in Eq. (5.1) and (5.2) indicate the type of system we are modelling, WO (+) and OW (−). The expansion coefficients $c_{i,v}$ are extremely well-behaved as we will see in the upcoming sections, for typical system parameters $c_{i,v} = \mathcal{O}(1)$. However, we will also find that this reduced[1] polynomial expansion will have diverging coefficients for other system parameters.

### 5.3.3 Coefficient Determination.

We can determine the coefficients $c_{i,v}$ by means of the expansion in Eq. (5.1), which is a polynomial of degree two. Solving the Poisson Equation in the spherical geometry for three droplet radii $a$, keeping all other parameters fixed gives us sufficient information to determine $c_{i,V}$ for $i \in \{0,1,2\}$.[2] Using the third equality we can immediately extract the physical quantity's value in the planar approximation, i.e. $v_{s_\pm}(\infty)$. This will prove a useful tool to determine whether the expansion can be applied for a certain range in parameter space, if not then the extracted planar and the analytical planar value will differ significantly. If we have a step self-energy potential, i.e. $s_\pm = 0$, we can also determine $c_{1,v}$ and $c_{2,v}$ form the three data points, since the expansion reduces to

$$
\begin{aligned}
V(a) &= \pm c_{0,V} \pm c_{1,V}(\kappa_o a) + c_{2,V}(\kappa_o a)^2; \\
v(a) &= v(\infty)\left(1 \pm c_{1,v}\left(\frac{1}{\kappa_o a}\right) + c_{2,v}\left(\frac{1}{\kappa_o a}\right)^2\right).
\end{aligned}
$$

Unfortunately, if $s_\pm \neq 0$, we need to repeat the calculation for the $s_\pm = 0$ system, i.e. repeat the spherically symmetric calculation for the three original data points with the step self-energy potential. We can then use these three new data points to extract $v_{(s_\pm=0)}(\infty)$, in order to determine $c_{1,v}$ and $c_{2,v}$ from the data for the $s_\pm \neq 0$ system. A slightly less elegant way is to determine $v_{(s_\pm=0)}(\infty)$ using the algebraic expression derived earlier and then apply linear algebra to determine $c_{1,v}$ and $c_{2,v}$ from the three original data points. However, doing so eliminates one consistency check.

The usefulness of this method should be clear. As we examine the dependence of $\sigma$ and $\gamma$ on the various system parameters in the upcoming sections we will also consider the expansion coefficients. In the range where this expansion holds, one need only determine the physical quantities in the spherical system for three different radii, keeping the other parameters fixed. Using these three points we can then find the constants and the planar limit, which in turn can be used to interpolate/extrapolate the behaviour of the system for other radii. This will enable us to circumvent tedious and lengthy numerical calculations. Of course, this technique can be applied to experiments as well, where the behaviour predicted by theory is used to interpolate/extrapolate the data obtained from measurements. Finally, the fact that such a polynomial expansion exists gives us insight in the curvature effects which play a role in spherically geometric systems.

---

[1] That is to say, the expansion obtained under the assumption that $1/(\kappa_w a)$ and the h.o.t. can be ignored.

[2] Provided we do so in an area of parameter space where the expansion is valid.

## 5.4 Dependence on the Relative Dielectric Constant of Oil

### 5.4.1 Surface Charge and Tension

The results in this section are based on figures 5.5 and 5.6. In fig. 5.5 the absolute value of the surface charge as a function of $\epsilon_o$ has been given for several droplet radii. Fig. 5.6 shows the surface tension corresponding to the surface charge in fig. 5.6 as a function of $\epsilon_o$.

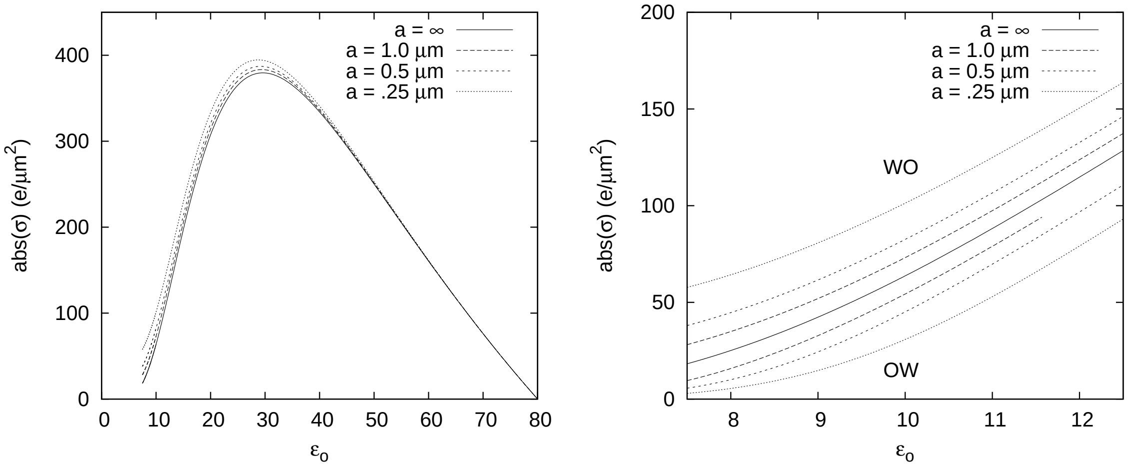

**Figure 5.5:** The absolute value of the surface charge, $\sigma$, as a function of the relative dielectric constant of oil, $\epsilon_o$, for $s_\pm = 0$, $\rho_w = 1.0$ mM and several different droplet radii. The global behaviour showing only WO lines (left) and a small $\epsilon_o$ segment showing both OW and WO lines (right). One of the lines terminates as a result of numerical instability. The surface charge of the OW system is positive and that of the WO system is negative because of the preferential partitioning of the ions.

We observe that the planar surface charge/tension tends to zero in the limits $\epsilon_o \downarrow 1$ and $\epsilon_o \uparrow \epsilon_w$. This can be easily verified by considering the solution to the Poisson Equation in the planar limit approximation. We also find that there is an extremal value in $\sigma$ and $\gamma$ at $\epsilon_o \approx 30$ and $\epsilon_o \approx 20$ respectively. This extremum can be explained as follows. There is a competition between two effects, the first is the difference between oil and air/vacuum ($\epsilon_o \downarrow 1$), the second is the difference between oil and water ($\epsilon_o \uparrow \epsilon_w$). As $\epsilon_o \uparrow \epsilon_w$ the system approaches a situation in which there is a water-water interface. Naturally, there will be no surface charge or tension at such an 'interface' and hence $\sigma$ and $\gamma$ should both vanish. On the other hand, if $\epsilon_o \downarrow 1$ the system will reach a water-air/vacuum interface. Since the ionic density in air/vacuum is negligible as there are no electrostatic effects[3], there is no preferential partitioning, which means that $\sigma$ and $\gamma$ tend to zero in this limit. In between these two limiting cases, the increase in salt concentration in oil ($\epsilon_o \uparrow \epsilon_w$) will tend to increase $|\sigma|$ and $|\gamma|$, whereas the decrease in self-energy difference will tend to decrease these quantities. Similarly, for $\epsilon_o \downarrow 1$ we find that the self-energy difference increases, but the ion density in the oil decreases, inducing a corresponding increase and decrease in $|\sigma|$ and $|\gamma|$. Therefore, there must be an $\epsilon_o$ in the $[1, 80]$ range for which there is

---

[3] Note that this is the case for the model used to describe oil-water interfaces in this thesis. In Ref. [13] a different model is presented to describe oil-air interfaces. In this model such an interface does have a surface tension, which is induced by image charge effects.

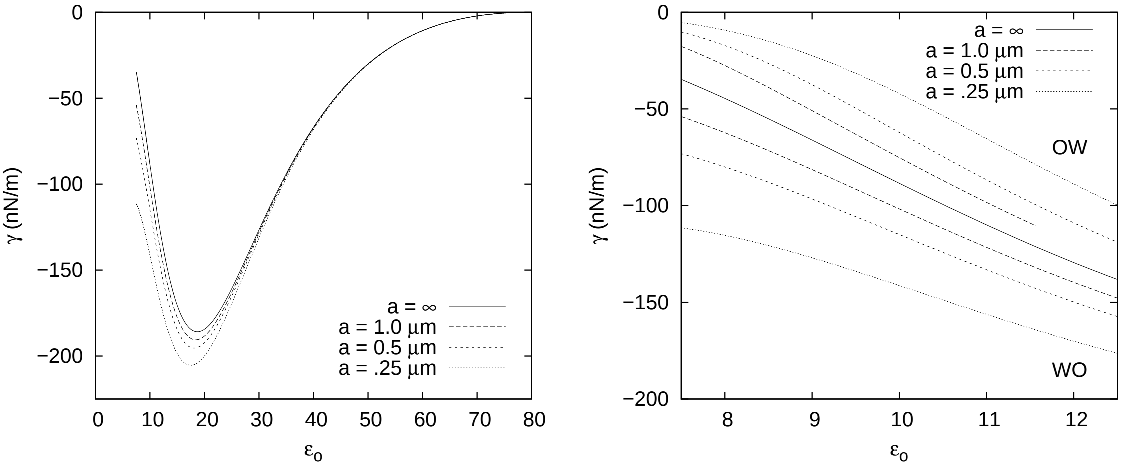

**Figure 5.6:** The surface tension, $\gamma$, as a function of the relative dielectric constant of oil, $\epsilon_o$. The systems are the same as in fig. 5.5. For both OW and WO emulsions $\gamma$ has the same sign, see the left-hand graph. It should be noted that for the $s_{\pm} = a_{\pm}$ emulsion the spherical curves surround the planar excess surface tension, see fig. 5.8, in much the same way they surround the planar $s_{\pm} = 0$ value of $\gamma$.

an extremum. The location of the extremum for $\sigma$ and for $\gamma$ will differ, because both quantities scale differently with $\epsilon_o$.

Figures 5.5 and 5.6 also show the effects of curvature, which influences the system in a non-trivial way. As in section 5.2 we can see that for OW emulsions $|\sigma|$ and $|\gamma|$ are reduced, whereas for WO emulsions they are increased with decreasing $a$/increasing curvature. This increase-decrease asymmetry can be explained by the effects of curvature. Also, we find that the OW and WO curves lie almost symmetrically around the planar curve for sufficiently high $\epsilon_o$, whereas for lower values of $\epsilon_o$ there is a positional asymmetry in the OW and WO curves w.r.t. the planar curve. This asymmetry can be explained by the difference in oil-water screening length, which becomes more pronounced with decreasing $\epsilon_o$ and is similar in origin to the behaviour asymmetry observed in section 5.2. More remarkable is the fact that, although $\sigma$ and $\gamma$ reduce to zero when $\epsilon_o \downarrow 1$ in an OW emulsion with $a \neq \infty$, for and WO emulsion these quantities appear[4] to level-off to a non-zero constant value when $\epsilon_o \downarrow 1$. This means that the value of $\sigma$ or $\gamma$ as calculated by solving the spherical Poisson Equation may differ from that determined in the planar approximation by over a factor of five. Such a significant difference illustrates the necessity of working in the spherical geometry, especially for oils with a low dielectric constant.

There are now three things we need to consider for the extrapolated limiting behaviour in WO systems. One, since the system is quite extreme in the limit $\epsilon_o \downarrow 1$, e.g. the oil Debye-length diverges, whereas the oil ion concentration vanishes, it is quite possible that the perceived effects are numerical in nature. Two, since physically speaking our model does not predict electrostatic effects, i.e. surface charge and surface tension, for $\epsilon_o \downarrow 1$ our extrapolation to $\epsilon_o = 1$ may not be valid. For small droplets, i.e. $\kappa_w^{-1} \approx a$, one expects that the surface energy scales with $a^3$.

---

[4] The choice to restrict the $\epsilon_o$-range to $[7.5, 80]$ was made purely in the interest of numerical precision and time conservation. Some results have been extended to lower values of $\epsilon_o$, $\epsilon_o \approx 3.5$, but this is extremely time consuming and it does not reveal a significant deviation from the results one would expect by extrapolating the curves in figures 5.5 and 5.6.

As most terms in the integrand of Eq. (4.4) will tend to constants, we are left with a volume integral over a constant. In this limit we find $\gamma \propto a$, but for the $\epsilon_o$ considered here we are not in this regime yet. Therefore, one may encounter a cross-over in the behaviour of $\sigma$ and $\gamma$ for $\epsilon_o$ close to 1, allowing both of these quantities to vanish. Three, many electrostatic parameters are a function of $1 - 1/\epsilon$, in that sense the $\epsilon_0 \in [1, 2]$ range is much 'larger' than the $\epsilon_0 \in [2, 7.5]$ range. This is another strong argument against blindly extrapolating the above data. Further investigation is required to determine the effects of curvature in the $\epsilon_o \downarrow 1$ limit.

### 5.4.2 Expansion Coefficients

Using the recipe given in the previous section, we examine expansion coefficients for the systems of figures 5.5 and 5.6. In fig. 5.7, the expansion coefficients $c_{1,v}$ and $c_{2,v}$ have been given, for both the step and the weighted self-energy potential. We have chosen five data points, namely $a$ = 0.0625, 0.125, 0.25, 0.5 and 1.0 $\mu$m, to determine the coefficients in order to increase numerical accuracy. Three points would have been sufficient.

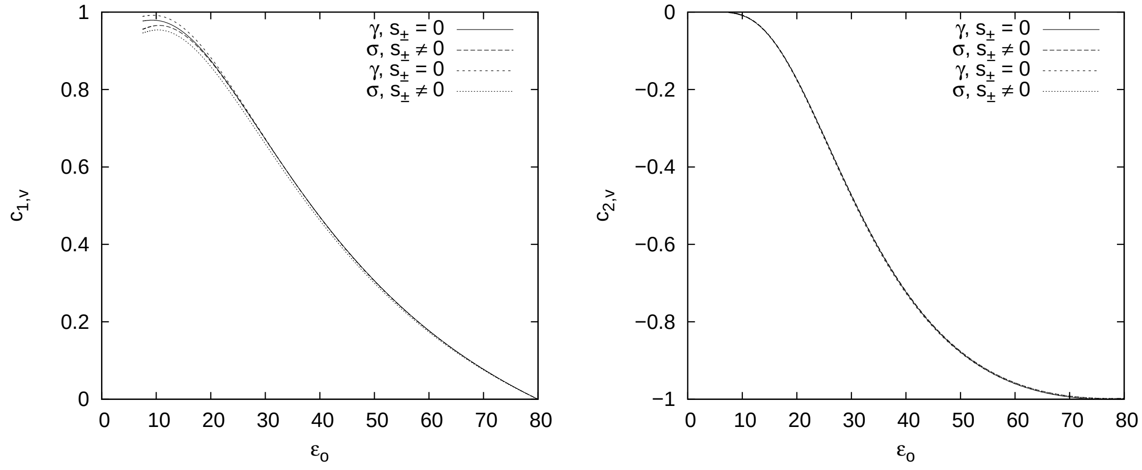

**Figure 5.7:** The coefficients $c_{1,v}$ (left) and $c_{2,v}$ (right) for a WO system only. The coefficients have been determined by fitting Eq. (5.1) to the charge and surface energy for five values of $a$, namely 0.0625, 0.125, 0.25, 0.5 and 1.0 $\mu$m. Note that there is excellent agreement between the various coefficients, i.e. those for $s_\pm \neq 0$ and $s_\pm = 0$ are virtually the same and those for $\gamma$ and $\sigma$ are almost identical. This seems to hold especially true for $c_{2,v}$. OW coefficients have not been included because of numerical problems encountered in their determination for low $\epsilon_o$ and because they are roughly the same as the WO coefficients for $\epsilon_o > 12$.

From fig. 5.7 we can see that in the case of a WO emulsion the coefficients are nearly identical for all parameters we have considered here, i.e. $\sigma$, $\gamma$, $s_\pm = 0$ and $s_\pm = a_\pm$. Furthermore, all coefficients are restricted to the $[-1, 1]$ range and they do not change sign. This, in addition to the close correspondence between the extracted planar limit value and the analytically determined planar value is convincing evidence that our expansion model works. See fig. 5.8, showing the planar excess surface tension in case of a weighted self-energy potential, for an example of this close correspondence.

In fig. 5.7 there seems to be a shift from linear to quadratic deviation from the planar value

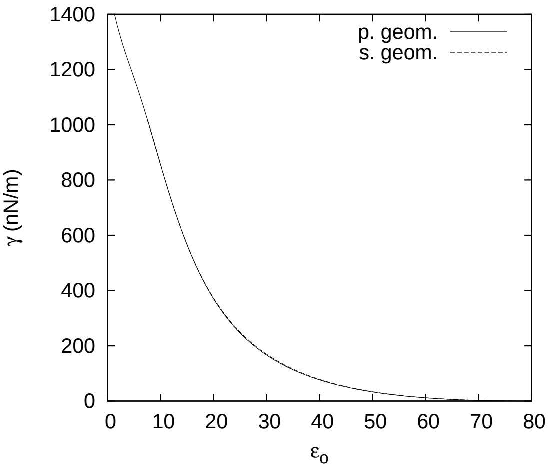

**Figure 5.8:** The surface tension, $\gamma$, as a function of $\epsilon_o$. The system is the same as the planar emulsion in fig. 5.5 with the exception that $s_{\pm} = a_{\pm}$. The continuous line represents $\gamma$ as obtained from the analytic calculation, whereas the dashed line represents the planar limit, which was extracted from results obtained in the spherical geometry. Notice the remarkable correspondence between the two sets of data, a strong indication that the coefficient extraction technique works.

for increasing $\epsilon_o$, this can also be seen in figures 5.3 and 5.4. We can conclude that there are two effects at play, both related to curvature, corresponding to the linear and quadratic term in Eq. 5.2. One scales as $1/(\kappa_o a)$ and is related to the difference in $\epsilon_o$, or rather the difference in Debye-length between the two media. The stronger this difference, the more pronounced the self-energy difference will be and the second effect will be relatively weaker. This first effect is related to the deformation of the double-layer w.r.t. its planar configuration. The second effect, scaling as $1/(\kappa_o a)^2$, is related to the fact that $\phi(0) \neq 0$ in a finite droplet. This becomes more apparent when the two media have similar $\epsilon$ and hence $\kappa$, because the stronger effect of double-layer modification is relatively weaker. However, one should be careful when comparing both terms, i.e. $c_{1,v}$ and $c_{2,v}$, since one would need to divide the latter by $\kappa_o a$ to make a fair comparison.

There are several reasons for not having included the coefficients for OW systems here as well. As one can see form the right-hand side of figures 5.5 and 5.6, the asymmetry between OW and WO systems seems to vanish above $\epsilon_o \approx 12$. That is to say, the coefficients are roughly the same from $\epsilon_o = 12$ on. The difference in sign has been included in Eq. (5.2). Below $\epsilon_0 = 7.5$ there are numerical problems with the implementation of the algorithm we use to investigate these systems. It becomes apparent form figures 5.1 and 5.2 that the limiting behaviour of OW and WO systems is the same, i.e. they approach a common planar value with the same tangent. This leads us to believe that the coefficients are in fact the same, but the range over which the expansion holds is not. At low $\epsilon_o$ with droplets in the $0 - 2$ $\mu$m range, the finite size effects we could safely ignore for WO emulsions dominate in OW emulsions. This is illustrated by the behaviour asymmetry which is clearly visible in the above figures.

We find that $\kappa_o a > 1$ is a sufficient condition to be able to use the expansion of Eq. (5.2) for an OW system. The reason that we do not see such an effect for the WO emulsions is that here $\kappa_o(R-a) > 1$, because we are working in an infinite sized Wigner-cell. This hypothesis explains the behaviour observed in figures 5.1 and 5.2. It could well be that in addition to the requirement that the oil area is at least one oil Debye-length in size, we also require that the water area is at least one water Debye-length in size. Fortunately, $\kappa_w^{-1} = 9.6$ nm for $\rho_w = 1.0$ mM, making it a condition which is easily met. One indeed finds that the correspondence between value of the physical parameters predicted by Eq. (5.2) and the value found by solving the Poisson Equation is lost for such small sized cells, when fitting the expansion coefficients to the data in figures 5.3 and 5.4. However, it may be possible to use the expansion for smaller droplet radii by including $1/(\kappa_w a)$ and $1/(\kappa_w a)^2$ terms in the expansion and redetermining the coefficients. We discuss such small droplets in more detail, when we consider finite sized Wigner-cells in the next chapter. It should be clear that the requirement that $a > \kappa_o^{-1}$ is rather restrictive on the usefulness of the expansion technique for OW systems, since for $\rho_w = 1.0$ mM and $\epsilon_o = 5$ we require $a > 8.43$ $\mu$m.

## 5.5 Ion Concentration in Water

### 5.5.1 Physical Quantities in the Spherical Geometry

Now that we have examined the $\epsilon_o$ dependence of these coefficients, it is natural to proceed by examining the dependence of the physical parameters on the bulk salt concentration in water, $\rho_w$. To give an indication of the system's behaviour we refer to figures 5.9 and 5.10. In fig. 5.9 we have given the surface charge as a function of $\rho_w$ for several droplet radii, with $\epsilon_o = 7.5$. Fig. 5.10 shows the surface tension as a function of $\rho_w$ for several droplet radii with $\epsilon_o = 7.5$ (left) and the planar $\gamma$ for several $\epsilon_o$ (right).

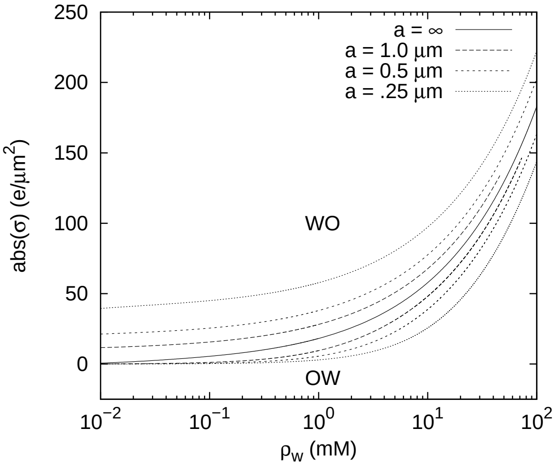

**Figure 5.9:** The surface charge density dependence on the bulk ion concentration in water for several droplet radii, where $s_\pm = 0$. The WO droplets are negatively charged, whereas the OW droplets are positively charged.

We have restricted our attention to the range $[0.01, 100]$ mM, mostly out of numerical considerations. From the planar theory we find that both $\sigma$ and $\gamma$ scale linearly with $-\sqrt{\rho_w}$, which can be seen from fig. 5.10 (right). Note that $\sigma$ and $\gamma$ not only behave similarly under changes

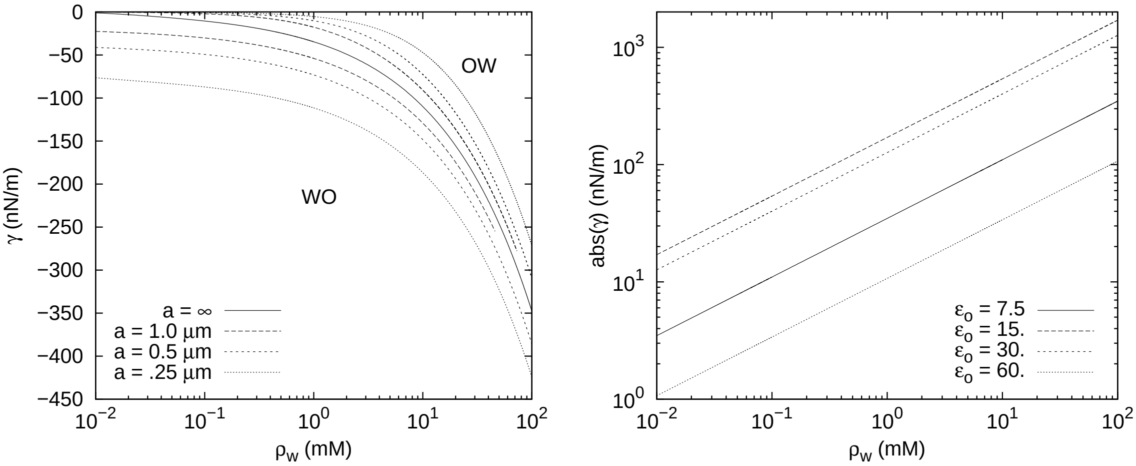

**Figure 5.10:** The surface tension as a function of $\rho_w$ for several droplet radii with $\epsilon_o = 7.5$ (left) and the planar $\gamma$ for several $\epsilon_o$ (right). In both cases we work with a step self-energy potential. The surface tension is negative, and for the planar system we can see that it scales linearly with $-\sqrt{\rho_w}$. Note that the effect of curvature on the surface tension is almost identical to that for the corresponding surface charge, fig. 5.9.

in $\rho_w$ but also under changes in $a$. In fact, the behaviour of these spherical curves w.r.t. their planar counterpart is reminiscent of that found in the previous section, see figures 5.5 and 5.6. This should come as no surprise if the polynomial expansion presented in Eq. (5.2) holds in general. Obviously we should find that the surface charge and tension vanish when the salt concentration tends to zero and this does indeed seem to be the case. However, as we have seen, care needs to be taken when extrapolating results.

In fig. 5.11 the $s_\pm \neq 0$ planar surface tension has been given as a function of $\rho_w$ for several $\epsilon_o$ (left) and $\gamma$ in the spherical geometry (right) for several droplet radii and $\epsilon_o = 7.5$. By comparing fig. 5.10 (right) with fig. 5.11 (left), we see that the effect of a finite $s_\pm$ on the system is to modify $\gamma$ w.r.t. the $s_\pm = 0$ emulsion, specifically its $\rho_w$ dependence. The excess surface tension behaves asymptotically as $\mathcal{O}(-\sqrt{\rho_w})$ for small $\rho_w$ and as $\mathcal{O}(\rho_w)$ for large bulk ionic strength. The former is related to preferential partitioning, whereas the latter is related to a finite interfacial thickness. The effect of curvature is also significant, as it can shift the cross-over point between the two regimes up by multiple decades for WO emulsions. It is not unreasonable to expect such a shift with the introduction of curvature, however, predicting its size using planar theory or the expansion of Eq. (5.2) proves impossible.

Note that our model differs from that described in the work of Bier et al., Ref. [7], as it assigns a different shell-parameter, $s_\pm$, to both species of ion, rather than a single parameter $s$. Furthermore, it uses a weighted rather than a shifted self-energy step-function. In that sense the model presented here does not describe a finite interfacial thickness, but rather a geometric effect depending on the ionic size. However, the behaviour of $\gamma$ turns out to be similar, since the weighted self-energy potential used in this thesis, see fig. 2.5, can be approximated by a step self-energy potential shifted towards the water side of the interface. The most important result is that for large bulk ionic strengths $\gamma$ scales linearly with $\rho_w$. This is in agreement with the few reported measurements of liquid-liquid interfacial tension between two electrolyte solutions, see

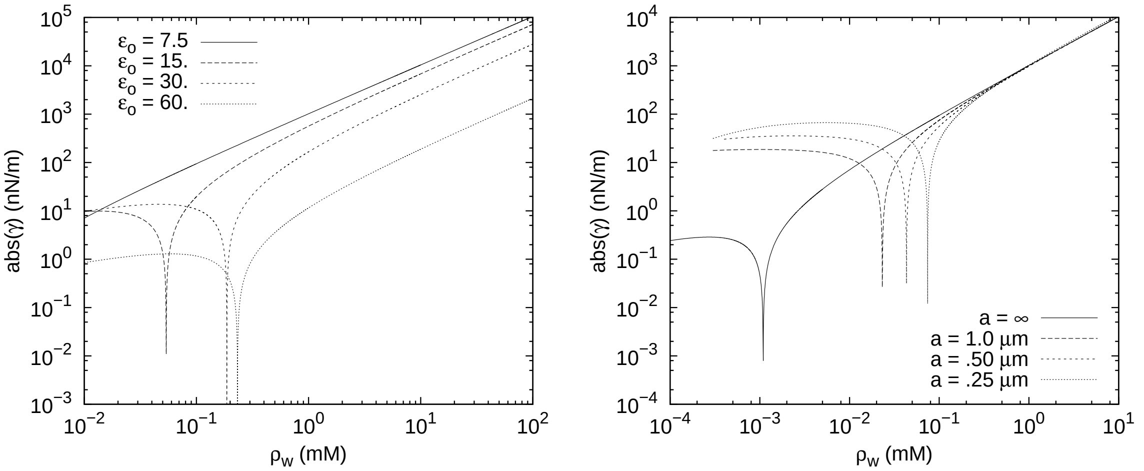

**Figure 5.11:** The planar surface tension dependence on the bulk ion concentration in water, for several different $\epsilon_o$ (left) and the spherical $\gamma$ for several radii $a$ compared to the planar value at $\epsilon_o = 7.5$ (right). In both cases we have $s_\pm = a_\pm$. From the left graph we can see that the effect of having a smoothed self-energy potential is that for higher salt concentrations $\gamma$ scales linearly with the salt concentration and is positive, whereas for low salt concentrations $\gamma = \mathcal{O}(-\sqrt{\rho_w})$. We have only included WO lines here, because the algorithm is unstable for low salt concentration in OW emulsions.

for instance Ref. [14].

### 5.5.2 Ionic Density and Expansion Coefficients

In fig. 5.12 the first coefficient in the expansion of Eq. (5.2) corresponding to the system of fig. 5.10 (left) have been given. On the left-hand side we have $c_{1,\gamma}$ for emulsions with the step self-energy potential and on the right-hand side with the weighted potential. The associated second expansion coefficients have been given in fig. 5.13.

Using this data we may examine the properties of the expansion coefficients of Eq. (5.2) as a function of the density. For high bulk salt concentrations the coefficients become constant in case $s_\pm = 0$. That is to say, the coefficients remain roughly the same for $\rho_w > 0.1$ mM and $a > 0.0625$ $\mu$m. Here we take $\rho_w > 0.1$ as an estimate, where we have ignored the $\epsilon_o = 7.5$ line, because of the strong deviation between the analytical and extracted planar value for these systems, see fig. 5.14 (right).

This deviation can in part be explained by numerical uncertainty, and in part by failure to choose droplet radii for which the expansion can be used. That is to say, there exists some criterion for the use of the expansion, depending on $\rho_w$, $\epsilon_o$ and $a$, which is violated. This criterion is violated most likely for the smallest $a$ used to determine these coefficients, $a = 0.0625$ $\mu$m. The second coefficients seem to exhibit slightly more $\rho_w$ dependence, but from $\rho_w > 1.0$ mM on they too hold steady. This difference can be explained by numerical uncertainty, to which $c_{2,v}$ is more susceptible than $c_{1,v}$. The origin of this uncertainty is most likely systematic. Further study of the system reveals that the coefficients remain constant for smaller salt concentrations as well, under the condition that the expansion is to be used for larger $a$. This is exactly

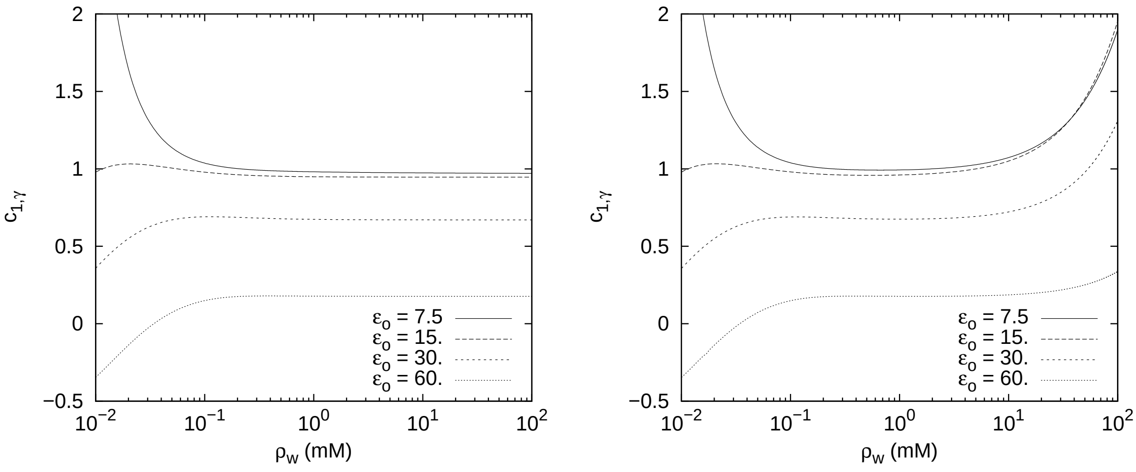

**Figure 5.12:** The first coefficient, $c_{1,\gamma}$, for $s_\pm = 0$ (left) and $s_\pm = a_\pm$ (right). Both have been calculated by means of Eq. (5.1) using $a = 0.0625$, 0.125, 0.25, 0.5 and 1.0 $\mu$m. The coefficient $c_{1,\sigma}$ is similar to $c_{1,\gamma}$ in the left graph for both $s_\pm = 0$ and $s_\pm = a_\pm$ and has therefore not been included here. We believe that for the left-hand graph the expansion coefficient is nearly independent of $\rho_w$ for high salt concentration and that the lines can be safely extended to $\rho_w = 10$ M. The deviation form this constant value for low $\rho_w$ is a combination of a break-down of the expansion of Eq. (5.2) and in part numerical uncertainty, see fig. 5.14. For the right graph the expansion coefficients diverge at high $\rho_w$.

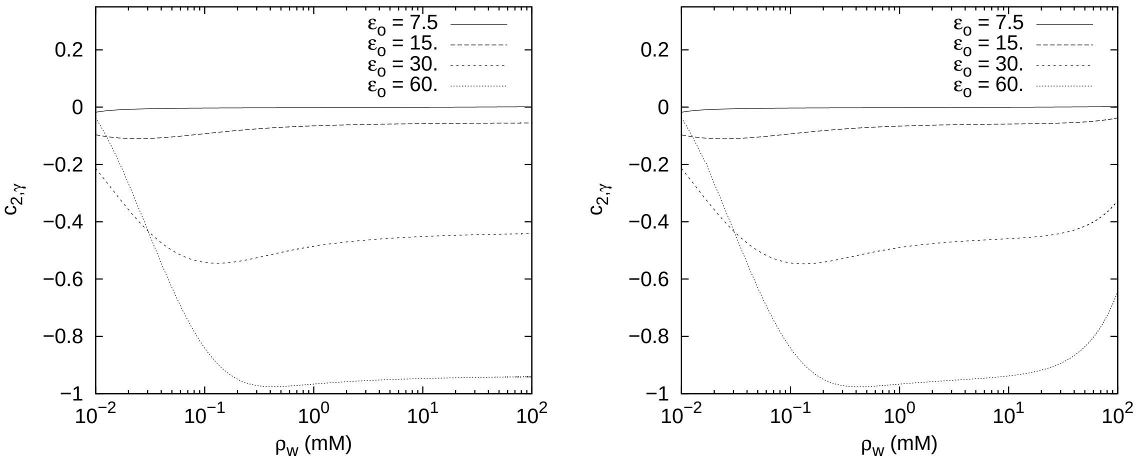

**Figure 5.13:** The second coefficient, $c_{2,\gamma}$, in case $s_\pm = 0$ (left) and $s_\pm = a_\pm$ (right). Again $c_{2,\sigma}$ behaves as $c_{2,\gamma}$ in the left-hand graph. Here too there seems to be a constant value for high bulk salt concentration coupled with a break-down of the expansion at low concentrations. The $s_\pm = a_\pm$ system's $c_{2,\gamma}$ shows the same type of deviations at high $\rho_w$ as the corresponding $c_{1,\gamma}$, see fig. 5.12 (right).

what one would expect if there exists such a criterion as mentioned above. There are also good indications, that OW coefficients show similar constancy behaviour, but for substantially higher salt concentrations/radii. The deviation from a constant value for low salt concentration can possibly be attributed to the fact that $1/(\kappa_w a)$ terms, which we have ignored in Eq. (5.2)

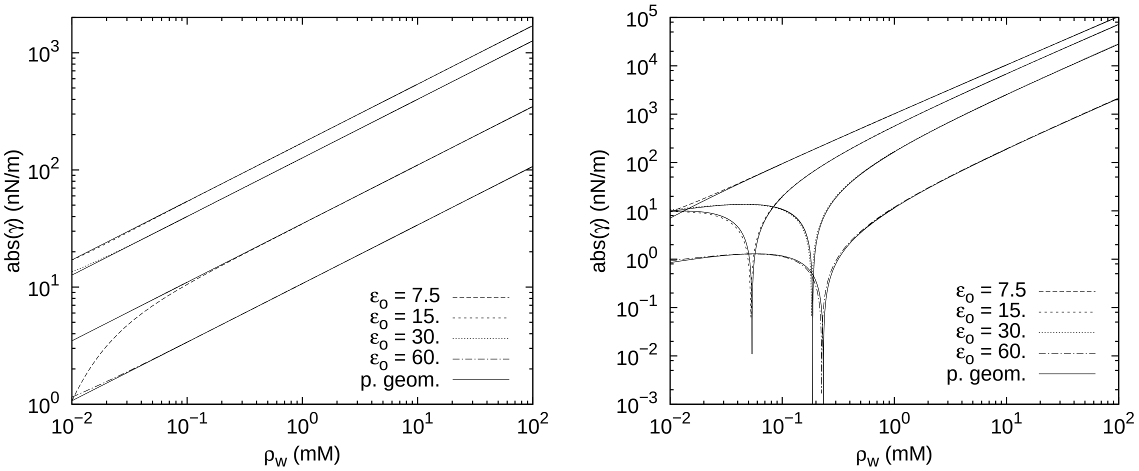

**Figure 5.14:** The extracted planar value compared to the value calculated in the planar limit. The left graph corresponds to the left-hand side of fig. 5.12 and the right graph to the right-hand side of that figure. Note that on the left of both graphs we see that there is a divergence between the extracted and analytical results, which grows for smaller $\rho_w$ and is more pronounced for smaller $\epsilon_o$. On the right of both graphs, i.e. for high $\rho_w$, there is no such effect.

become relevant. For $\rho_w = 0.1$ mM and $\epsilon_o = 7.5$, for instance, we find $1/(\kappa_w a) \approx 0.5$, with $a = 0.0625$ $\mu$m. This 'small' factor can have a sizeable influence on the expansion coefficients.

One could suspect that, because both $\rho_w$ (via $\rho_o$) and $\epsilon_o$ appear in $\kappa_o$, these expansion coefficients are only $\kappa_o$ dependent. This turns out not to be the case. The coefficients are virtually $\rho_w$ independent, provided the appropriate constancy criterion is upheld. This does not, however, negate the validity of the expansion if this criterion is violated, only the fact that the coefficients are constant. Since the point at which the deviations from the constant value occur is not the same for all $\epsilon_o$, we must conclude that the criterion contains some $\epsilon_o$-dependence. One could surmise that $\kappa_o a > 1$ is a sufficient condition, however, this is not the condition for constant coefficients. It does explain the divergence of the coefficients for $\epsilon_o = 7.5$ at low $\rho_w$, see fig. 5.14. We find that the $\rho_w$ for which the coefficient is constant scales as $a^3$ and is seemingly linear with $\epsilon_o$. We thus hypothesise that $\rho_w a^3/\epsilon_o > 1$ is the constancy criterium. This gives us a range of validity for $\rho_w > 0.05$, 0.1, 0.2 and 0.4 mM for $\epsilon_o = 7.5$, 15, 30 and 60 respectively. Here we have used $a = 0.0625$ $\mu$m, the smallest droplet radius employed to calculate the coefficients, as it is most likely to be a limiting factor. These densities appear to be in reasonable agreement with the behaviour of the coefficients in figures 5.12 and 5.13. We must stress that, although the coefficients are not constant when $\rho_w a^3/\epsilon_o < 1$, the coefficients in the expansion are still well-behaved. This is no longer the case when $\kappa_o a > 1$.

Another effect the reader will have noticed on the right-hand side of figures 5.12 and 5.13, is that the expansion coefficients diverge for salt concentrations above roughly 10 mM, when we consider $s_\pm \neq 0$. Still, Eq. (5.2) works well over multiple decades of salt concentration. There are several possibilities for this coefficient divergence. We have taken care to eliminate numerical and systematic errors to the best of our ability and are therefore inclined to believe that this is an actual effect. As can be seen form fig. 5.14 (right) there is no clear deviation between the actual planar and the extracted planar value for $\rho_w > 10$ mM. In fact, for $\epsilon_o = 7.5$

the deviation at $\rho_w = 100$ mM is of the order of 1%. It is therefore quite possible that for high salt concentration the distinction between $s_\pm = 0$ and $s_\pm \neq 0$ effects are not quite as clear cut as is implied in Eq. (5.2). However, due to the limitations of our algorithms we cannot prove such a claim at this time, nor can we exclude numeric/systematic uncertainties.

## 5.6 Variation of the Shell-Parameter

### 5.6.1 The Effects of Curvature

We have examined the dependence of the excess surface tension on the shell-parameter by taking $\rho_w = 1.0$ mM and $\epsilon_o = 7.5$, 15, 30 and 60. The surface tension has been calculated for a WO system only. We we keep $a_+ = 3.6$ Å and $a_- = 3.0$ Å fixed and vary $s_-$ between $0 - 1$ nm, whilst holding $s_+ = a_+$ to determine the effect of shell-size ratio. In another calculation, we hold the ratio $s_-/s_+ = 5/6$ and let $s_-$ run to study the effect of shell-size. Fig. 5.15 shows the difference between the planar value of $\gamma$ and the spherical value, using the above set-up for a weighted self-energy potential and several droplet radii, taking $\epsilon_o = 7.5$.

One can see that the deviation form the planar value is linear in $1/a$, within the parameter range we have studied here. We have also seen this behaviour for the relative dielectric constant of oil and the bulk ion density in water. We surmise that the linear part of the expansion in $1/a$ dominates the quadratic part for all physically relevant systems. For OW emulsions a similar deviation can be observed. As remarked earlier, this $1/a$ scaling can be explained by the way the double-layer is affected w.r.t. the planar double-layer by the introduction of curvature. We must stress that only the electrostatic contribution is modified significantly in the spherical geometry, the self-energy contribution near the interface is hardly altered. Since weighting the potential does not significantly influence the surface charge we have not considered it in this section.

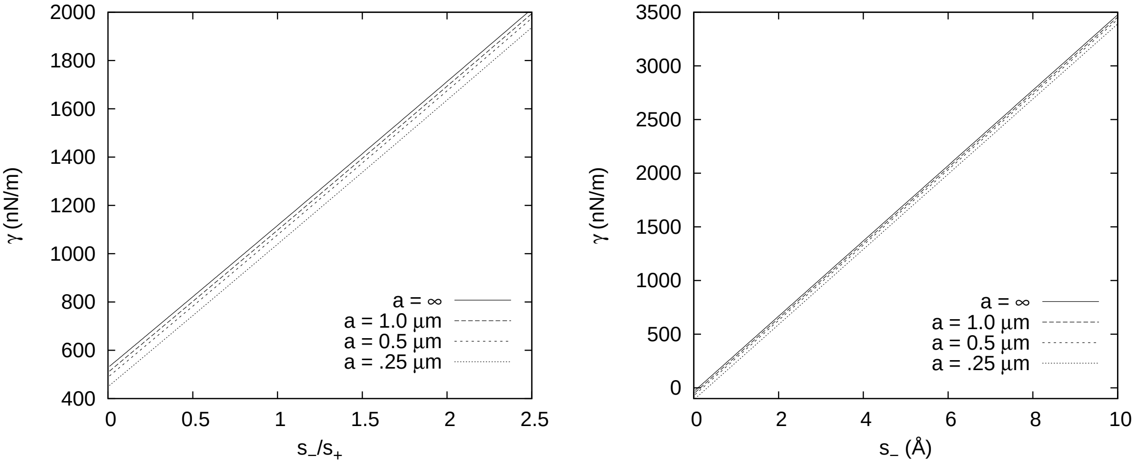

**Figure 5.15:** A comparison between the planar value of $\gamma$ and the value calculated in the spherical geometry for several different droplet radii, as a function of the ratio $s_-/s_+$ for $s_+ = 3.6$ Å (left) and as a function of $s_-$ for $s_-/s_+ = 5/6$ (right). Here $\rho_w = 1.0$ mM, $\epsilon_o = 7.5$, $a_+ = 3.6$ Å and $a_- = 3.0$ Å. Only WO emulsions have been considered.

Fig. 5.16 gives the planar $\gamma$ as a function the shell-parameters for a series of $\epsilon_o$, using the aforementioned procedure. From the right-hand graph we can see that for vanishing shell-parameter we indeed retrieve the surface tension for the step self-energy potential. Furthermore, we can see that the deviation from the $s_\pm = 0$ value of $\gamma$ is linear in both $s_+$ and $s_-$, independent of $a$ (fig. 5.15), $\epsilon_o$ (fig. 5.16) and $\rho_w$ (for which we have not included a graph). This linearity follows directly from the theory, since the size of $s_\pm$ linearly influences the size of the non-electrostatic contribution to the excess surface tension. In the next chapter this will become more clear. Note that this linearity is also found in the work of Bier et al., Ref [7].

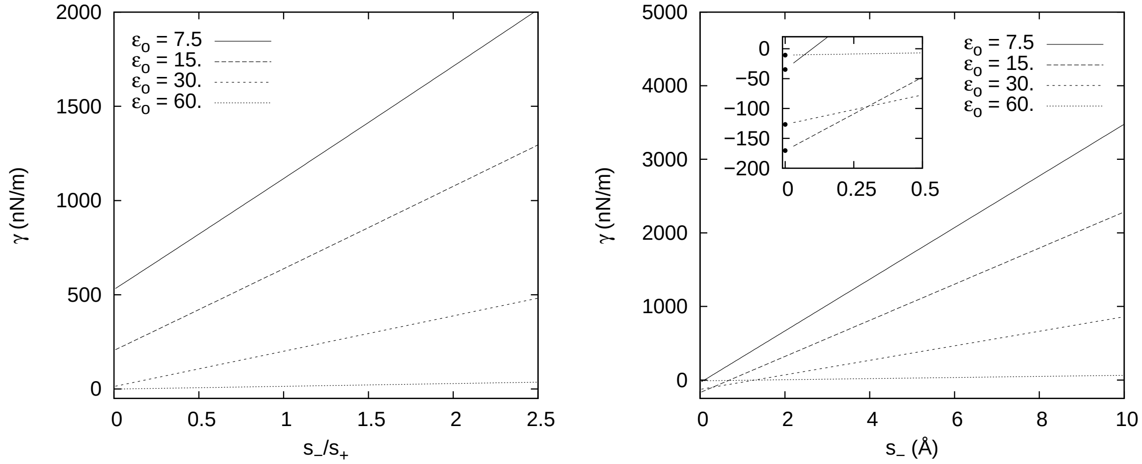

**Figure 5.16:** The extracted planar surface tension, $\gamma$, as a function of $s_-/s_+$ for $s_+ = 3.6$ Å fixed (left) and as a function of $s_-$ for $s_-/s_+ = 5/6$ (right). The systems are the same as in fig. 5.15, with the exception that a series of $\epsilon_o$ have been used instead of a series of droplet radii. The values calculated for the $s_\pm = 0$ system have been indicated using dots in the insert of the right figure. The two graphs together show that both shells $s_+$ and $s_-$ contribute to the surface tension, not just the largest one. Moreover, this contribution is linear in both arguments.

### 5.6.2 Expansion Coefficients

Using the familiar series of radii $a = 0.0625$, 0.125, 0.25, 0.5 and 1.0 $\mu$m, we have determined the expansion coefficients corresponding to the systems of fig. 5.16. Fig. 5.17 shows the first expansion coefficient and fig. 5.18 shows the second expansion coefficient. From these figures it becomes clear that for fixed $a_\pm$ the choice of shell-parameter does not significantly alter the coefficients. This indicates that at least for the parameters we have examined the expansion in Eq. (5.2) can be used. That is to say, the coefficients do not diverge. A possible source for the slight deviations from a constant value for $c_{\gamma,i}$ is the changes induced in the self-energy contribution to $\gamma$ by curvature, since we have ignored such effects in Eq. (5.2).

In figures 5.17 and 5.18 we only show the coefficients for the excess surface tension. The coefficients for the surface charge behave similarly. However, considering the fact that the surface charge remains virtually the same under the transition from step to weighted self-energy potential, they can hardly be considered to be relevant.

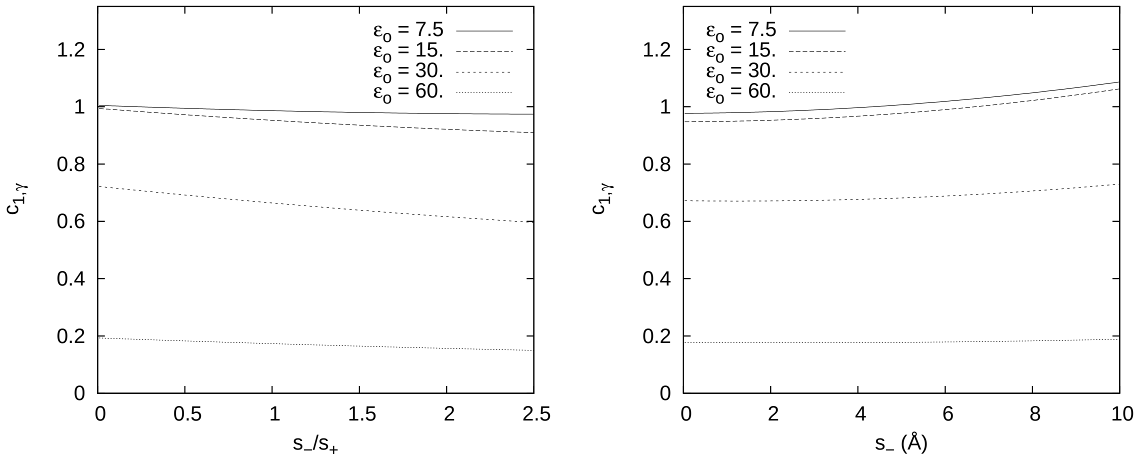

**Figure 5.17:** The coefficient $c_{1,\gamma}$ as a function of the ratio $s_-/s_+$ for $s_+ = 3.6$ Å (left) and as a function of $s_-$ for $s_+ = 3.6$ Å (right). Here $\rho_w = 1.0$ mM and $\epsilon_o = 7.5$, 15, 30 and 60. Note that the coefficient is virtually independent of the ratio of $s_-/s_+$ and the shell-size, for a reasonable choice of parameters. The coefficients have been determined by making use of the data in fig. 5.15.

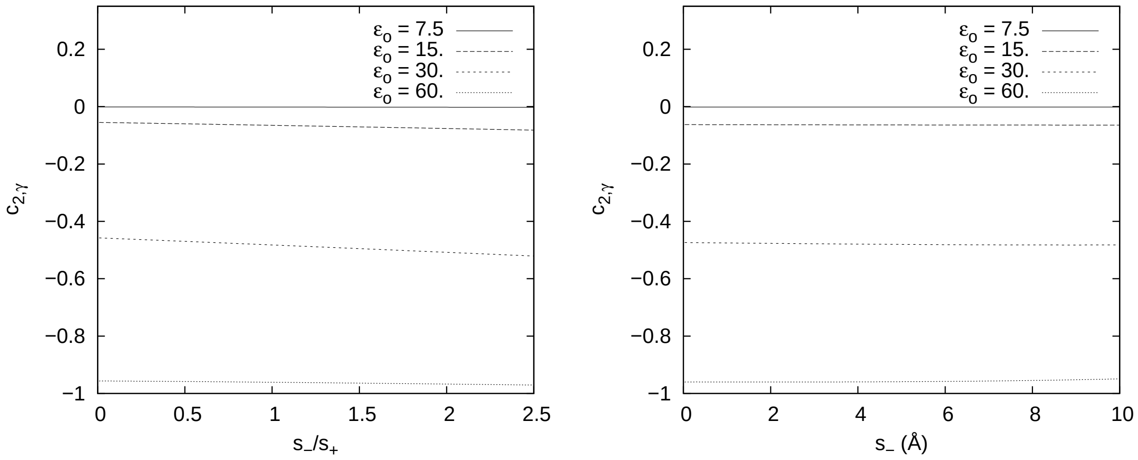

**Figure 5.18:** The second coefficients, $c_{2,\gamma}$, corresponding to $c_{1,\gamma}$, given in fig. 5.17. Note that these coefficients are almost constant, in fact, more so than their $c_{1,\gamma}$ counterparts.

## 5.7 Born Self-Energy Modification via Ion Size Variation

### 5.7.1 The Influence of Ion Size on the Physical Quantities

In this section we follow the same procedure as in the previous section, with the exception that we will now vary $a_\pm$ instead of $s_\pm$. We set $s_\pm = a_\pm$ in the case of a weighted self-energy potential. In fig. 5.19 one can see the extracted planar surface charge as a function of the ionic radii. On the scale of the plot these results are indistinguishable from those of the full numerical calculations. Observe that in the left-hand figure we see that $\sigma$ vanishes as $a_-/a_+ \to 1$. This is caused by the disappearance of preferential partitioning, since the self-energy difference between the two species of ion vanishes.

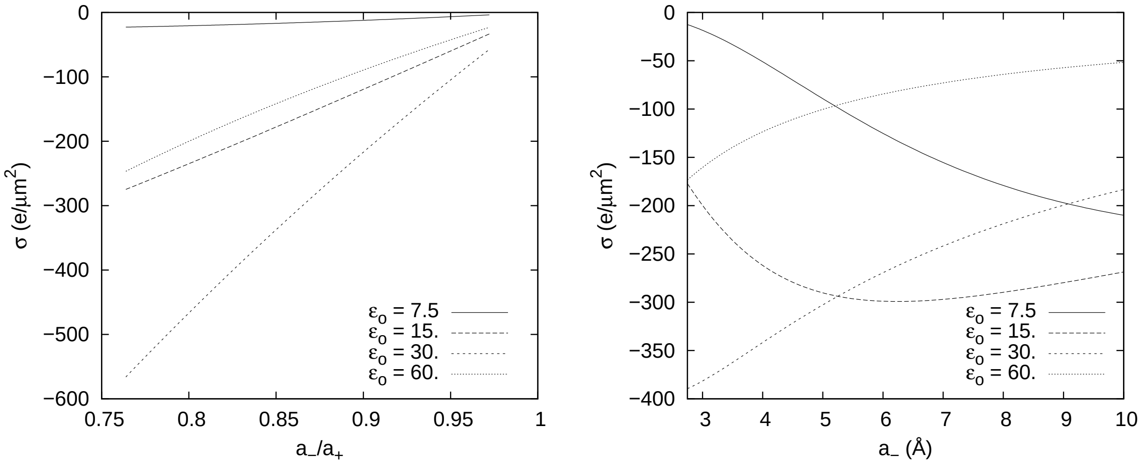

**Figure 5.19:** The extracted planar surface charge, $\sigma$, as a function of the ratio $a_-/a_+$ for $a_+ = 3.6$ Å (left) and as a function of $a_-$ for $a_-/a_+ = 5/6$ (right). Here $\rho_w = 1.0$ mM and $s_\pm = 0$. Comparison with the analytic planar value shows exact correspondence. Left we see the disappearance of preferential partitioning for $a_+/a_- \to 1$, caused by vanishing self-energy difference.

Fig. 5.20 shows the excess surface tension, corresponding to the systems in fig. 5.19, for a self-energy step potential as a function of the ionic radii. Again, the extracted and analytic value of $\gamma$ are indistinguishable on the scale of the plot. The same holds for fig. 5.21, where $\gamma$ is given as a function of the ionic radii, but now for $s_\pm = a_\pm$. By changing one or both ionic radii, the self-energies of the ions are altered. This in turn modifies the bulk ion density in the oil, the Debye-length in the oil/water and the level of partitioning. It is therefore difficult if not impossible to give the physical interpretation of such changes. These results have been included to justify the phenomena we observe when we consider the expansion coefficients and for overall completeness.

Finally, we examine the effects of curvature on the the surface tension. In fig. 5.22 the surface tension is given as a function of the ionic radii for several values of the droplet radius $a$. Again, we find the curvature induced $1/a$ deviation form the planar value.

### 5.7.2 Ionic Radius and Expansion Coefficients

In fig. 5.23 we have examined the $a_\pm$-dependence of the first expansion coefficient. The coefficients found here, have been determined by using the data in figures 5.19-5.21. For the second expansion coefficient we refer to fig. 5.24. From fig. 5.23 we can see that there is a difference in value for $c_{1,\sigma}$ and $c_{1,\gamma}$. We have already seen this is usually the case, but now there is also another difference. The coefficients $c_{1,\gamma}$ appear to diverge in the limit $a_-/a_+ \to 1$, whereas the $c_{1,\sigma}$s do not appear to diverge. It should be noted that for size ratios tending to 1 the system starts to degenerate, because preferential partitioning breaks down. The positive and negative ion self-energies become identical and hence the droplet charge will vanish, see fig. 5.19 (left). Apparently this is does not affect expansion coefficients for the surface charge significantly.

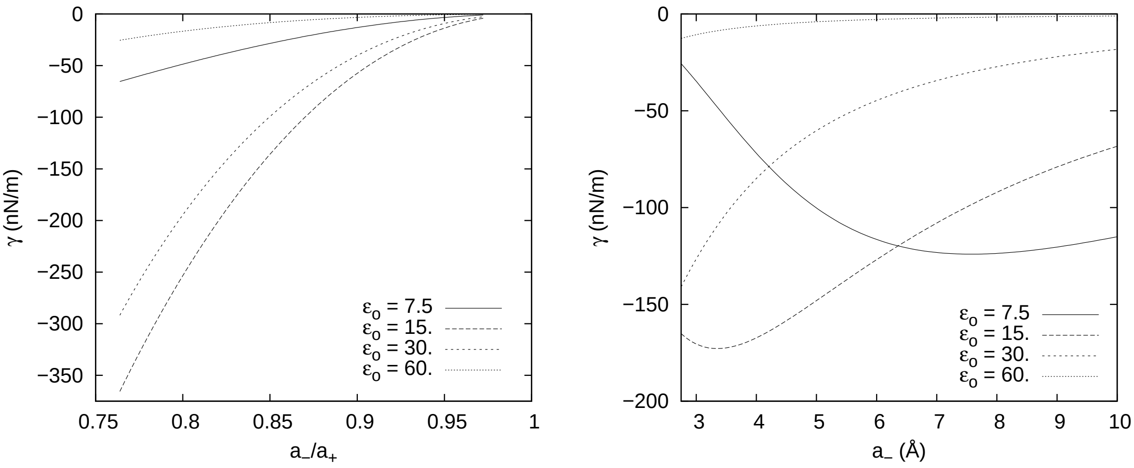

**Figure 5.20:** The extracted planar surface tension, $\gamma$, for $s_{\pm} = 0$. The same system parameters as in fig. 5.19 have been used.

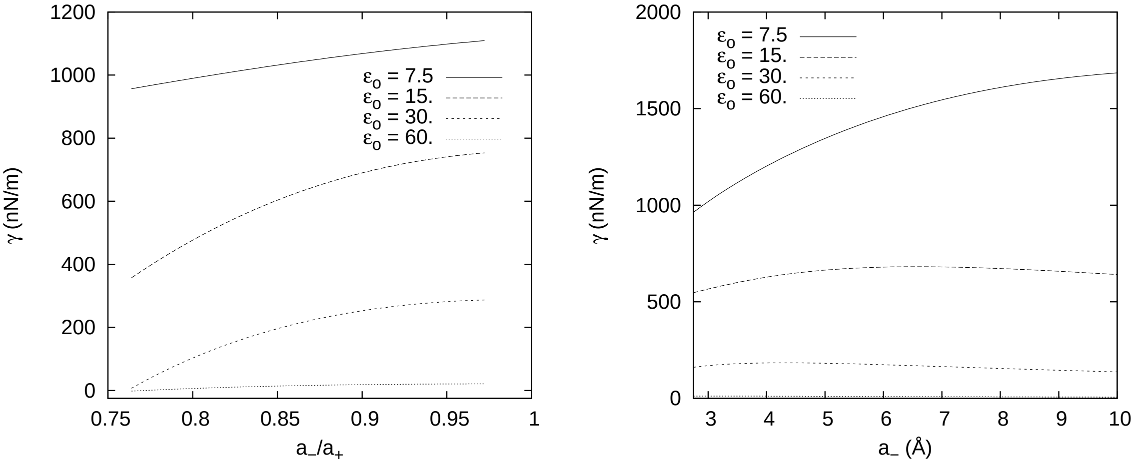

**Figure 5.21:** The extracted planar $\gamma$ for a weighted potential with $s_{\pm} = a_{\pm}$. Otherwise the emulsions are exactly the same as those shown in fig. 5.20.

However, the coefficients for $\gamma$ are definitely influenced. The exact correspondence between the $\gamma$ extracted from the spherical data and the surface tension determined analytically suggests that the divergence is not a numerical artifact. We must therefore take care in using this expansion for ion size ratios tending to 1. However, it will turn out that we are not very interested in $a_-/a_+ \approx 1$. We will come back to this when we discuss crystallisation in the next chapter.

From figures 5.23 and 5.24 it would appear that the expansion coefficients diverge for too low $a_-/a_+$ ratios as well. In fact form this it seems as though we have been working near the edge the parameter regime for which we may apply Eq. (5.2), since there is a strong divergence in $c_{1,\gamma}$ for $a_- < 2.8$ Å and $a_+ = 3.6$ Å. The second coefficient is more well-behaved, fig. 5.24 (right). Unfortunately it is difficult to say what the reason behind the divergence is, since modifying $a_{\pm}$ directly and indirectly influences a whole host of parameters. It appears to be related to $\epsilon_o$ though, i.e. the effect is less prominent for larger $\epsilon_o$. Therefore, $\kappa_o$ is a likely suspect. At this

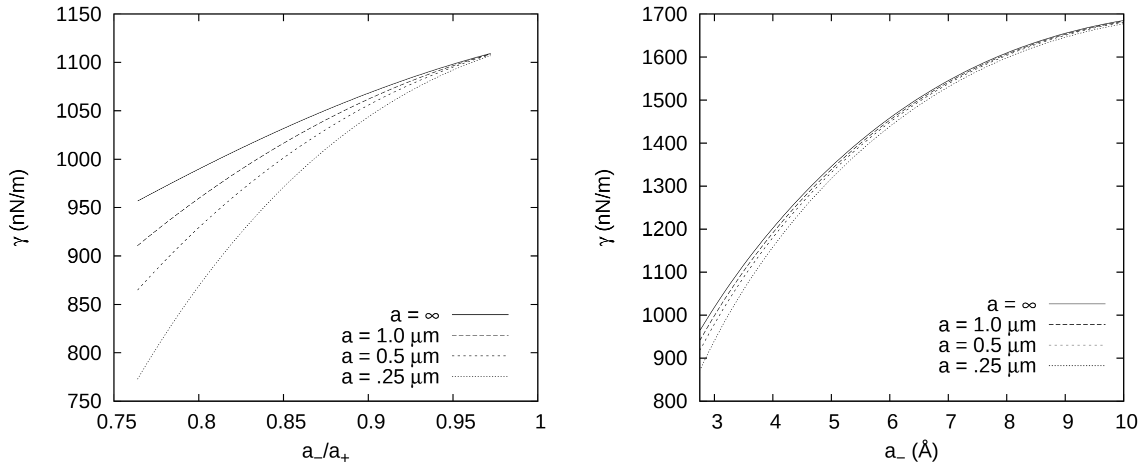

**Figure 5.22:** A comparison between the planar value of $\gamma$ and the value calculated for several different droplet radii, $a$, in the spherical geometry as a function of the ionic radii. Only $\epsilon_o = 7.5$ is considered here, $\rho_w = 1.0$ mM and $s_\pm = a_\pm$. Only WO emulsions have been considered in these graphs, because of numerical difficulties with OW emulsions in our algorithms.

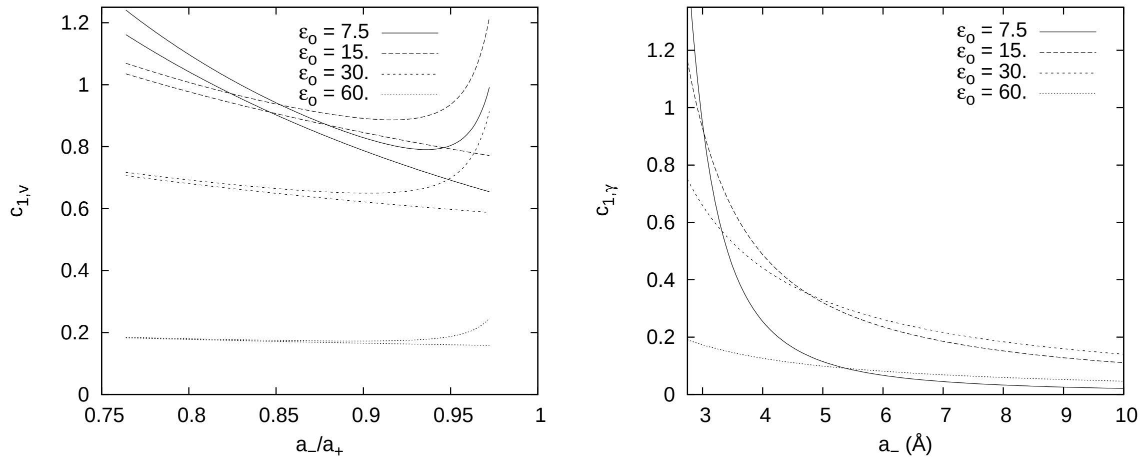

**Figure 5.23:** The coefficient $c_{1,v}$ as a function of the ratio $a_-/a_+$ (left) and as a function of $a_-$ for $a_+ = 3.6$ Å (right). We have used $\rho_w = 1.0$ mM, $\epsilon_o = 7.5$, 15, 30 and 60 and $s_\pm = a_\pm$. Both $c_{1,\sigma}$ and $c_{1,\gamma}$ have been included in the left graph, $c_{1,\sigma}$ is given by the more or less straight lines. We have done so because there is a substantial deviation between $c_{1,\sigma}$ and $c_{1,\gamma}$ in this case. On the right-hand side only $c_{1,\gamma}$ has been included, as $c_{1,\sigma}$ is similar. See fig. 5.22 for the data-sets on which the above graphs are based.

point though, there is not enough data to make any kind of definitive statement with regard to this effect and it would certainly merit further investigation. Note that the expansion can be safely used for $a_- \gg a_+$.

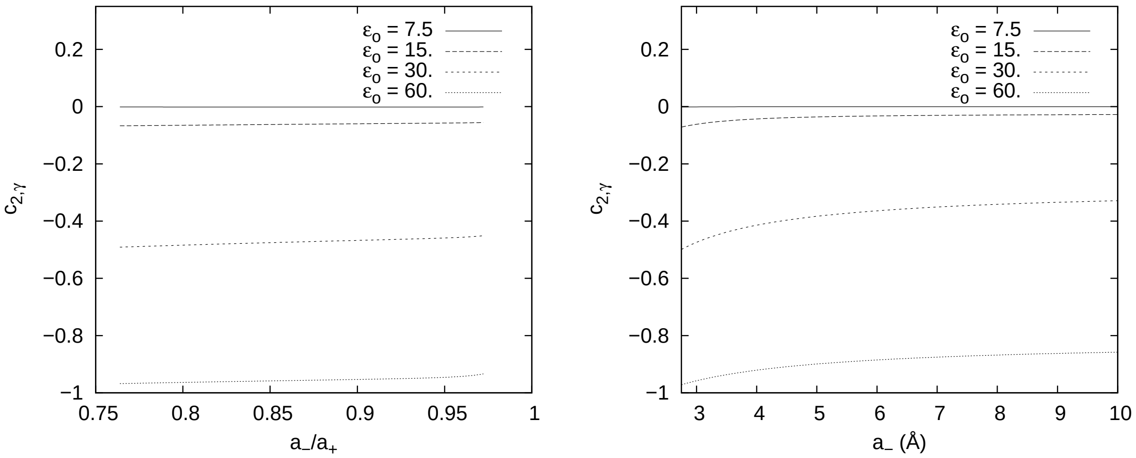

**Figure 5.24:** The second coefficients, $c_{2,\gamma}$ corresponding to the first coefficients given in fig. 5.23. Only the $\gamma$-coefficients have been included, because the $\sigma$-coefficients are similar.

## 5.8 Summary

Let us recap the results we have analysed thus far. We have studied the effects of curvature on the surface charge and the surface tension of oil-water interfaces. From the data gathered we can deduce that modifications in these quantities w.r.t. the value determined in the planar approximation are caused by the deformation of the double-layer under curvature. The results obtained by solving the Poisson Equation in the spherical geometry can differ substantially form those obtained in the analytical approximation of the planar limit. This is especially true for WO emulsions with low oil dielectric constant and low bulk salt concentration in water. Although not much is known about the value of $\rho_w$ in the experiments of Ref. [3], we know that $\epsilon_o$ is small enough, i.e. $4-10$, to warrant a theoretical analysis of these experiments in the spherical geometry. Another example of the importance of the spherically geometric quantities is the significant shift in the cross-over point between $\gamma = \mathcal{O}(-\sqrt{\rho_w})$ and $\gamma = \mathcal{O}(\rho_w)$ compared with the cross-over in the planar approximation for weighted self-energy potentials. It is not unreasonable to expect such a shift, however, quantifying it using only planar results proves impossible, even though the effects can be quite dramatic. Nevertheless, we find that there are large regions of parameter space where the planar approximation is very accurate. We established that $\kappa_o a \gg 1$ is an essential condition to obtain reasonable results form the planar limit approximation.

We have checked if the experimentally observed crystal of water droplets in oil is thermodynamically stable according to our model. This thermodynamical stability is quantified by the difference between the excess surface tension and the regular surface tension. Throughout this chapter we have seen that the excess surface tension, as predicted by our spherically symmetric model for saline emulsions of oil and water, is extremely small compared to regular surface tension found at any oil-water interface. The excess $\gamma$ is at most a couple of hundred $\mu$N/m, in the most favourable case, whereas the regular $\gamma$ is of the order of 1-10 mN/m. Hence the influence of the excess surface tension on the regular tension will not be significant. Using the shell-parameter model, which more accurately models experimental systems, the excess surface tension is positive rather than negative for the parameter regimes used in Ref. [3]. This implies an increase in the droplet's ability to coalesce and the emulsion's tendency to demix by introducing salt to an oil-water emulsion. Therefore, we may rule out true thermodynamic stability of the these emulsions. We will come back to the meta-stable crystallisation observed in Ref. [3] in the next chapter.

The pinnacle of this chapter is the formulation of a polynomial expansion in $1/(\kappa_o a)$, which relates the effects of curvature in the spherical geometry on the value of $\sigma$ and $\gamma$ w.r.t. that found in the planar limit. This expansion captures the essence of the double-layer deformation. We have investigated OW and WO emulsions to determine the regime for which the expansion of Eq. (5.2) can be used. The two expansion coefficients are dependent in various degrees on the system parameters $\rho_w$, $\epsilon_o$, $a_\pm$ and $s_\pm$, but they are well-behaved, i.e. $\mathcal{O}(1)$, under only a few basic assumptions. The definite asymmetry between WO and OW systems, leads us to conclude that we $\kappa_o a > 1$ and to a lesser extent $\kappa_w a > 1$ are criterions, which govern the range of applicability of the expansion.

The advantage of an expansion, which we have shown to have a wide range of applicability, is that we only need to calculate the value of $\sigma$ and $\gamma$ for three radii to determine the behaviour of the system for all $a$. Provided we do so in a part of parameter space, where the polynomial expansion is valid. In addition, knowledge of the behaviour of physical quantities in emulsion droplets enables experimentalists to interpolate/extrapolate data and to check the validity of the theoretical model presented in this thesis. However, it should be noted that, although this expansion can be a powerful tool, it is not the holy grail of saline emulsions in the spherical geometry. It has its limitations, namely a distinct lack of quantitative predictive power without knowledge of the coefficients, which requires solving the Poisson Equation in the spherical geometry to begin with.

# Chapter 6

# Finite Droplet Concentration

## 6.1 Introduction

As we have seen in the previous chapter we can quantify the effects of the spherical geometry in an infinite Wigner-cell by means of expansion in terms of $1/(\kappa_o a)$ w.r.t. the planar geometry. However, when we wish to treat emulsions with a finite droplet volume fraction the situation changes. In this chapter we will consider a finite Wigner-Seitz cell to describe emulsions of oil and water with finite droplet concentration. We use droplets of radius $a$ in a Wigner-cell with radius $R$. Thus, the droplet volume fraction is $x \equiv (a/R)^3$. Thus, the ratio of oil : water in an OW emulsion is given by $x : 1-x$ and $1-x : x$ in a WO emulsion. In the upcoming paragraphs our investigation will centre around a specific system configuration, as given in table 6.1, from which we will only deviate when varying one or more of the system parameters or out of numerical necessity. This configuration has been chosen as it is in reasonable agreement with the experimental parameters given in Ref. [3].

**Table 6.1:** Standard System Parameters

| Quantity | Symbol | Value |
|---|---|---|
| Wigner-Seitz Cell Radius | $R$ | 10.0 $\mu$m |
| Droplet Radius | $a$ | 1.0 $\mu$m |
| Bulk Salt Density Water | $\rho_w$ | 1.0 mM |
| Relative Dielectric Constant Oil | $\epsilon_o$ | 5.0 |
| Positive Ion Size | $a_+$ | 3.6 Å |
| Negative Ion Size | $a_-$ | 3.0 Å |
| Positive Shell Size | $s_+$ | 0.0, 3.6 Å |
| Negative Shell Size | $s_-$ | 0.0, 3.0 Å |

Using these experimental parameters as a guideline will examine not only how the system's quantities change w.r.t. those found in infinitely dilute emulsion, but also answer many of the questions left unanswered in the previous chapter. We will for instance determine the origin of the droplet charge and the surface energy and how the introduction of a finite $s_\pm$ influences the system. We will adhere to a division into two parts, one describing charge and crystallisation, another describing the surface tension.

## 6.2 Surface Charge and Plasma-Parameter

### 6.2.1 Preferential Partitioning

Thus far, we have discussed physical quantities which are calculated by determining and manipulating the electrostatic potential, however, we have yet to see the actual functional form of this potential. In fig. 6.1 we have indicated the equilibrium electrostatic potential $\bar{\phi}(r)$, in the figure referred to as $\phi$, for OW and WO systems. Note that we indeed have $\bar{\phi}'(0) = \bar{\phi}'(R) = 0$ for all the emulsions considered in this figure. Furthermore, we find that in the left-hand graph $\phi(R) = 37.5$ mV for the $R = \infty$ system. This corresponds to $(f_+ - f_-)/2$, which is what one would expect since the modified electrostatic potential $\psi(R) = 0$ for $R = \infty$. In fact, for planar WO emulsions we always have $\bar{\phi}(-\infty) = 0$ and $\bar{\phi}(\infty) = (f_+ - f_-)/2$ and for OW emulsions $\bar{\phi}(-\infty) = (f_+ - f_-)/2$ and $\bar{\phi}(\infty) = 0$. It is clear that this no longer holds for systems in the spherical geometry. We see that $\bar{\phi}(R) < (f_+ - f_-)/2$ for $R \neq \infty$ in the left-hand graph of fig. 6.1. It is also true that $\bar{\phi}(0) > 0$, although this cannot be seen on the scale of this plot.

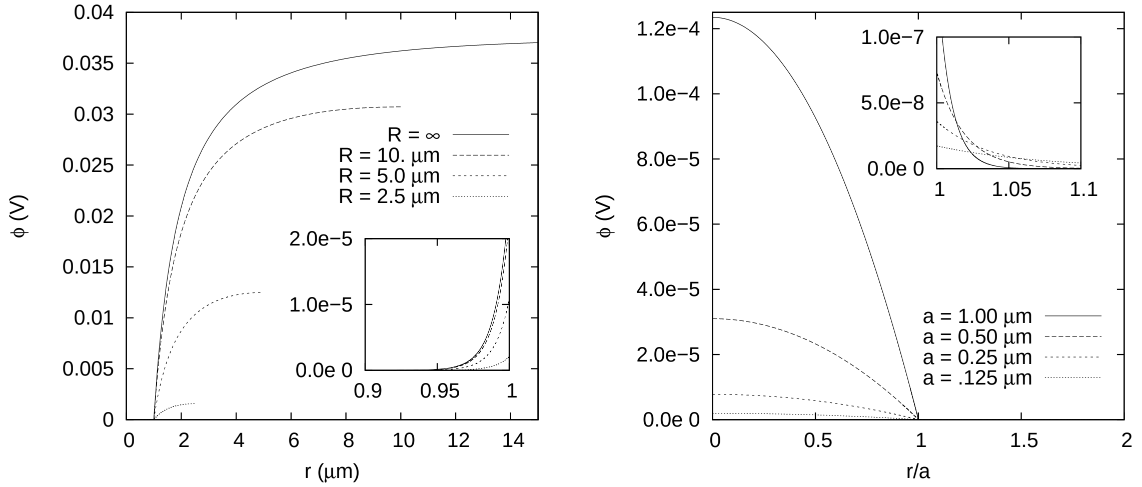

**Figure 6.1:** The electrostatic potential $\phi$ in Volts as a function of $r$ between 0 and $R$ for a WO emulsion, with $a = 1.0$ $\mu$m, (left) and as a function of $r/a$ for an OW emulsion (right). The insets show a small part of the water area close to the interface. The other system parameters are given in table 6.1. For the OW emulsion we have chosen an infinite Wigner-cell, because the Debye-length of water is so small that finite size effects would hardly be noticeable for all but the smallest $R - a$. The choice for $r/a$ dependence on the right is to ensure that the interfaces are all located at $r/a = 1$ in order to facilitate comparison. Both graphs give the electrostatic potential for the $s_\pm = 0$ system, the $s_\pm = a_\pm$ potential looks identical on this scale and only differs by a minute amount in an area of size $\max(s_\pm)$ around $r = a$.

The non-zero modified electrostatic potential at the boundaries is a consequence of the requirement that the Wigner-cell is charge neutral, i.e. $\bar{\phi}'(0) = \bar{\phi}'(R) = 0$, but $\psi(0) \neq 0 \neq \psi(R)$. This is caused by the double-layer modification we mentioned in the previous chapter, which is more extreme in finite Wigner-cells. Due to the small screening length in water the potential decays rapidly enough to assume $\bar{\phi}(0) \approx 0$. However, for the oil side we have that Debye length is close to or larger than $R - a$ in the left graph, or $a$ in the right. Therefore, the system 'chooses' a potential value smaller than $(f_+ - f_-)/2$ in order to achieve charge neutrality within the limited decay length. This limited decay length explains the behaviour asymmetry and the difference in the range of applicability of the polynomial expansion between OW and WO systems observed in the previous chapter. For a WO emulsion with an infinite Wigner-cell the system compensates only for the small effect of the finite water area. For an OW emulsion the effects of finite size droplets become apparent much more quickly, because of the difference between $\kappa_o^{-1}$ and $\kappa_w^{-1}$. Note for instance the difference between the value of $\bar{\phi}(\infty)$ in the left graph of fig. 6.1 and $\bar{\phi}(0)$ for $a = 1.0$ $\mu$m in the right graph. In a planar system both of these values would be equal to $(f_+ - f_-)/2$, because in a planar system there is ample decay on both sides of the interface. Moreover, we find that when $\kappa_o$ approaches $\kappa_w$ this behaviour asymmetry in the spherical geometry vanishes, as we have observed in the previous chapter.

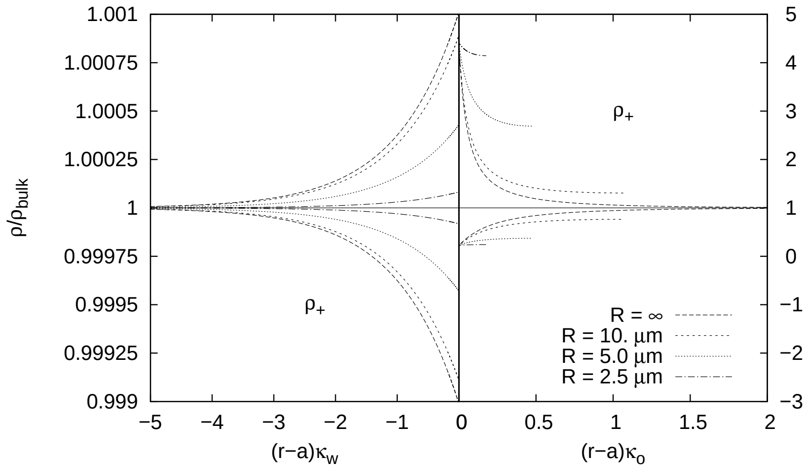

**Figure 6.2:** The ion distributions for the WO emulsions of fig. 6.1 (left) as a function of $(r - a)\kappa$. The upper-left and lower-right quadrants correspond to $\rho_-(r)$ distribution, whereas the lower-left and upper-right correspond to the $\rho_+(r)$ distribution. The effects of preferential partitioning become most strongly evident on the oil side of the interface, where there is a far greater positive ion concentration. To give an indication of the values; $\kappa_w^{-1} = 9.63$ nm, $\kappa_o^{-1} = 8.44$ $\mu$m, $\rho_{\text{bulk},w} = 1.0$ mM, $\rho_{\text{bulk},o} = 8.15 \cdot 10^{-8}$ mM, $f_+ = 14.84$ and $f_- = 17.81$. Note that on both sides the $R = \infty$ ion distributions decays to the bulk density within a couple of screening lengths. We have opted for this particular form of representation, as it illustrates the various effects at work, without the need to use several figures.

Using the electrostatic potentials we have obtained in fig. 6.1 it is possible to determine the corresponding ion distributions in a WO system, see fig. 6.2, and in an OW system, see fig. 6.3. As mentioned earlier, the ion distributions do not decay to their bulk value in a finite Wigner-cell. The droplet and medium charge are given by integrating the area between the positive and negative ion distribution, after appropriate rescaling. Because of the way the data has been represented, it is difficult to see that these areas are in fact equal in size, although the integrands have opposite sign as imposed by charge neutrality. In addition we find that for smaller cells the charge decreases, as can be seen form the water side of fig. 6.2. From the oil side it becomes clear that the medium has a positive charge and hence the droplet must have a negative charge. This is caused by the preferential partitioning of ions. For the OW emulsions of fig. 6.3 it is the droplet which has a positive charge. Note that for small droplets the surface charge scales with $a$. We will come back to this later.

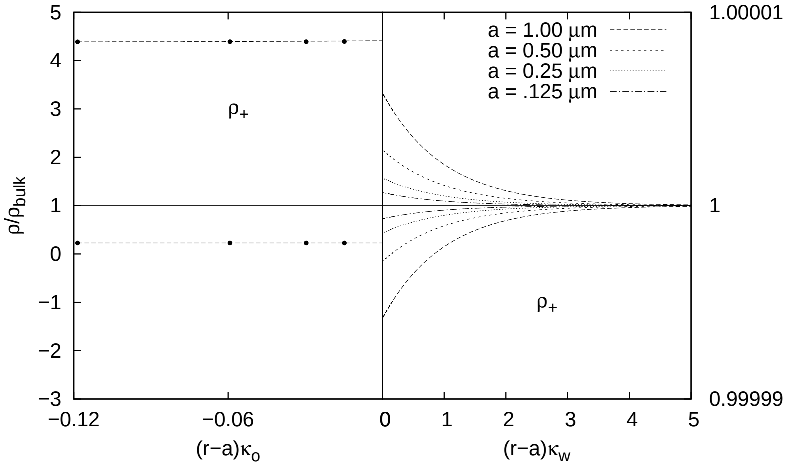

**Figure 6.3:** The ion distributions corresponding the OW emulsions of 6.1 (right) as a function of $(r-a)\kappa$. The dots indicate the termination points of the various distributions in the oil area, from right to left $a = 0.125$, 0.25, 0.5 and 1.0 $\mu$m. On this scale the density profiles for the different droplet radii all overlap in oil area. That is to say, the decay in $\rho_o$ is negligible because of the large screening length compared to the relatively small droplet sizes. The bulk values are the same as in fig. 6.2. Note that the droplet has a positive charge, which at these sizes scales with $a^3$, since the surface charge scales with $a$, as can be seen from the graph.

### 6.2.2 Crystallisation Criteria in the Planar Limit

#### Approach

In this section we will discuss meta-stable crystals of water droplets in oil using the plasma-parameter condition $\Gamma = 106$, as described in Refs. [5, 9, 10]. First, we will refresh the theoretical background given earlier, and rewrite the generic equations given there to the specific case of an WO emulsion considered here. Next, we will examine the validity of the $\Gamma$-model, which is based on a point-like Yukawa droplet-droplet interaction for crystallisation, whereas the full DLVO interaction includes non-Yukawa terms. For the systems we consider in this thesis the non-Yukawa terms will not contribute significantly and therefore we are safe to use the plasma-parameter crystallisation criterion. Using this criterion we will investigate which part of parameter space allows crystallisation to occur in the planar approximation. Finally we will touch upon the difference between this area of parameter space in the spherical geometry w.r.t. the planar geometry.

#### Theoretical Refresher

Recall that the criterium for a system of point-like particles interacting with a Yukawa potential $U(r)$ to crystalise is $\Gamma > 106$, where $\Gamma$, as in Eq. (4.8), is given by

$$\Gamma \equiv \beta U(R)\left(1+\kappa_2 R+\frac{1}{2}(\kappa_2 R)^2\right),$$

where $\kappa_2^{-1}$ is the screening length of the medium and $R$ the typical particle-particle neighbour distance, with Eq. (4.7)

$$\beta U(r) = \frac{\lambda_B Z_1^2}{\epsilon_2}\left(\frac{\exp(\kappa_2 a)}{1+\kappa_2 a}\right)^2 \frac{\exp(-\kappa_2 r)}{r},$$

which is the electrostatic contribution to the DLVO potential. By combining the two for a WO emulsion with water droplets of radius $a$ and charge $Z_w$ in an oil medium, we may write

$$\Gamma = \frac{\lambda_B Z_w^2}{\epsilon_o}\left(\frac{\exp(\kappa_o a)}{1+\kappa_o a}\right)^2 \frac{\exp(-\kappa_o R)}{R}\left(1+\kappa_o R+\frac{1}{2}(\kappa_o R)^2\right). \tag{6.1}$$

The form of Eq. (6.1) implies that the only difference between the value for $\Gamma$ in the planar and spherical geometry is the value of the charge, i.e. $Z_w(a) = 4\pi a^2 \sigma_w(\infty)$ versus $Z_w(a) = 4\pi a^2 \sigma_w(a)$. This fact will prove significant in the following section.

### Point-like Yukawa Potential

In the above formula, we have taken only the electrostatic part of the DLVO potential into account, i.e. $U(r)$ in Eq. (6.1), which is indeed a point-like Yukawa potential. However, actual droplets of water in oil also experience of Van-der-Waals interactions, especially when they are in close proximity to each other. The Van-der-Waals part of the DLVO potential is not of the Yukawa form. This may pose a problem if we wish to apply the theory of Ref. [10] to our emulsions. We have thus far ignored such Van-der-Waals interactions and we will show here that we are correct in continuing to do so. The Van-der-Waals contribution to the DLVO potential is given by

$$\begin{aligned} W(r) &= -\frac{A}{6}\left(\frac{2a^2}{r^2-4a^2}+\frac{2a^2}{r^2}+\log\left(\frac{r^2-4a^2}{r^2}\right)\right), \\ &\approx \begin{cases} -\frac{A}{12}\frac{a}{r-2a} & \text{if } r \approx 2a; \\ -\frac{16}{9}A\left(\frac{a}{r}\right)^6 & \text{if } r \gg 2a, \end{cases} \end{aligned}$$

see [15]. Here $A$ is the Hamaker constant and $r$ is the distance between the centres-of-mass of the two droplets, both of which have radius $a$. For water droplets in oil the Hamaker constant is typically around 0.75 $k_B T$. Note that we can distinguish two different regimes for the Van-der-Waals attraction using a Taylor series. Close range, i.e. $r \approx 2a$, interaction and long range, $r \gg 2a$, which shows the characteristic Van-der-Waals decay rate, $r^{-6}$.

The theory described in Ref. [10] is based on the screened Coulomb potential, which is a point-like Yukawa potential. If adding this Van-der-Waals part to the electric DLVO potential, which is not of the Yukawa form, does not significantly alter the behaviour of the system, we are safe in assuming that we can use the method of Ref. [10] to predict crystallisation. The modified plasma-parameter $\Gamma_{\text{VdW}}$ is now given by

$$\begin{aligned} \Gamma_{\text{VdW}} &\equiv \beta V_{\text{DLVO}}(R)\left(1+\kappa_o R+\frac{1}{2}(\kappa_o R)^2\right) \\ &= \beta(U(R)+W(R))\left(1+\kappa_o R+\frac{1}{2}(\kappa_o R)^2\right) \end{aligned}$$

$$= \left(\frac{\lambda_B Z_w^2}{\epsilon_o}\left(\frac{\exp(\kappa_o a)}{1+\kappa_o a}\right)^2 \frac{\exp(-\kappa_o R)}{R} - \frac{A}{6}\left(\frac{2a^2}{R^2-4a^2} + \frac{2a^2}{R^2} + \log\left(\frac{R^2-4a^2}{R^2}\right)\right)\right) \times \left(1+\kappa_o R + \frac{1}{2}(\kappa_o R)^2\right).$$

To illustrate just how minute the differences between $U(r)$ with corresponding $\Gamma$ and $V_{\mathrm{DLVO}}(r)$ with corresponding $\Gamma_{\mathrm{VdW}}$ are, we have included fig. 6.4, which gives $U(r)$ for a typical system together with $V_{\mathrm{DLVO}}(r)$ for a couple of Hamaker constants, namely $A = 0.0075$, 0.75 and 75 $k_BT$. For the physically relevant Hamaker's constant, $A = 0.75\ k_BT$, the effects of the Van-der-Waals interaction are completely negligible at $r = R$, hence for all intents and purposes $\Gamma = \Gamma_{\mathrm{VdW}}$.

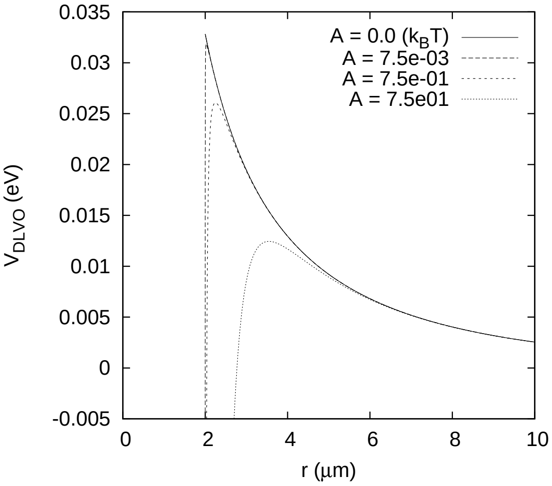

**Figure 6.4:** The full DLVO potential in eV as a function of $r$ for a WO emulsion with $R = 10.0$ $\mu$m, $a = 1.0$ $\mu$m, $x = 0.001$, $\rho_w = 1.0$ mM, $\epsilon_o = 5.0$ and a series of Hamaker constants. Note that the effect of the Van-der-Waals contribution to $V_{\mathrm{DLVO}}$ is negligible at $r = R$ even with $A = 75$ k$_B$T.

### Planar Plasma-Parameter 106-Isolines

We will examine the planar limit crystallisation criterion before returning to the spherical geometry in the next paragraph. From Eq. (6.1) one can see that there are many parameters, $R$, $a$, $\rho_w$, $\epsilon_o$ and $a_\pm$, which influence $\Gamma$ and their effects are not easily predicted. We propose the representation of the data as given in fig. 6.5, which shows planar $\Gamma = 106$ isolines as a function of the ion size and self-energy for several $\rho_w$. For $R = 10.0$ $\mu$m, $a = 1.0$ $\mu$m and $\epsilon_o$, we determine the $\Gamma = 106$ isolines by varying $a_\pm$ and $\rho_w$. The convex envelope of this data indicates the maximum area in parameter space where theory predicts crystallisation can occur. That is to say, in this area we can find $a_+$, $a_-$ and $\rho_w$ such that $\Gamma > 106$. This will prove to be an important tool to rule out crystallisation for certain ion size ratios, droplet volume fractions $x$ etc. We have multiplied $a_\pm$ with $\epsilon_o$ to facilitate comparison of the convex envelopes for different $\epsilon_o$ in fig. 6.6 (left).

See Appendix A, fig. A.1, for the $\rho_w$ isolines corresponding to the $x = 0.1$, $\epsilon_o = 5$ envelope in fig. 6.6. The convex envelopes for $R = 5.0$ $\mu$m and $R = 15.0$ $\mu$m have been indicated in fig.

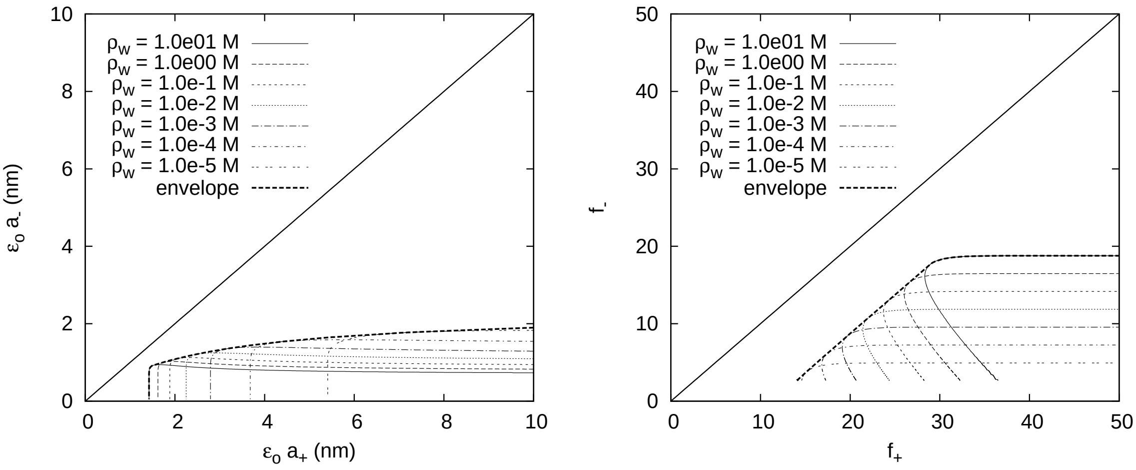

**Figure 6.5:** The planar $\Gamma = 106$ isolines for $R = 10.0$ $\mu$m, $x = 0.001$ and $\epsilon_o = 5$ as a function of $a_\pm$ and $\rho_w$ (left), and as a function of the self-energy differences, $f_\pm$, corresponding to $a_\pm$ (right). Crystallisation can occur in the area underneath each curve (left), enclosed by each curve and $f_+$-axis (right). Because of $a_+ - a_-$ mirror symmetry, we have only included one branch of the isolines. Note that we have also given the convex envelope of the isolines for $10^{-7} < \rho_w < 10$ M. This envelope indicates the maximum crystallisation area, i.e. for any point underneath this curve there there are system parameters $a_+$, $a_-$ and $\rho_w$, such that $\Gamma > 106$.

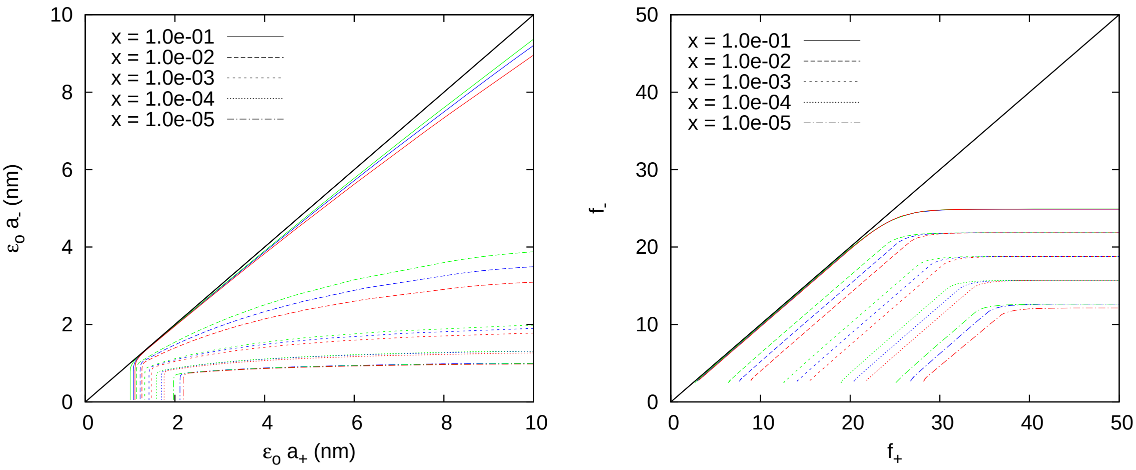

**Figure 6.6:** The convex envelopes of the $\Gamma = 106$ lines for $R = 10.0$ $\mu$m, $10^{-7} < \rho_w < 10$ M, $\epsilon_o = 2.5$ (red), $\epsilon_o = 5$ (blue) and $\epsilon_o = 10$ (green) in the planar geometry. The envelopes are given as a function of $\epsilon_o a_\pm$ (left) to facilitate comparison of curves for different values of $\epsilon_o$.

A.2. Let us now analyse the data of fig. 6.5 and 6.6. It is clear that planar theory predicts crystallisation for $a_-/a_+ \approx 1$ only at high values of $x$. This one of the reasons why we are not interested in such ion-size ratios, as was mentioned in the previous chapter. The droplet volume fraction which most closely corresponds to the experiments of Ref. [3] is $x = 0.001$. We can see that for this fraction only a narrow strip of ion size fractions exists which allows the droplets to achieve crystallisation. This is especially true for high bulk salt concentrations as can be seen form fig. 6.5 (left). For $\rho_w = 10$ M and $\epsilon_o = 5$, we require $a_- \in [0.0, 2.0]$ Å with $a_+ > 3.0$ Å, whereas for $\rho_w = 1.0$ mM, we require $a_- \in [0.0, 3.0]$ Å with $a_+ > 7.5$ Å.

From fig. 6.6 it becomes clear that there is no crystallisation at $x = 0.001$ for the ion size-ratio of $5/6 \approx 0.83$, or equivalently 6/5, we have considered in this thesis thus far. In fact, the ion size-ratio for $H^+$ and $Br^-$ for the experiments of Ref. [3] is even worse, namely $a_+/a_- = 2.8/3.0 \approx 0.93$. There is a good indication that there are ion sizes, within the range available to experimentalists, for which we would find crystallisation. However, it should be noted that we have approximated the self-energy of the ions by making use of the Born formula. Therefore, we have included the self-energy differences corresponding to the ion sizes in the right-hand side of the figures in this section. Since the actual self-energy may differ substantially form that calculated in the Born approximation, the $f_\pm$ representation of the isolines should be more insightful than the $\epsilon_o a_\pm$ representation. The isolines in these graphs correspond to $a_- > a_+$, the horizontal lines for $f_\pm$ come form the line segments orthogonal to the axes in the $a_\pm$-graph, whereas the lines parallel to the $f_+ = f_-$ line come form the curved lines in the $a_\pm$-graph. Naturally we find that we require an ample difference in $f_+$ and $f_-$, especially for low salt concentration to achieve $\Gamma > 106$. From fig. 6.6 we find that crystallisation can only occur when $a_-/a_+ < 0.65$ for $x = 0.001$, or equivalently $f_-/f_+ < 0.65$, at least on the basis of planar charge distributions.

### Plasma-Parameter 106-Isolines in the Spherical Geometry

We have yet to examine the effect of the spherical geometry on the allowed size ratio, since curvature will definitely influence charge of the droplet and hence the behaviour of the isolines and corresponding convex envelope. Fig. 6.7 shows a comparison between the convex envelope for crystallisation in spherical geometry and corresponding envelope in planar geometry.

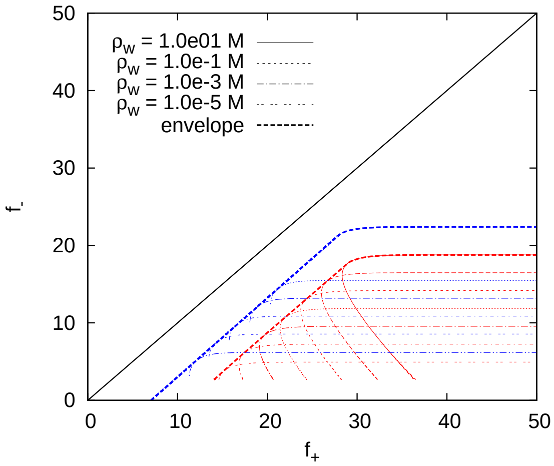

**Figure 6.7:** The convex envelope and corresponding isolines for $R = 10.0$ $\mu$m, $x = 0.001$ and $\epsilon_o = 5$. The spherical results have been indicated in blue and the planar results in red. Note that we have extrapolated the convex envelope in the spherical geometry for $\rho_w > 10$ mM from the available data.

We find that for these systems the effect of the spherical geometry is to raise the isolines w.r.t.

the $f_+$-axis. The difference in the planar and spherical isolines is virtually constant with $\rho_w$, therefore, we can safely extrapolate the convex envelope for higher bulk salt concentrations. We believe that isolines for different $\epsilon_o$ and $x$ will be affected similarly. As a rule of thumb one can state that the spherical geometry will change the isolines and convex envelope for a certain $x$ w.r.t. the isolines and envelope of the planar geometry for the same $x$. The spherical isolines and envelope will correspond to those of a planar $x'$ which differs by a factor of five to ten from the original $x$. From this single graph we cannot assume that spherical geometry always increases the crystallisation zone in this representation. Having said this, we can conclude that for the systems in fig. 6.7 the condition on the size ratio of the ions is relaxed to $a_-/a_+ < 0.75$, which is substantially closer to the ratio of 0.83 used in this thesis, but still quite far from the ratio 0.93 corresponding to the experiments.

Throughout this thesis we have worked with $a_+ = 3.6$ Å and $a_- = 3.0$ Å, which for $\epsilon_o = 5$ translates into $f_+ = 14.8$, $f_- = 17.8$. The closest point where crystallisation is predicted by our plasma-parameter model is $f_+ \approx 12.3$, $f_- \approx 19.2$, with $\rho_w \approx 1.0$ mM. This means that a 20% change in self-energy difference w.r.t. that found by using the Born approximation is sufficient to explain crystallisation in the Na$^+$-Br$^-$ system we have used, or a 25% change for the H$^+$-Br$^-$ self-energies used to model the results in Ref. [3]. It should be noted that this is a 20-25% difference in the desired direction. However, such a self-energy alteration is not unreasonable, since the self-energies here have been estimated using a Born approximation, neglecting other effects. From the above discussion we can conclude that not only does it prove difficult to explain the observed crystallisation, but we also find that crystallisation is not as easily achieved as was previously expected. The difference in self-energy has to be quite significant for physically reasonable systems and finding ion species which accomplish this for a fixed $\epsilon_o$ and $\rho_w$ can be difficult. We believe that this is one of the main reasons why such crystallisation had, to the knowledge of the author, not been observed earlier and was only found recently in Ref. [3].

### 6.2.3 Return to the Spherical Geometry, $x$ and $\epsilon_o$ Dependence

We have yet to examine the effects of the droplet volume fraction, defined as $x \equiv (a/R)^3$. That is keeping an $R$, in this case $R = 10.0$ $\mu$m, fixed and letting $a$ run between 0 and $R$. The choice for $R$ is in part inspired by the experiments described in Ref. [3] and in part out of numerical necessity, i.e. to have smooth numerical convergence. We will find that the behaviour of $\Gamma$ under curvature is not quite so clear-cut as the result in the previous section suggested. Let us begin by examining the behaviour of the physical quantities $Z$ and $\Gamma$ for the system parameters given in table 6.1. The variables are $a$ and $\epsilon_o$. By limitation of the algorithm's numeric stability we must restrict our attention to $\epsilon_o \in [3.0, 8.0]$.

Let us begin by discussing $\Gamma$, plotted in fig. 6.8 as a function of $x$ and $\epsilon_o$. There is tendency for $\Gamma$ to increase for greater values of $x$, only to decrease as $x$ approaches 1. A similar increase-decrease behaviour can be observed for $\epsilon_o$. To understand both trends we need to examine the droplet charges with which $\Gamma$ was determined and the role of $\epsilon_o$ in Eq. (6.1). Fig. 6.10 shows the charge of a water droplet as a function of $x$ and $\epsilon_o$. It is should be clear that the behaviour of $Z$ in the left-hand graph is not the same as predicted by planar theory, since that tells us that $Z = 4\pi a^2 \sigma_p$ and hence $Z \propto x^{2/3}$, which gives a straight line in a log-log plot.

Note that the volume fraction dependence of $\Gamma$ and $Z$ is almost identical. There is a difference

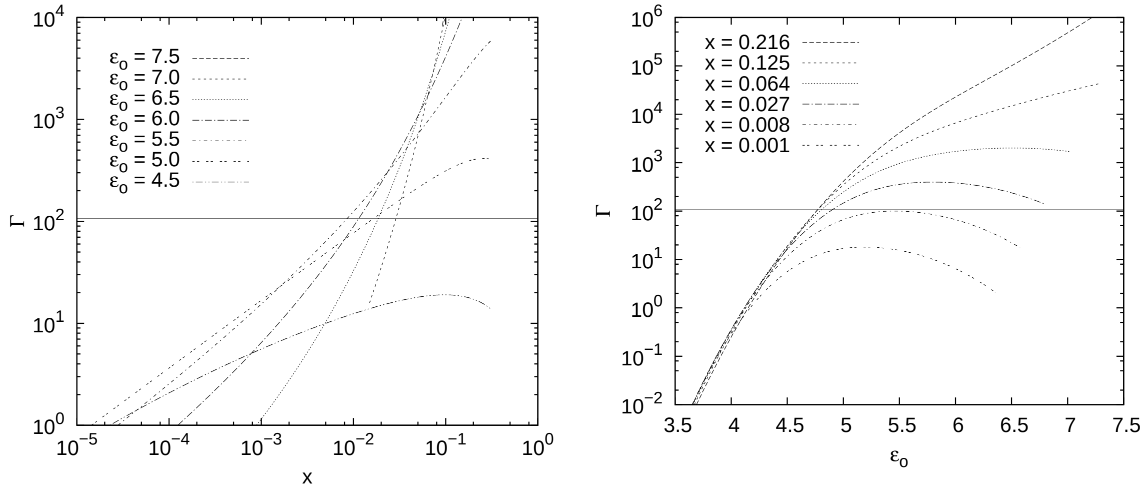

**Figure 6.8:** The plasma-parameter as a function of the droplet volume fraction (left) for several $\epsilon_o$, and as a function of the dielectric constant of oil for several $x$ (right). We have used $\rho_w = 1.0$ mM, $R = 10.0\ \mu$m, $a_+ = 3.6$ Å, $a_- = 3.0$ Å and $s_\pm = 0$. Note the inclusion of the $\Gamma = 106$ line above which crystallisation occurs according to the model presented in Ref. [10].

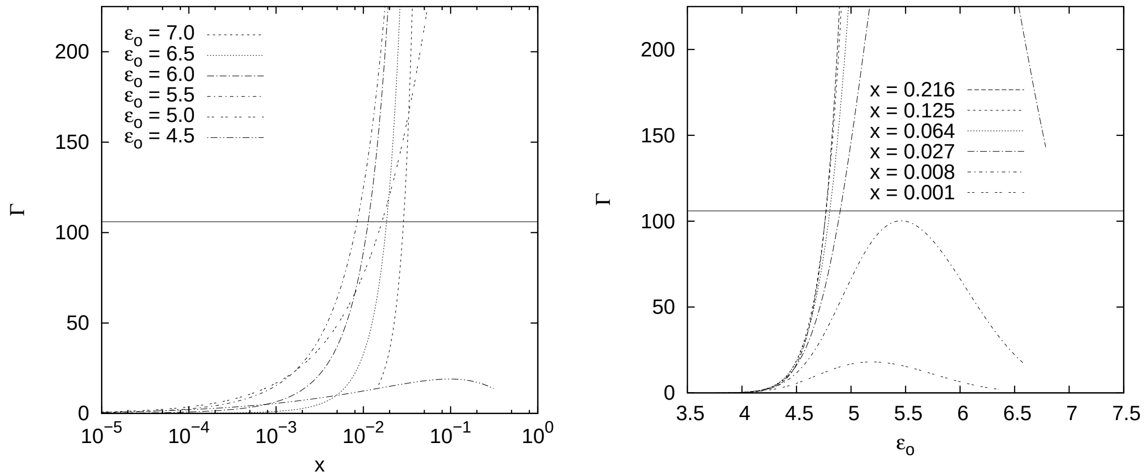

**Figure 6.9:** The plasma-parameter as in fig. 6.8, but now on a linear scale for a better view of the crystallisation zone.

in slope, i.e. the $\Gamma$ lines intersect, whereas the $Z$ lines do not. This can be explained by the fact that $\Gamma \propto Z^2$ and that the $\epsilon_o$ dependence of $\Gamma$ in Eq. (6.1) shifts this $Z^2$ proportionality ever further down for greater $\epsilon_o$. More importantly, this means that that the decrease of $\Gamma$ for $x$ close to 1 can be explained by the corresponding decrease in the charge. We need to realise that for the $x$ dependence of $Z$ there are two effects at work. Firstly, the increase of droplet size from the nm range to the $\mu$m range will make the system more 'planar', hence the charge will increase as we have seen in the previous chapter. However, the second effect is that of a decreased oil area, i.e. $R - a$ becomes smaller, which in section 6.2.1 we have seen decreases the charge. The combined effect will be an increase in charge for small $x$ which peaks at some value determined by $\epsilon_o$ followed by a decrease in $Z$ for larger $x$. For the $\epsilon_o$ dependence of $\Gamma$, as shown

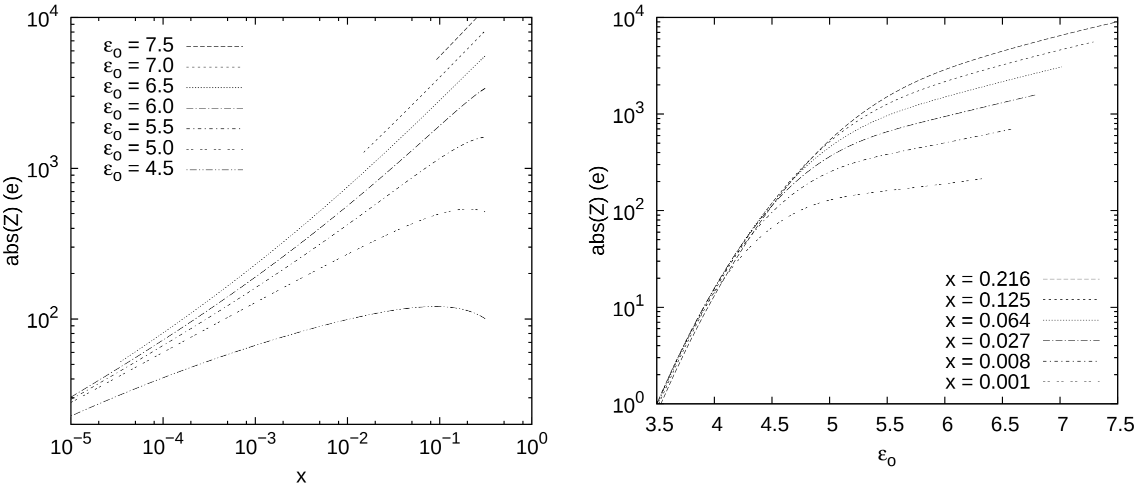

**Figure 6.10:** The absolute value of the droplet charge $Z$ as a function of the water/oil volume fraction $x$ (left) for several $\epsilon_o$ and of the dielectric constant of oil for several $x$ (right). The systems are the same as those of fig. 6.8.

in the left-hand graphs of figures 6.8 and 6.9, we find the following cause for the decrease in the plasma-parameter with large $\epsilon_o$. By increasing $\epsilon_o$ the charge increases as well, see fig. 6.10 (right), hence the reason for the decrease in $\Gamma$ must be sought in the $\epsilon_o$ dependent terms of Eq. (6.1). Using some basic algebra one can easily verify that these terms cause the eventual decrease, because they drop off more quickly than $Z^2$ increases.

We have seen a decrease in the plasma-parameter for large values of the droplet volume fraction. It should be noted that such large $x$, i.e. $x > 0.1$, are physically unrealistic and can therefore be safely ignored. The inter-droplet separation is extremely small, if $x \approx 0.1$ then $R - 2a \approx 0$. Any small influences on the system, which allow two droplets to come into contact, will cause a chain-reaction of coalescence. When one droplet coalesces, the effect will ripple through the emulsion, because the inter-droplet separation is negligible compared to the droplet radius. Thus, even if the plasma-parameter is extremely high for $R$ slightly greater than $2a$, the close packed nature of the system will have inherent instability due to the droplet's ability to coalesce.

Now that we have examined $Z$ and $\Gamma$ in the spherical geometry we would like to compare the $\Gamma$ by solving the full Poisson Equation to that found by solving it in the planar approximation. See fig. 6.11 for a representation of both planar and spherical crystallisation areas in parameter space. It should be pointed out that for $\epsilon_o \in [4.8, 7.5]$ the system will crystallise at much lower volume fractions than predicted by planar theory, above $\epsilon_o = 7.5$ the area is more or less the same. However, for $\epsilon_o < 4.8$, we find that we require higher $x$ for crystallisation to occur. The effect of having a spherical geometry is therefore not quite as clear cut as one might think and as was suggested by the results in the previous section.

### 6.2.4 Plasma-Parameter at Constant Droplet Volume Fraction

In the previous section we examined the quantities for which crystallisation occurs by varying the volume fraction, keeping the typical droplet-droplet distance fixed at $R = 10.0$ $\mu$m. However, from an experimental standpoint it makes more sense to vary the system parameters at

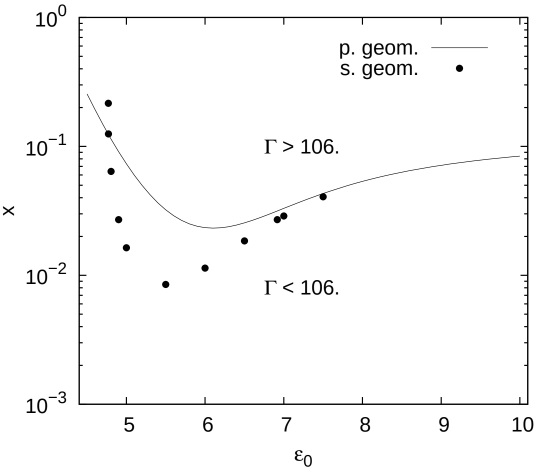

**Figure 6.11:** The $\Gamma = 106$ isoline as a function of $\epsilon_o$ and $x$, for $\rho_w = 1.0$ mM, $a_+ = 3.6$ Å and $a_- = 3.0$ Å. The solid line indicates the isoline we have determined by using the planar limit, whereas the dots indicate the data points we have obtained using the spherical geometry, see fig. 6.8. Note the sizeable increase in the zone where crystallisation can occur for $\epsilon_o \in [4.8, 7.5]$.

constant volume fraction. That is to say, volume fraction is imposed on the system by emulsifying a certain amount of oil with water, whereas the cell and droplet sizes are determined by the physics of the system. In this and the next section we will examine the dependence of $\Gamma$ and $Z$ on $R$, $\rho_w$, $\epsilon_o$, $a_\pm$ and $s_\pm$, keeping the composition $x$ fixed. Since we have already looked at $\epsilon_o$ in the last section, we will confine ourselves to $\epsilon_o = 4$, 5 and 6 here. Because of the vastness of the parameter space we have made choices to restrict our attention to certain zones within it. These choices were inspired by the systems ability to crystallise, the stability of the algorithm and the available time. It is our intention to establish a set of qualitative remarks about the the various quantities and their difference w.r.t. the planar limit.

Let us begin by examining the plasma-parameter, $\Gamma$, see figures 6.12 (left) and 6.13, where $\Gamma$ is plotted as a function of $R$ for various values of $\epsilon_o$ and $x$. One can see is that crystallisation occurs only for larger volume fractions and in a narrow $R$-band. This is consistent with our findings based on fig. 6.11. The effect of increased $R$ is to increase the charge of the droplet, since the system becomes more planar. Hence, it is the explicit $R$ dependence in the charge independent terms of Eq. (6.1) which cause the decrease in $\Gamma$ for larger $R$. This can be easily seen from the fact that those charge independent terms are dominated by $\exp(-\kappa_o R)$ for large $R$. A more interesting phenomena becomes apparent when we consider the right-hand side of fig. 6.12 (right). Here we can see that the curvature does indeed increase $\Gamma$ w.r.t. the planar value, however, the slopes of the spherical and planar lines are different for small $R$. This would suggest that there may be a cross-over point at low $R$ where the spherical geometry reduces $\Gamma$. For clarity reasons we have not included this point in the graph.

Fig. 6.14 shows the droplet charge for $x = 0.001$ and several $\epsilon_o$ as a function of $R$. We compare the planar with the spherical prediction and find that there is indeed a cross-over in the charge, which accounts for a similar cross-over phenomena occurring in the plasma-parameter. For large $R$ we see that the system tends to the $Z = \mathcal{O}(R^2)$ that is predicted by planar theory.

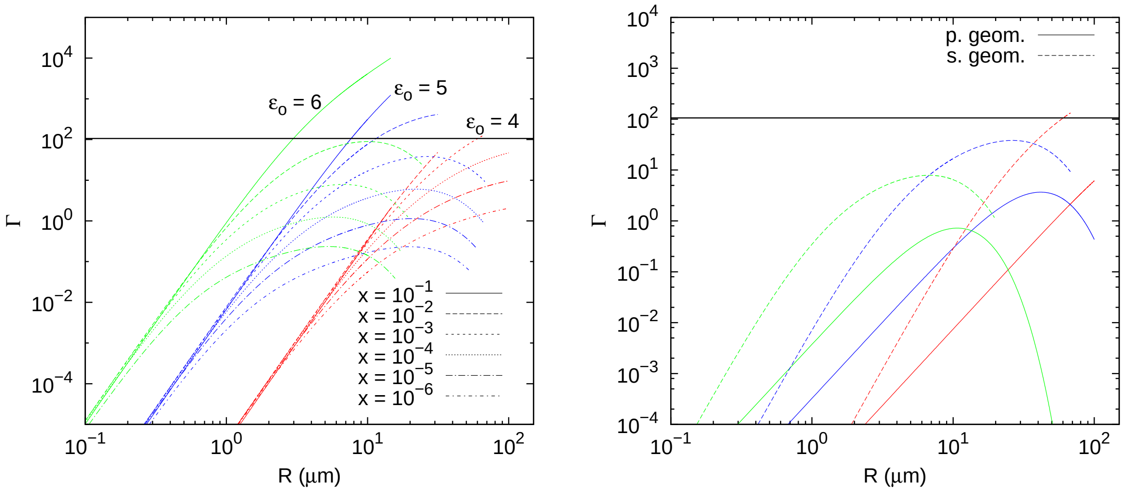

**Figure 6.12:** The plasma-parameter, Γ, as a function of the Wigner-radius, $R$, for several water-volume fractions $x$ and $\epsilon_0$ (left). The red lines are $\epsilon_o = 4$, the blue lines are $\epsilon_o = 5$ and the green lines are $\epsilon_o = 6$. The difference between the planar geometry and the spherical geometry for $x = 10^{-3}$ (right), the spherical curves correspond to the ones in the left figure.

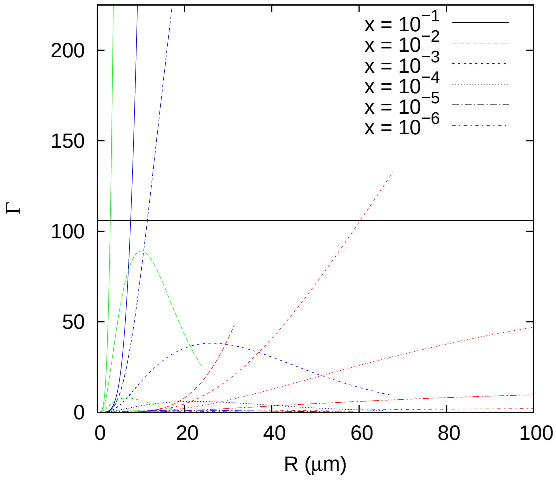

**Figure 6.13:** The plasma-parameter, Γ, as in fig. 6.12 (left) but now represented linearly for better view of the crystallisation area and the effect of volume fraction.

Although, this should be intuitively clear, larger $R$ need to be considered before we can prove this statement. From the fact that for small $R$, $Z$ has a different slope in a log-log plot than its corresponding planar charge, we may conclude that $\sigma \propto R^k$. Here $k$ is the difference in the slope of the spherical and planar curves, which we can easily determine because both sets of lines are linear in this regime. We find that $Z_{\rm sp} \propto R^3$ and hence $\sigma \propto R$. This behaviour can be most easily explained using Eq. (4.5). Let us repeat it here for the $s_\pm = 0$ system in a WO emulsion

$$\sigma_w \quad = \quad -\frac{2}{a^2}\rho_w \int_0^a \mathrm{d}r \; r^2 \sinh(\psi(r)).$$

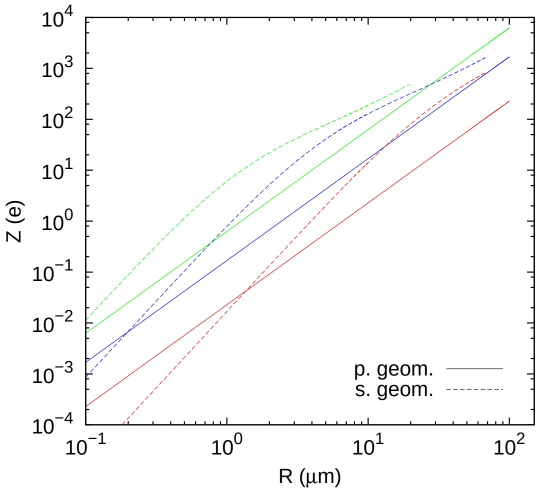

**Figure 6.14:** The charge corresponding to the lines in fig. 6.12 as a function of $R$, with $x = 10^{-3}$. Note the cross-over between increased and decreased charge w.r.t. the planar geometry.

We know that for small droplets $\psi(r) \approx c \neq 0$ in the water area. Therefore we may write

$$\begin{aligned}\sigma_w &\approx -\frac{2}{a}\tilde{c}\int_0^a \mathrm{d}r\ r^2 \\ &= -\frac{2}{3}\tilde{c}a,\end{aligned}$$

with $\tilde{c} = \rho_w \sinh(c) \approx \rho_w c$. Since we are working at constant volume fraction $a \propto R$ and hence $\sigma \propto R$. This this is one of the 'small size' effects which also becomes visible for extremely small droplets in infinite cells. The location of the transition to linear scaling with $R$ differs with $\epsilon_o$, since the approximation $\psi(r) \approx c$ is dependent on the screening length.

### 6.2.5 Ion Density and Ion Size Effects on Crystallisation

In the previous section we have seen that the behaviour of the various parameters as a function of $R$ can lead to a substantial increase in the plasma-parameter in certain regimes and a substantial decrease in others. Also, the need to calculate quantities in the spherical geometry, rather than in the planar, has been re-emphasised. In this section we will investigate the effects of the bulk salt concentration in water and the ion size on crystallisation. In fig. 6.15 we have indicated the plasma-parameter as a function of $\rho_w$ for $R = 10.0$ $\mu$m and a series of $x$ and $\epsilon_o$.

Note that $\Gamma$ has a maximum for some bulk water density. This maximum can be explained as follows. The charge from which $\Gamma$ was determined, see fig. 6.16, appears to level off to a constant value with increasing $\rho_w$. The constant charge limit with increasing $\rho_w$ for the spherical geometry is caused by charge saturation of the droplet. This is in stark contrast with the behaviour of $Z$ in the planar calculation, for which it was found that $Z \propto \sqrt{\rho_w}$, as can be easily deduced from Eq. (4.5). Therefore the planar limit results does not allow for such a charge saturation. Since the charge becomes more or less constant, we must conclude that the decay in $\Gamma$ seen for high $\rho_w$ is caused by the charge independent terms in Eq. (6.1). Since $\kappa_o$ is

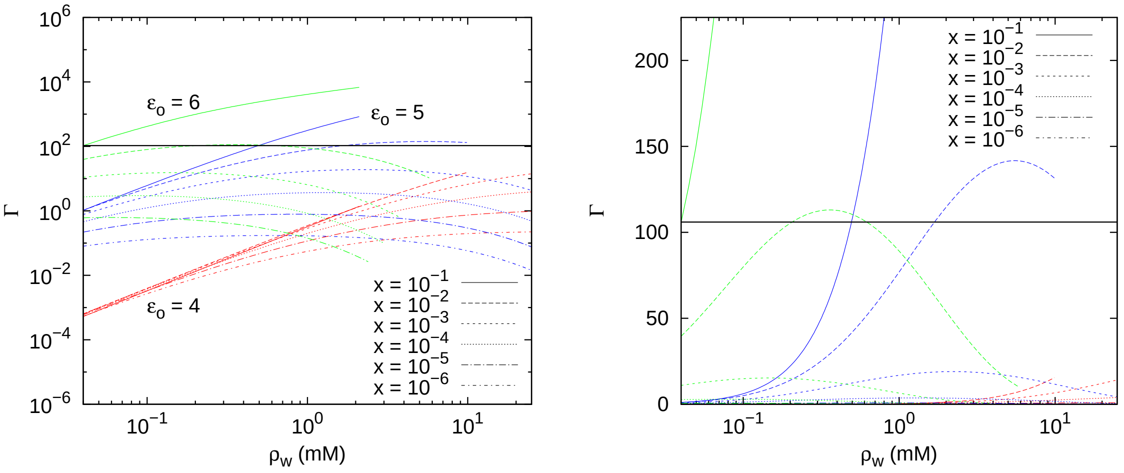

**Figure 6.15:** Γ as a function of the bulk ion concentration in water, for $R = 10.0$ $\mu$m and other system parameters corresponding to those in fig. 6.12 (left). In the right-hand graph we have the linear version for better view of the crystallisation area.

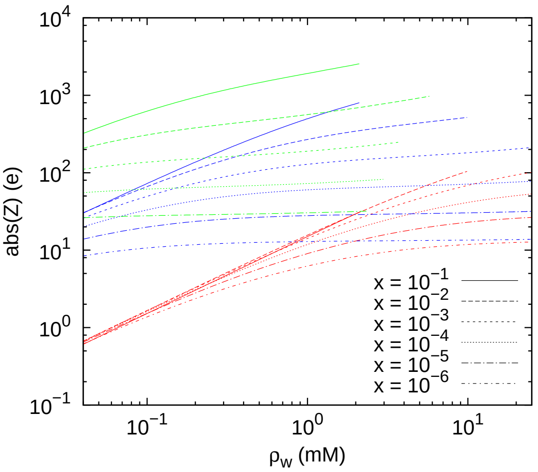

**Figure 6.16:** The charge dependence on the bulk ion density in water, $\rho_w$, corresponding to fig. 6.15 (left).

proportional to $\sqrt{\rho_w}$ and Γ is dominated by $\exp(-\kappa_o(R-2a))$, we see that for $x < 1/8 = 0.125$ there will always be a decrease in the plasma-parameter at high salt concentrations. The consequence of having a maximum in Γ as a function of $\rho_w$ is that crystallisation can only occur in a narrow $\rho_w$-strip, and only for high droplet volume fractions, as can be seen in fig. 6.15.

Now that we have determined that changing the salt concentration can both increase and decrease the plasma-parameter, let us turn our attention to the ratio and size of the ions. Note that we have ignored the shell-parameter here, since it does not notably modify to the charge with respect to that found for the step self-energy potential. See fig. 6.17 for the effect of the $a_-/a_+$ ratio on Γ in the spherical geometry (left) compared to the effect in the planar geometry (right). Fig. 6.18 shows the Γ dependence on the ion size with a similar comparison. We have taken $R = 1.0\ \mu$m here for numerical convenience, whereas $R = 10\ \mu$m would have been a more suitable choice for the sake of experimental comparison.

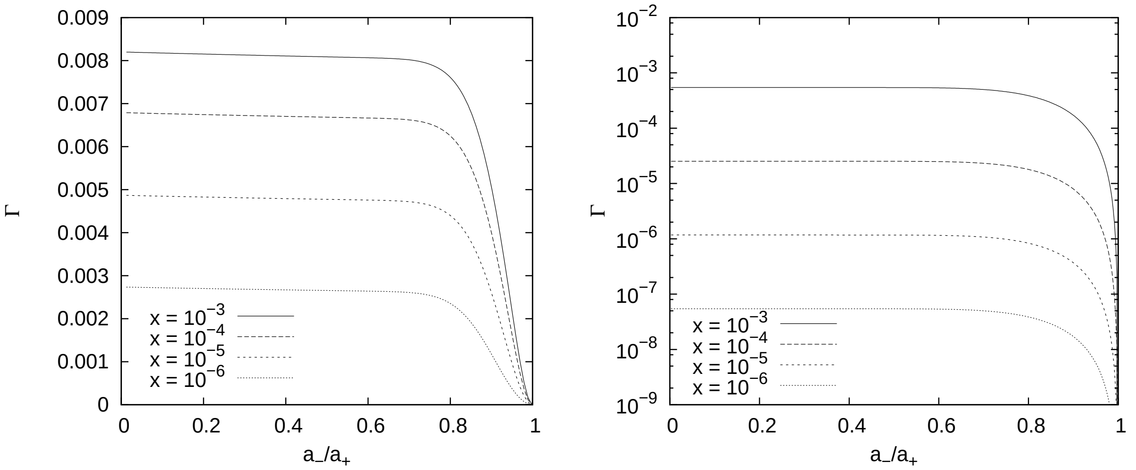

**Figure 6.17:** The plasma-parameter as a function of the ratio $a_-/a_+$ for a series of $x$ in the spherical geometry (left) and the corresponding planar values (right). The system parameters are given by $\rho_w = 1.0$ mM, $\epsilon_o = 5$ and $R = 1.0\ \mu$m. Note the tremendous difference between the value of Γ in the planar and in the spherical geometry.

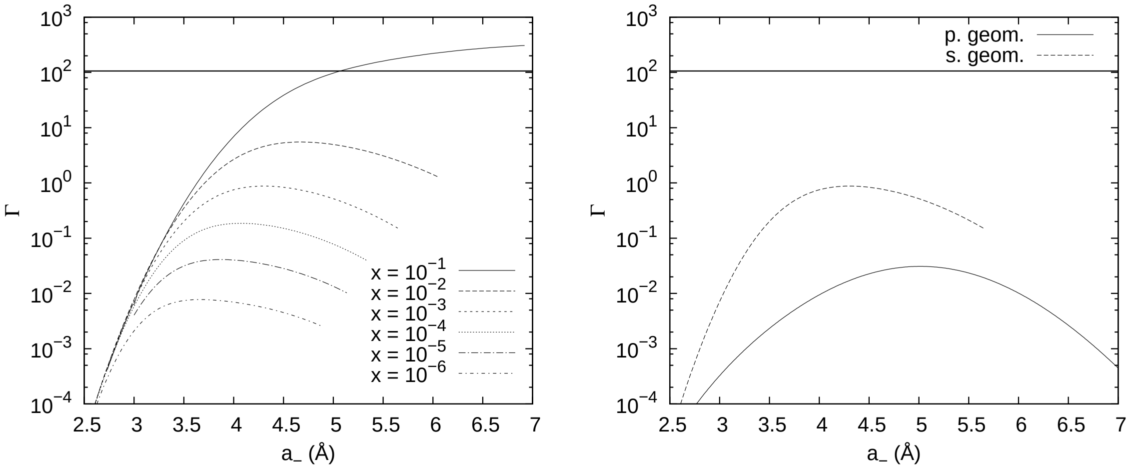

**Figure 6.18:** Γ as a function of $a_-$ for a fixed ratio $a_-/a_+ = 5/6$ and a series of $x$ in the spherical geometry (left) and the corresponding planar values (right). The system parameters are the same as in fig. 6.17. Again we have an enourmous difference between the value of Γ in the planar and in the spherical geometry.

In fig. 6.17 we see that there is a substantial size ratio range over which the plasma-parameter hardly changes. That is to say, if we fix the size of the largest ion and reduce the size of the smallest, there will not be a noticeable difference in Γ for $a_+/a_- \in [0.0, 0.7]$. We should also point out that for $a_-/a_+ \to 1$ there is no self-energy difference. Hence, there is no preferential partitioning and no charge. This is illustrated by the decrease of the plasma-parameter to 0 in fig. 6.17. This is the second reason why we are not interested in $a_+/a_- \approx 1$, as was mentioned in the previous chapter. In fact in this $a_+/a_- \to 1$ limit all physical quantities vanish. Since modifying the ion sizes directly and indirectly influences a whole host of parameters, we cannot make conclusive statements about physics underlying the behaviour observed in figures 6.17 and 6.18. For now, the effect of increasing the size of the ions on the plasma-parameter must be determined on a system-to-system basis.

## 6.3 Surface Tension

### 6.3.1 Antiderivative of the Electrostatic Excess Stress

In this part we will determine the differences between the surface tension in finite and infinite Wigner-cells. This analysis is based on the study of the surface charge in section 6.2. For the systems considered in this section we also calculated the surface tension. However, we felt it was inappropriate to convolute the discussion of $\Gamma$ and $Z$, which are strongly related, by mixing in the surface tension results. In this section we will focus on the origin of $\gamma$, i.e. whether the water or the oil contributes the most to its value and what the effect of a shell-parameter is. In order to facilitate the analysis we can rewrite Eq. (4.4) as

$$\begin{aligned}
\beta\gamma &= -\frac{1}{a^2}\sum_{i=\pm}\int_0^R \mathrm{d}r\ r^2\left(\rho_i(r) - \rho_{\mathrm{bulk}}(r) + \frac{1}{2}q_i\rho_i(r)\bar{\phi}(r)\right) \\
&\equiv \int_0^R \mathrm{d}r\ \tau(r) \Rightarrow \\
\tau(r) &= -\frac{1}{a^2}\sum_{i=\pm} r^2\left(\rho_i(r) - \rho_{\mathrm{bulk}}(r) + \frac{1}{2}q_i\rho_i(r)\bar{\phi}(r)\right).
\end{aligned}$$

The ionic stress, or pressure, $\beta^{-1}\tau(r)$, is caused by the preferential partitioning of positive and negative ions. Note that it has dimension $\mathrm{Nm}^{-2}$. We now consider the antiderivative of this stress term, i.e.

$$\gamma(r) = \beta^{-1}\int_0^r \mathrm{d}r'\tau(r'), \tag{6.2}$$

with $\gamma = \gamma(R)$ by definition. By examining Eq. (6.2) for several systems we can get a good indication of the areas within the Wigner-cell which contribute most to the integrand and the way in which they contribute. See figures 6.19 and 6.20 for $\gamma(r)$ corresponding to electrostatic potentials of fig. 6.1 in section 6.2.1.

There are two things which become immediately clear from figures 6.19 and 6.20. One is the striking difference between the behaviour of the antiderivative of the stress for step and weighted self-energy potentials. The second is the difference between the contribution of the oil area and that of the water area to the excess surface tension. We see that the oil area for the step self-energy potential contributes most to the value of $\gamma$. This can be easily explained by the following. When we consider Eq. (4.4) there are two terms we need to integrate, i.e. $\rho_i(r) - \rho_{\mathrm{bulk}}(r)$ and $\rho_i(r)\bar{\phi}(r)$. Both terms essentially vanish in the water area more than a few $\kappa_w^{-1}$ from the interface, because $\rho_i(r) \approx \rho_{\mathrm{bulk}}(r)$ and $\bar{\phi}(r) \approx 0$ there. Even close to the interface, the difference between $\rho_i(r)$ and $\rho_{\mathrm{bulk}}(r)$ and $\bar{\phi}(r)$ and 0 respectively is negligible for this system

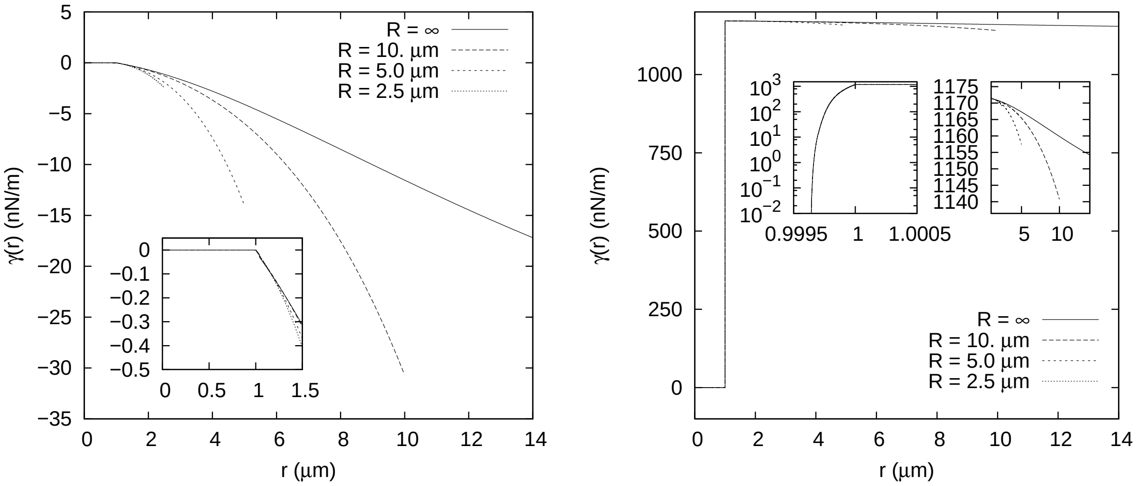

**Figure 6.19:** The antiderivative of the stress $\beta^{-1}\tau(r)$, $\gamma(r)$, as a function of $r$ corresponding to the electrostatic potential of the WO emulsions in the left-hand graph of fig. 6.1 for $s_{\pm} = 0$ (left) and $s_{\pm} = a_{\pm}$ (right). The inset in the left-hand graph shows that there are no anomalies around the interface. This can be compared to the graph on the right, where we see that the largest contribution to the surface tension comes from the vicinity of the interface. In fact, from the left insert we see that it comes from the water area. In the oil area $\gamma(r)$ behaves as in the left-hand graph, see the right insert. We indeed find that $\gamma = \gamma(R)$.

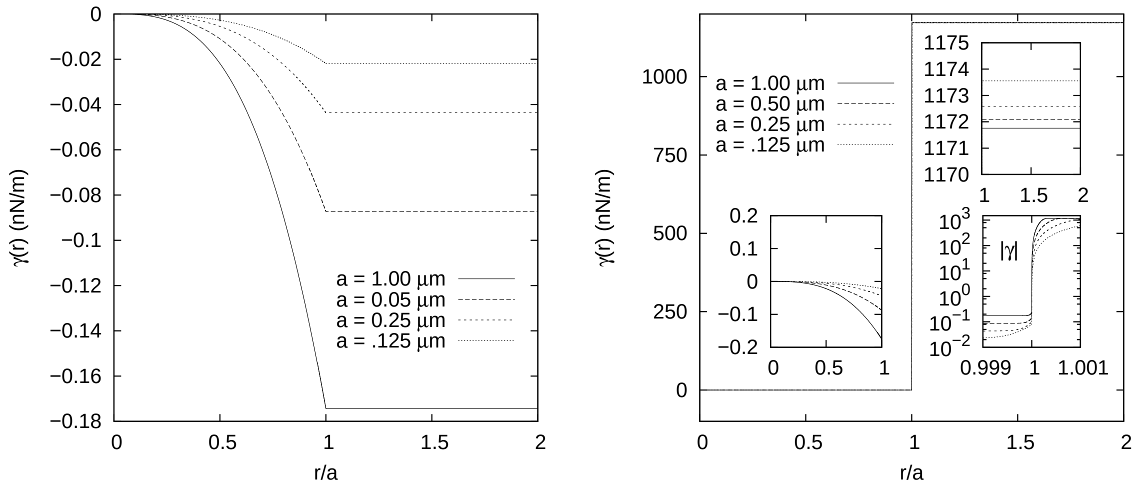

**Figure 6.20:** The stress antiderivative as a function of $r/a$ corresponding to the electrostatic potential of the OW emulsions the right-hand side of fig. 6.1 for $s_{\pm} = 0$ (left) and $s_{\pm} = a_{\pm}$ (right). The largest contribution for the $s_{\pm} = 0$ system comes form the oil area, whereas for the $s_{\pm} = a_{\pm}$ system it comes from the vicinity of interface, the bottom right insert. The bottom left and top right insert have been included to show that the systems are otherwise similar to those with $s_{\pm} = 0$.

configuration. From figures 6.2 and 6.3 it becomes apparent that in the vicinity of the interface the bulk and actual ion density differ by no more than 0.1%, which when integrated over a small decay length becomes vanishing. However, this is not the case in the oil area, as can be seen from figures 6.1 and 6.2. The oil area is smaller than $\kappa_o^{-1}$, such that the stress, $\beta^{-1}\tau(r)$ has not vanished at $r = R$. Furthermore, in the oil area the difference between the bulk and actual density can vary by as much as a factor of five. This combined with the large decay length over which such a difference needs to be integrated produces a non-vanishing contribution to $\gamma$. Similar observations hold true for the equilibrium electrostatic potential.

The contribution of weighting the self-energy potential to the excess surface tension seems to be located in the water area alone. There is a contribution in the oil area as well, but it appears to have negligible effect, although the effect should become more prominent for higher salt concentrations. The change w.r.t. $s_\pm = 0$ is caused by the fact that not $\bar{\phi}$ but $\psi$ changes significantly in the small shell-sized layer around the interface. See fig. 6.21 (right) for the difference between $\psi$ for the step and $\psi$ for the weighted self-energy potential in the vicinity of the oil-water interface. This modification of $\psi$ caused by weighting the potential, strongly affects the ion distributions at the interface.

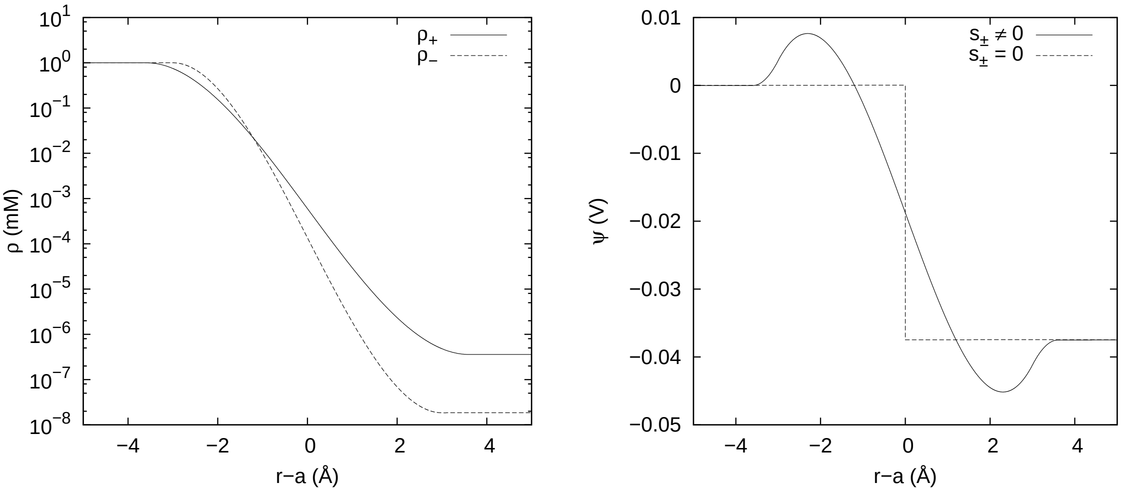

**Figure 6.21:** The ion distributions in the Å-scale vicinity of the OW interface (left) corresponding to the left-hand graph of fig. 6.2 as a function of $(r-a)$, with $s_\pm = a_\pm$. At this scale we can only see the effects of the weighting and not the divergence of the individual density distributions caused by taking various $R$. Note that preferential partitioning combined with the difference in shell size causes there to be a small area of positive charge in the otherwise negative water-side of the double-layer. The difference between $\psi(r)$ in Volts for $s_\pm = 0$ and $s_\pm = a_\pm$ near the interface (right). Note that the discrepancy between $\psi$ and 0.0 mV in area 1 and -37.5 mV in area 2, produce the density profiles in the left-hand graph. The two 'bumps' arise for the interplay between shell-size and self-energy differences.

Because the ion concentration is so low in the oil area, we only see a discernable effect in the water area. The effect of the geometric weighting of the self-energy potential is the appearance of a small layer of positive charge within the water-part of the double-layer. In essence this geometric self-energy modification can be replaced by a step-potential shifted towards the water side of the interface. The effect is to significantly increase the contribution the factor $\rho_i(r) - \rho_{\text{bulk}}(r)$ has to the stress $\beta^{-1}\tau(r)$. The model for emulsions was set up in such a way that it will be a positive contribution, as can be seen form fig. 6.19. Another thing we can see form figures 6.19 and 6.20 is that weighting only affects the behaviour of $\gamma(r)$ in a small area near the interface and leaves the system otherwise unchanged. This gives confidence to our choice for the form of the polynomial expansion of Eq. (5.2). We have added fig. 6.22, which gives the antiderivative of the stress for a couple of $\epsilon_o$ in WO and OW emulsions, to show that the behaviour observed in figures 6.20 and 6.20 holds for different values of $\epsilon_o$ as well.

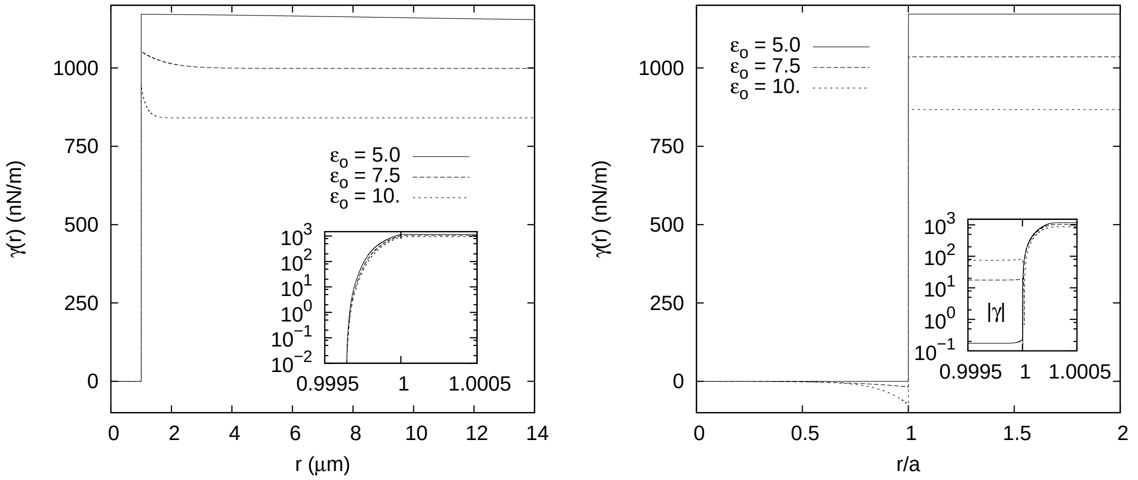

**Figure 6.22:** The antiderivative of the stress, $\gamma(r)$, for a couple of $\epsilon_o$, WO (left) and OW (right), where $s_\pm = a_\pm$. The insets show the behaviour close to the interface. The largest contribution to $\gamma$ comes for the water side of the cell in the vicinity of the interface.

### 6.3.2 The Surface Tension for $x$, $\epsilon_0$ and $\rho_w$ Variation

Let us now discuss the dependence of the surface tension on variations in the droplet volume fraction. Here we will focus on an effect which stood out particularly as not expected by using planar theory. Fig. 6.23 shows the surface tension as a function of the droplet volume fraction at fixed droplet-droplet distance $R = 10.0$ $\mu$m.

In the left-hand side graph of fig. 6.23, we see the decrease of $\gamma$ for a system with $s_\pm = a_\pm$ for decreasing $x$. An interesting question one can ask on the basis of fig. 6.23 (left) is if there is a proper $x \to 0$ limit. For the case of $\epsilon_o = 3.5$ we investigated this, and the result is shown in fig. 6.23 (right). We see that in fact $\gamma$ changes sign for very small $x$ and becomes strongly negative. The transition occurs for $a \approx 11$ nm, so it is well outside the $3.0 - 3.6$ Å range of the shell size. The droplet is small, but it is not so small that it becomes unphysical in size, although one can question the validity of our coarse-grained approach here. It should be noted that the droplet is barely one water Debye-length in size.

Since $a > s_\pm$ the shell contribution to surface tension remains relatively unchanged. The strongly negative surface tension at small $x$ must therefore be sought in a divergent electrostatic contribution to $\gamma$. This is indeed the case, see fig. 6.24, where we have indicated the surface tension of a step self-energy potential as a function of $x$ at fixed $R = 10.0$ $\mu$m. From this figure we can see that the $s_\pm = 0$ surface tension becomes strongly negative, possibly diverging to $\gamma = -\infty$, for $x \to 0$. This effect is caused by the fact that the *surface energy* becomes more or less constant. For a small $a$ there is hardly any decay of $\bar{\phi}$ in the water area and the increase in the size of the oil area for even smaller $a$ does not increase the surface energy significantly. However, dividing this almost constant surface energy by $4\pi a^2$ to obtain the surface tension, shows that $\gamma \propto a^{-2}$ and hence it will become strongly negative for small $a$.

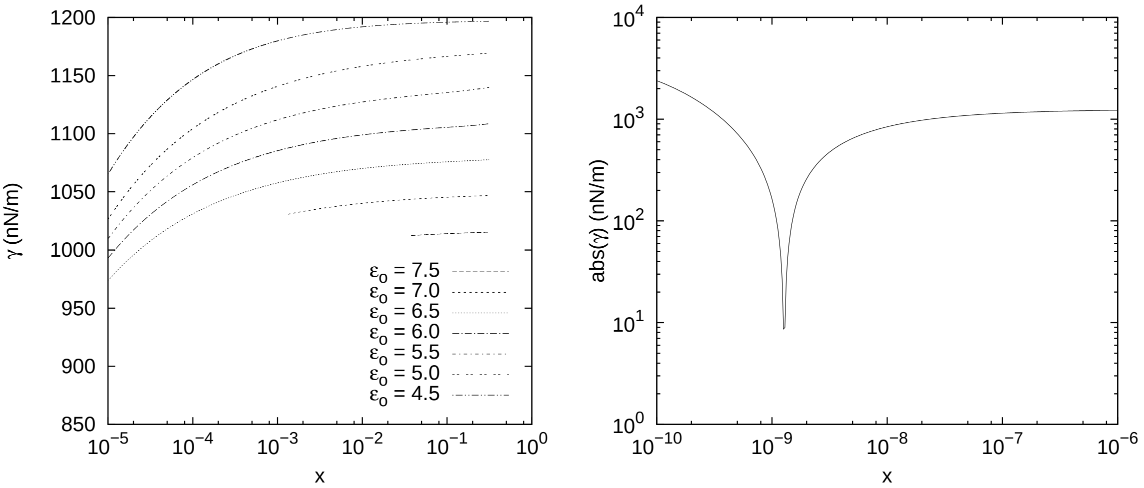

**Figure 6.23:** The surface tension as a function of the droplet volume fraction $x$ in the case of a $s_\pm = a_\pm$ systems, with the other parameters the same as in table 6.1. Note the general tendency of $\gamma$ to decrease with smaller droplet size. In the graph on the right we have given the curve for $\epsilon_o = 3.5$ and extended it to much smaller volume fractions than we have discussed thus far.

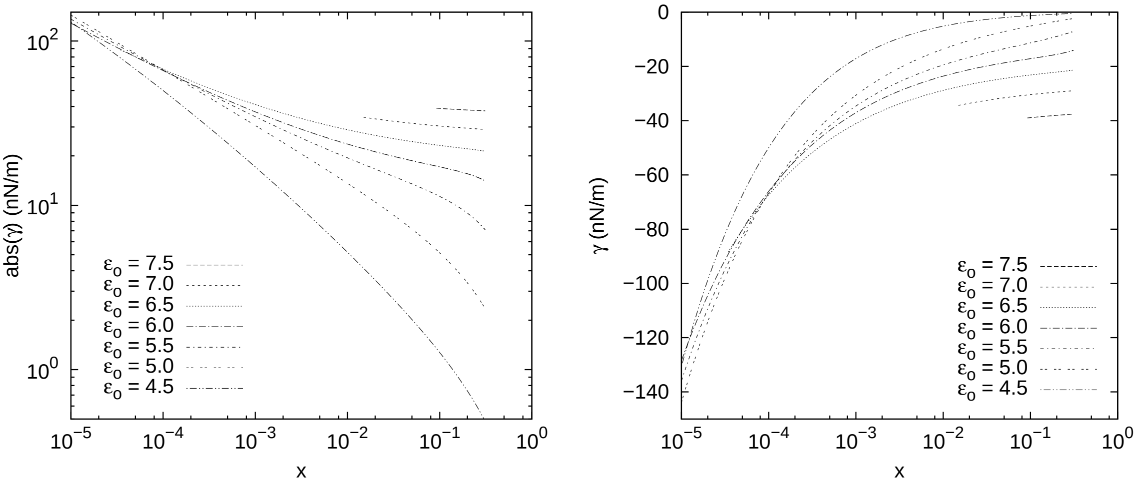

**Figure 6.24:** The logarithmic (left) and linear (right) representation of the surface tension as a function of the water-volume and $\epsilon_o$ respectively. We have $\rho_w = 1.0$ mM, $R = 10.0\ \mu$m and $s_\pm = 0$.

In fig. 6.25, we have indicated the surface tension of a step self-energy potential as a function of $\epsilon_o$ for several $x$, with $R = 10.0\ \mu$m. From this figure we can conclude that the the surface tension will decrease to 0 in the limit $\epsilon_o \rightarrow 1$. This is in accordance with what one theoretically speaking would expect to find. Note for the $\epsilon_o$ considered here we have not yet reached the extremum in $\gamma$ which is located a $\epsilon_o \approx 20$. Also note the 'bump' in the $\epsilon_o$ dependence of $\gamma$ for low $x$. Presumably this effect is caused by the difference in oil and water Debye-length and it is exacerbated by the small droplet size. A similar effect can be seen in fig. 6.26, which gives the surface tension of the weighted self-energy potential as a function of $\epsilon_o$ for several $x$. Again we find that it is only the electrostatic part of the excess surface tension which is influenced by

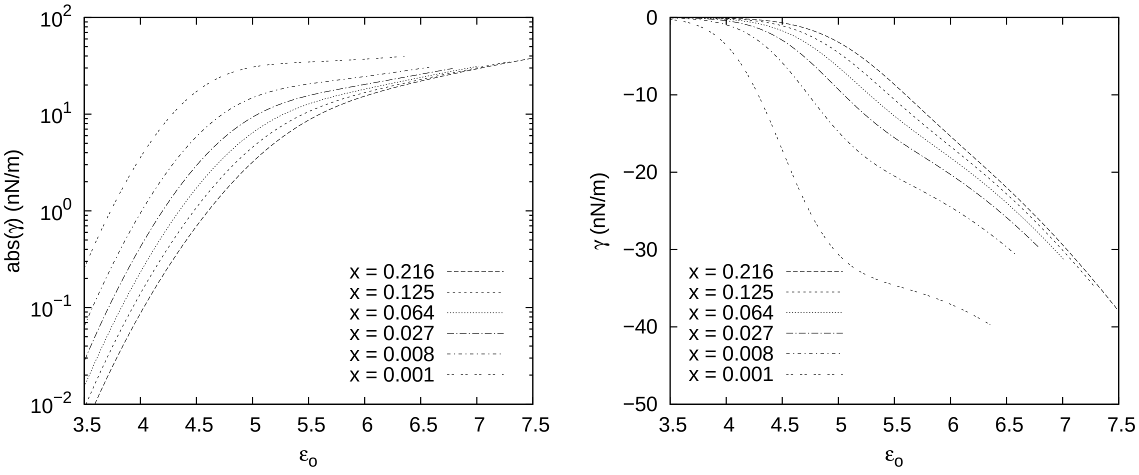

**Figure 6.25:** The surface tension $\gamma$ as a function of $\epsilon_o$ for $x$. Again we have $\rho_w = 1.0$ mM, $R = 10.0\ \mu$m and $s_\pm = 0$.

$x$, by comparing figures 6.25 and 6.26.

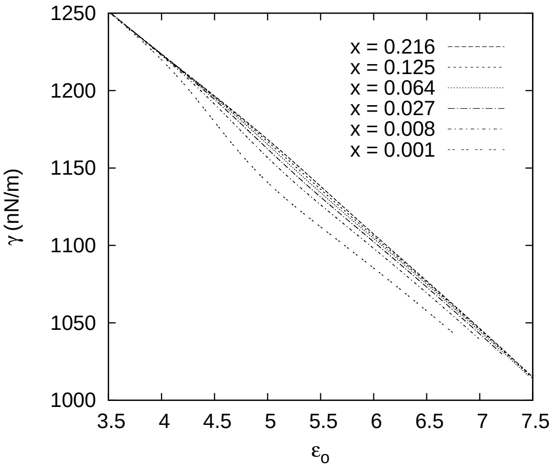

**Figure 6.26:** The surface tension as a function of the relative dielectric constant in oil for $s_\pm = a_\pm$. The systems are otherwise the same as those in fig. 6.24 (right).

We conclude this paragraph by examining the dependence of the surface tension on the bulk salt density in water. Fig. 6.27 shows $\gamma$ for a step self-energy potential as a function of $\rho_w$ for $\epsilon_o = 5$ and several $x$ at constant inter-droplet distance $R = 10.0\ \mu$m. We can see that increasing the salt concentration decreases the surface tension asymptotically. This apparent asymptotic behaviour is related to the charge saturation observed in fig. 6.16. If the salt concentration is such that the electrostatic potential does not change substantially with the addition of more salt, neither the charge or the surface tension will vary.

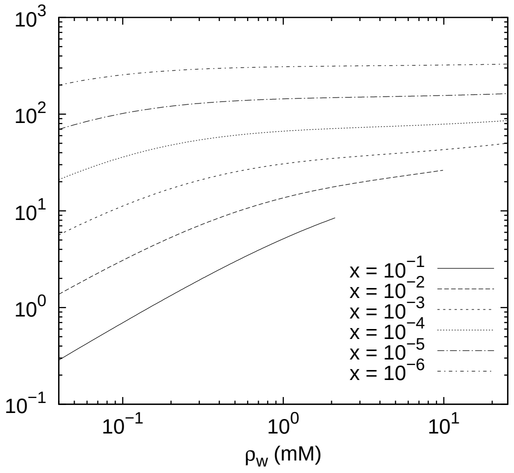

**Figure 6.27:** The surface tension, $\gamma$, as a function of $\rho_w$ for $R = 10.0$ $\mu$m, $\epsilon_o = 5$ and $s_\pm = 0$. For these systems the surface tension is negative.

### 6.3.3 The Effect of Ion Size at Constant $x$.

In this paragraph we will consider the surface tension as a function of $R$ at constant droplet volume fraction, focussing on an effect which stood out as unexpected from a planar point of view. Fig. 6.28 shows the surface tension as a function of the Wigner-cell radius $R$ for several $x$ with $\epsilon_o = 5$.

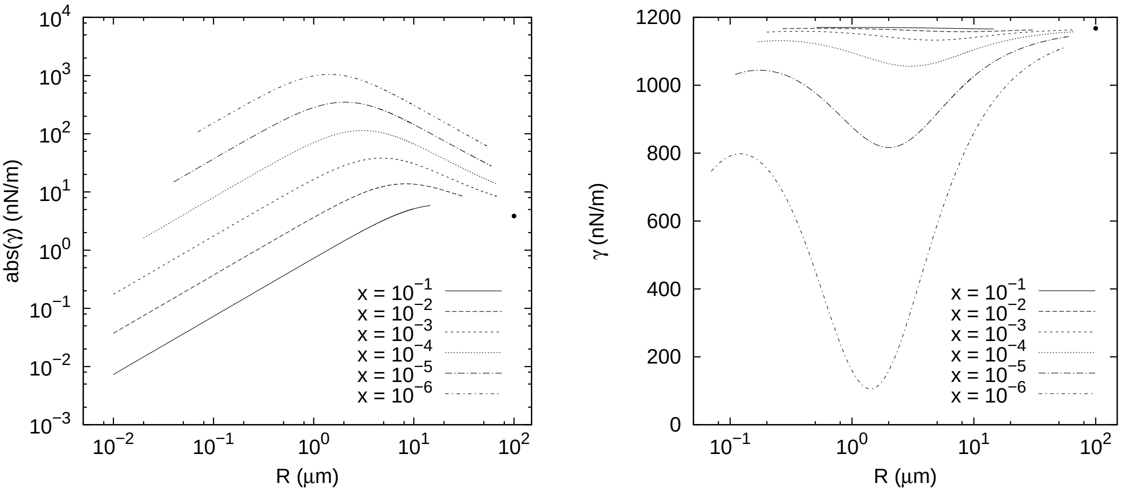

**Figure 6.28:** The surface tension, $\gamma$, as a function of the Wigner-radius for several droplet volume fractions $x$ at $\epsilon_0 = 5.0$, $s_\pm = 0$ (left) with negative $\gamma$ and $s_\pm = a_\pm$ (right). The planar value has been indicated with a dot at $R = 100$, as a means to show the limiting value for all curves as $R \to \infty$.

From fig. 6.28 we can see that $\gamma$ changes substantially with $R$. In the $s_\pm = 0$ system we find $\gamma \propto R$ for small $R$, whereas for large $R$ the behaviour is given by $\gamma - \gamma_p \propto R^{-1}$. The latter was to be expected from the discussion in the previous chapter of the effects of curvature with respect to the planar value. The first can be explained as follows. For smaller $R$, the size of the oil area decreases, since $(R - a) \propto R$ at constant volume fraction. As with the surface charge for small $R$, we find that $R \downarrow 0$ the terms in the integrand of Eq. (4.4) become constant and consequently $\gamma \propto R$.

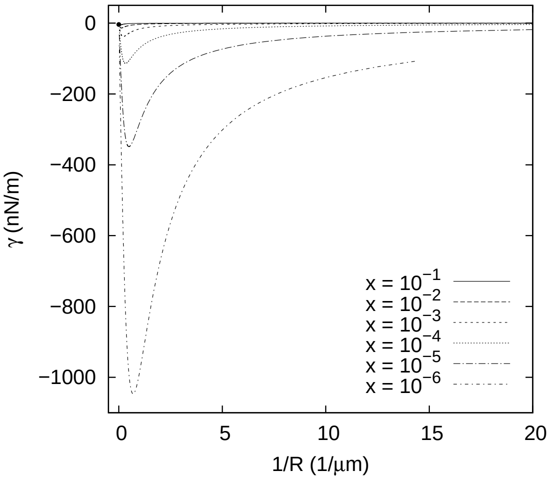

**Figure 6.29:** The surface tension, $\gamma$, corresponding to fig. 6.28, but now represented linearly and as a function of $1/R$ so that the asymptotic behaviour can be more readily seen.

We have included fig. 6.29, showing the $s_{\pm} = 0$ surface tension as a function of $1/R$ for several $x$, to indicate that the asymptotic value is indeed the planar one. It also represents more clearly that for smaller volume fractions $\gamma$ has a minimum, $\gamma_m$, which can be quite deep. This minimum is explained by the cross-over from $\sim R$ to $\sim R^{-1}$ proportionality. The depth of the minimum is directly related to the droplet volume fraction. A smaller droplet, i.e. less water, gives a deeper minimum; see fig. 6.30 (left), showing the depth of the observed minimum as a function of $x$. The Wigner-radius for which the minimum occurs, $R_m$, can also be correlated $x$; see fig. 6.30 (right), showing $R_m$ as a function of $x$. Even this surface tension, with its deep minimum, cannot decrease sufficiently for physically reasonable parameter to influence the regular oil-water surface tension. Note that $\gamma_m$ is more negative for lower volume fractions, but that the corresponding $R_m$ is also smaller. This combination makes that $a_m \equiv \sqrt[3]{x} R_m$ rapidly approaches the nanometre size range with decreasing $\gamma_m$. At this size range the coarse-grained model we are using to describe these emulsions will break down.

## 6.4 Summary

In this chapter we have discussed crystallisation by making use of the plasma-parameter and the theory described in Ref. [10]. We have seen that $\Gamma$ is determined by the subtle interplay of the parameters $R$, $a$, $\rho_w$, $\epsilon_o$ and $a_{\pm}$. This makes the behaviour of the plasma-parameter, especially in the spherical geometry, difficult to predict. There are good indications that for the emulsions we are interested in, the area in parameter space where crystallisation can occur is greatly extended in the spherical geometry w.r.t. the planar area. However, we have also shown that this crystallisation area can be reduced for other emulsions. Our results lead us to conclude

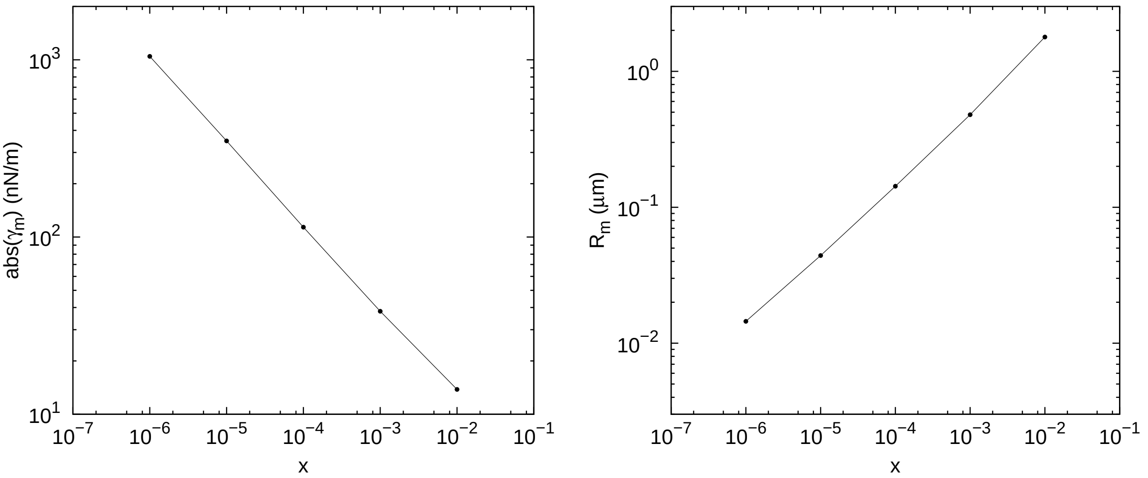

**Figure 6.30:** The size and location of the minimum observed in $\gamma$ in fig. 6.29.

that crystallisation is not as easily achieved as was previously thought, which explains why this phenomena was only recently observed. At this point there are still too many unknowns to dismiss or accept the current theoretical predictions, in the spherical or the planar geometry, on the basis of the experimental results in Ref. [3]. Nevertheless, we are quite confident in our methodology and we expect that crystallisation can be found experimentally in the area of parameter space indicated by our calculations.

We have also seen that the other spherical geometry alters the behaviour of the physical quantities w.r.t. those predicted by planar theory. These effects can be quite dramatic for finite cells, especially for nanoscopic droplets. The most poignant example of such an effect is the extreme difference in surface tension as a function of $R$ for fixed small $x$. We have identified the source of the excess surface tension for $s_{\pm} = 0$ and $s_{\pm} \neq 0$ systems by using the antiderivative of the interfacial stress. In the former case only the oil area contributes, whereas in the latter the finite interfacial thickness causes a significant contribution in the water area close to the interface. This observation lends credibility to the choice for the polynomial expansion discussed in the previous chapter. Using a few basic assumptions about the system we can, to some extent, qualitatively describe the effects of the droplet volume fraction in a Wigner-cell of fixed size, and of $R$ for a fixed $x$. However, making quantitative remarks concerning the physical quantities proves beyond the scope of this research.

# Chapter 7

# Outlook

In the first part of this thesis we have set up the theoretical framework required to describe saline emulsions of oil and water. We have used this to examine the properties of saline emulsions in two instances, namely in the planar limit approximation and by solving the Poisson Equation in the spherical geometry using numerical integration techniques. We have explored the physics of these emulsions and scrutinised the differences between the planar and spherical geometry. Although the planar geometry is a useful tool to make predictions about the systems's behaviour, it has its limitations. Some of these limitations can be addressed by making use of the spherical geometry, but it too has its weaknesses. That is to say, the solution of the Poisson-Boltzmann Equation will describe the effects of curvature, but the expressions are more complex and we often require time consuming numerical methods. In addition, the ease with which parameter dependence of the physical quantities can be observed in the analytic case of the planar approximation is lost in the spherical geometry. The expansion model presented in this thesis attempts to find the middle ground between the two approaches for an infinite Wigner-Seitz cell, where $\kappa_w a$ and $\kappa_o a > 1$. However, there are still many questions left unanswered concerning this polynomial expansion. For instance, the divergence of the expansion coefficients observed for certain ion size ratios and for $s_{\pm} \neq 0$ at high $\rho_w$ would merit further investigation.

Although the author considers this likely, it remains to be checked whether the same or a similar polynomial expansion can be used for droplets in finite Wigner-cells. One criterion on the use of such an expansion would then logically be $\kappa_w(R-a) > 1$ and $\kappa_o(R-a) > 1$ for OW and WO emulsions respectively. Furthermore, one would like to formulate a series/functional expansion which accurately describes the behaviour of physical quantities in nanoscopic droplets, i.e. expansion which works when $\kappa_w a$, $\kappa_o a$, $\kappa_w(R-a)$ and $\kappa_o(R-a) < 1$. There are strong indications that the charge and surface energy in such droplets lend themselves to be modelled in such a way. It should be noted that in addition to formulating such simplifications to explain the mathematics behind our spherically geometric theory, we will also want to compare the behaviour predicted by theory and that found by experiments to a greater extent. Unfortunately, our attempts to do so have been foiled by the lack of experimental data, which can be attributed to the difficulties in carrying out the relevant measurements. It is our hope that this situation can be remedied in the near future, particulary on the subject of the crystallisation of water droplets in oil. A two part approach is required to elucidate the effectiveness of the model used in this thesis, in which both the available experimental and theoretical data for the spherical geometry is greatly extended. The theoretical tools we have developed here should for now prove useful in guiding any future experiments.

Finally, it should be noted that the subject of saline emulsions lends itself well to branch out into a variety of directions. One of these is adding colloids or other surfactants to the system. Another is to examine the effects of an electric field on the ion density distributions. Also, the dynamical aspects of crystal formation are worth further investigation. One would, for instance, like to know whether there is droplet growth after emulsification, but before the crystal is formed, or that emulsification is directly followed by crystallisation. These are only a few of the possibilities left unexplored in this part of the thesis, although the addition of colloidal particles will to an extent be discussed in part II.

# Part II

# Pickering Emulsions

# Chapter 8

# Introduction

In this part we will set up the theoretical means to describe Pickering Emulsions, i.e. emulsions which contain colloids. Here will will take a two-part approach to the problem of devising such a theoretical model. Firstly, we will modify the theory for saline emulsions in the spherical geometry to include a 'surface charge shell'. That is to say, we introduce a spherical surface charge distribution near the interface centred on the droplet. This will be used to model the Pickering Emulsions found in Refs. [2, 6], where thermodynamically stable Pickering Emulsions were found and spontaneous emulsification was observed. Secondly, we will extend the model given in Ref. [5], describing the experiments of Ref. [3], from the planar geometry to the spherical geometry. In Ref. [3] Pickering Emulsions with a large colloid-free exclusion zone between the monolayer of colloids absorbed to the oil-water interface and a bulk colloidal crystal were observed, see fig. 8.1 (left).

It should be noted that the systems of Refs. [2, 6] are fundamentally different from those of Ref. [3]. The former, see figure 8.1 (right), are emulsions of oil and water with either magnetite or Ludox particles adsorbed to the interface. These colloids are in the 10-25 nm size range with emulsion droplets of $\sim 100$ nm. Whereas the latter, see figure 8.1 (left), contains PMMA particles of size $\sim 2$ $\mu$m. In the Pickering Emulsions of Refs. [2, 6], we also have that all the colloids, which were originally added to the oil water system before emulsification, have distributed reasonably evenly over the surfaces of the water droplets and there are no free colloids left. This is in stark contrast with the system of Ref. [3], where there is a colloidal crystal in bulk oil, separated from the colloidal monolayer adsorbed to the interface by a relatively large colloid-free depletion zone, see figure 8.1 (left). Also, the droplet sizes studied in Ref. [3] are much larger, in fact $> 10$ $\mu$m. Since these two types of experiment differ so substantially we believe it appropriate to use two different models to describe the observed effects.

The addition of a surface charge shell is to model Pickering Emulsions for which all the colloids have been adsorbed homogeneously to the surface, is a tremendous simplification with respect to the experiments. However, we are allowed to make this reduction, because there are no free colloids and the absorbed colloids are tightly bound to the interface. This simplified model has the advantage that it is not restricted to colloidal particles absorbed to the interface. It can, for instance, be used to describe charged surfactants as well. In the case of Ref. [3], such a reduction is not possible and the full effects of colloid-colloid, colloid-ion and colloid-medium interactions have to be taken into account. This will result in a complicated model with approximates the experimental observations to a reasonable degree, see Ref. [5].

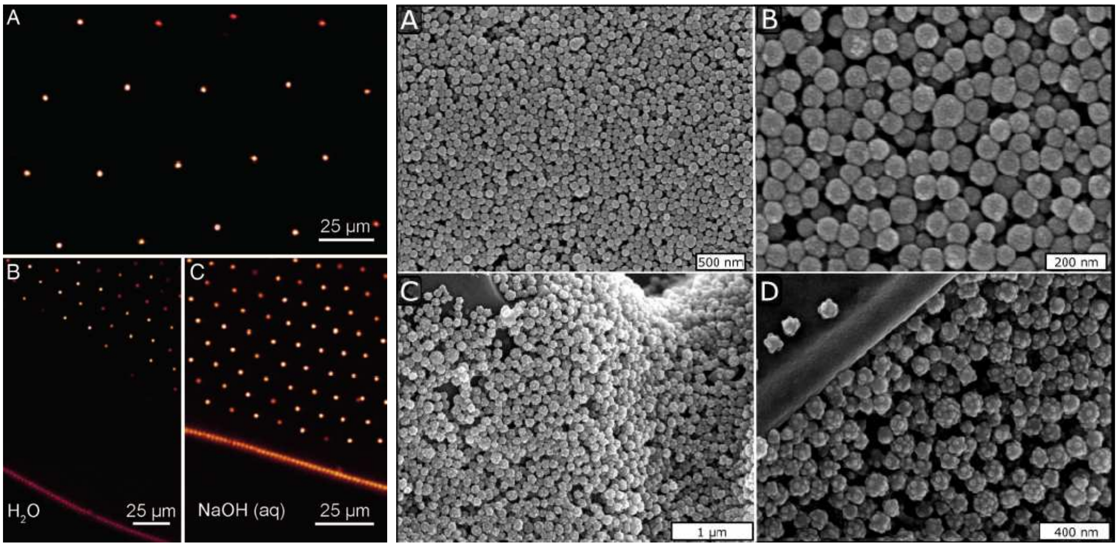

**Figure 8.1: Left:** *Confocal micrographs of PMMA spheres (radius 1.08 $\mu$m) suspended in CHB-decalin, in contact with water. (A) Part of a (110) plane of the bodycentered-cubic colloidal crystal in the bulk oil phase. (B) Particle monolayer, followed by a large zone depleted of particles near the water-suspension interface. (C) With 1.6 $\mu$M NaOH in the water phase the depleted zone in the oil phase shrinks considerably.* **Right:** *Scanning electron micrograph showing polymerized TPM emulsion droplets with adsorbed (A, B) magnetite and (C, D) silica Ludox particles visible as white spots on the droplet surfaces. Without polymerization, it is not possible to image an emulsion in this way.* Reproduced from Ref. [3] and Ref. [6] respectively with the author's permission.

# Chapter 9

# Theory for Droplets with Surface Charge

## 9.1 Approach

In this chapter, we formulate a simple model to describe Pickering Emulsions of homogenously charged colloidal particles as observed in Refs. [2, 6]. We do so by adding a single component to the Grand Potential Functional of Part I, Eq. (2.4). This term accounts for a shell of surface charge located in the vicinity of the oil-water interface. Since the emulsions observed in Refs. [2, 6] did not have any free colloids, that is to say all colloids were adsorbed to the interface, we may include their presence in the emulsion in such a manner. In fact, this shell of surface charge can be used to model more than colloids. Charging of the interface may also occur by adding surfactants or by self-dissociation of the oil molecules in contact with water. Therefore, the Grand Potential formulated here has a wide range of applicability. From this Grand Potential we will derive the Poisson Equation with appropriate boundary conditions. Finally we will discuss the physical quantities one may determine by solving the Poisson Equation.

## 9.2 Grand Potential with Surface Charge Shell

We refer to Chapter 2 for an overview of way in which a saline emulsion without interfacial surface charge is modelled. We have a spherically symmetric Wigner-cell of radius $R$ centred around a droplet of radius $a$. In this cell we have density distributions $\rho_{\pm}(r)$ for the ion species, where the presence of the oil and water background is introduced in the form of an external potential. This potential is based on the self-energy difference of the ions between water and oil and is given by $V_{\pm}(r)$, Eq. 2.1 for the step and Eq. 2.3 for the weighted self-energy potential.

To describe the effects of charged particles adsorbed to the oil-water interface, we introduce the following charge density to the system $\rho_{\text{surf}}(r) = \sigma\delta(r - (a + s))$, with $\sigma$ a surface charge and $s$ the separation between this charge shell and the interface. Typically $s$ will be in the order of a few nm, and it can be both positive and negative depending on the area the colloids/surfactants prefer. Recall that area 1 refers to the droplet and area 2 to the medium. With the addition of

$\rho_{\text{surf}}$ we may derive the following Grand Potential Functional

$$\begin{aligned}\beta\Omega[\rho_\pm] &= \sum_{i=\pm}\int \mathrm{d}\mathbf{r}\rho_i(r)\left(\log\left(\frac{\rho_i(r)}{z_i}\right) - 1 + \frac{1}{2}q_i\phi(r,[\rho_\pm]) + \beta V_i(r)\right) + \\ & \quad 2\pi(a+s)^2\sigma\phi(a+s,[\rho_\pm]),\end{aligned} \tag{9.1}$$

where the electrostatic potential is modified with respect to the one given in Chapter 2 as follows

$$\phi(r,[\rho_\pm]) = 4\pi(a+s)^2\sigma G(r,a+s) + \int \mathrm{d}\mathbf{r}' \sum_{i=\pm} q_i\rho_i(r')G(r,r'), \tag{9.2}$$

with $G(r,r')$ is a Greens function, such that it satisfies the Poisson Equation

$$\nabla_{\mathbf{r}}\cdot(\epsilon(r)\nabla_{\mathbf{r}}G(r,r')) = -4\pi\lambda_B\delta(r-r'). \tag{9.3}$$

Minimising the Grand Potential w.r.t. the density profiles yields

$$\begin{aligned}\left.\frac{\delta\beta\Omega[\rho_\pm]}{\delta\rho_i(r)}\right|_{\bar{\rho}_\pm} &= \log\left(\frac{\bar{\rho}_i(r)}{z_i}\right) + \beta V_i(r) + q_i\phi(r,[\bar{\rho}_\pm]) \\ &\equiv \log\left(\frac{\bar{\rho}_i(r)}{z_i}\right) + \beta V_i(r) + q_i\bar{\phi}(r),\end{aligned} \tag{9.4}$$

which is the same as Eq. 2.7. To derive this form we have used the following property of the electrostatic potential

$$\begin{aligned}\frac{\delta}{\delta\rho_k(r')}\phi(r,[\rho_\pm]) &= \\ \frac{\delta}{\delta\rho_k(r')}\left[4\pi(a+s)^2\sigma G(r,a+s) + \int \mathrm{d}\mathbf{r}''\sum_{i=\pm}q_i\rho_i(r'')G(r,r'')\right] &= \\ \int \mathrm{d}\mathbf{r}''\sum_{i=\pm}q_i\frac{\delta}{\delta\rho_k(r')}\rho_i(r'')G(r,r'') &= q_kG(r,r').\end{aligned}$$

This can be applied in the following calculation

$$\begin{aligned}2\pi(a+s)^2\sigma\frac{\delta}{\delta\rho_k(r')}\phi(a+s,[\rho_\pm]) + \sum_{i=\pm}\int \mathrm{d}\mathbf{r}\rho_i(r)\frac{1}{2}q_i\frac{\delta}{\delta\rho_k(r')}\phi(r,[\rho_\pm]) &= \\ 2\pi(a+s)^2\sigma q_kG(a+s,r') + \sum_{i=\pm}\int \mathrm{d}\mathbf{r}\rho_i(r)\frac{1}{2}q_iq_kG(r,r') &= \\ \frac{1}{2}q_k\left[4\pi(a+s)^2\sigma G(a+s,r') + \sum_{i=\pm}\int \mathrm{d}\mathbf{r}\rho_i(r)q_iG(r,r')\right] &\overset{(9.2)}{=} \frac{1}{2}q_k\phi(r,[\bar{\rho}_\pm]),\end{aligned}$$

to eliminate the factor 1/2 one would obtain if the implicit $\rho_\pm$ dependence had not been taken into account in deriving Eq. (9.4). The equilibrium Grand Potential, which follows from Eq. (9.1) and Eq. (9.2), is thus given by

$$\beta\Omega[\bar{\rho}_\pm] = 2\pi(a+s)^2\sigma\bar{\phi}(a+s) - \sum_{i=\pm}\int \mathrm{d}\mathbf{r}\bar{\rho}_i(r)\left(1 + \frac{1}{2}q_i\bar{\phi}(r)\right). \tag{9.5}$$

Note that from Eq. (9.4) we obtain the following form for the equilibrium density distributions

$$\bar{\rho}_i(r) \;=\; \rho_s(r)\exp(-q_i[\bar{\phi}(r)+\phi_c(r)]), \tag{9.6}$$

with $\rho_s(r)$ as in Eq. (2.10) and $\phi_c(r)$ the Donnan potential given by

$$\phi_c(r) \;\equiv\; \beta\frac{V_+(r)-V_-(r)}{2}.$$

## 9.3 The Poisson Equation

### 9.3.1 Derivation

In this section we will derive the Poisson Equation for this system. The calculation is analogous to that applied in section 2.5 to derive the Poisson-Boltzmann Equation for saline emulsions. Using the form of the electric displacement $\mathbf{D}(r) \equiv -\epsilon(r)\nabla_{\mathbf{r}}\bar{\phi}(r)$, we obtain

$$\begin{aligned}
\nabla_{\mathbf{r}}\cdot\mathbf{D}(r) &= -\nabla_{\mathbf{r}}\cdot(\epsilon(r)\nabla_{\mathbf{r}}\bar{\phi}(r)) \\
&= -\nabla_{\mathbf{r}}\cdot\left(\epsilon(r)\nabla_{\mathbf{r}}\left[4\pi(a+s)^2\sigma G(r,a+s)+\int \mathrm{d}\mathbf{r}'\sum_{i=\pm} q_i\rho_i(r')G(r,r')\right]\right) \\
&= -4\pi(a+s)^2\sigma\nabla_{\mathbf{r}}\cdot(\epsilon(r)\nabla_{\mathbf{r}}G(r,a+s)) - \int \mathrm{d}\mathbf{r}'\sum_{i=\pm} q_i\rho_i(r')\nabla_{\mathbf{r}}\cdot(\epsilon(r)\nabla_{\mathbf{r}}G(r,r')) \\
&\overset{(9.3)}{=} 16\pi^2\lambda_B(a+s)^2\sigma\delta(r-(a+s)) + 4\pi\lambda_B\int \mathrm{d}\mathbf{r}'\sum_{i=\pm} q_i\rho_i(r')\delta(r-r') \\
&= 4\pi\lambda_B\left(\sum_{i=\pm} q_i\rho_i(r) + 4\pi(a+s)^2\sigma\delta(r-(a+s))\right) \\
&= -8\pi\lambda_B\rho_s(r)\sinh(\bar{\phi}(r)+\phi_c(r)) + 4\pi\lambda_B\sigma\delta(r-(a+s)),
\end{aligned}$$

which we may rewrite to

$$\nabla^2_{\mathbf{r}}\bar{\phi}(r) \;=\; \kappa^2(r)\sinh(\bar{\phi}(r)+\phi_c(r)) - \frac{16\pi^2\lambda_B}{\epsilon(r)}(a+s)^2\sigma\delta(r-(a+s)). \tag{9.7}$$

by using local commutativity of $\epsilon(r)$ and $\nabla_{\mathbf{r}}$ and by introducing the Debye-length profile, $\kappa(r)$.

### 9.3.2 Boundary Conditions

The addition of a shell of surface charge to the system will modify the boundary conditions given in section 2.5.2 for Eq. (2.16) to a new set for Eq. (9.7). Here we will need to consider two cases, one $s = 0$ and two $s \neq 0$, since in the former the dielectric jump coincides with the surface charge shell, whereas in the latter they do not coincide. Let us suppose that $s = 0$ then

- BC1: By radial symmetry of the problem we require that $(\nabla_{\mathbf{r}}\bar{\phi})(0) = 0$.
- BC2: There is no free surface charge, but there is a surface charge $\sigma$, therefore

$$\lim_{r\uparrow a}\epsilon(r)\nabla_{\mathbf{r}}\bar{\phi}(r) - \lim_{r\downarrow a}\epsilon(r)\nabla_{\mathbf{r}}\bar{\phi}(r) \;=\; 4\pi\lambda_B\sigma.$$

- BC3: The electrostatic potential is continuous everywhere, therefore it is continuous at the interface, $\lim_{r\downarrow a}\bar{\phi}(r) = \lim_{r\uparrow a}\bar{\phi}(r)$.
- BC4: The Wigner-Seitz cells are charge neutral, hence $(\nabla_{\mathbf{r}}\bar{\phi})(R) = 0$.

If $s \neq 0$ the boundary conditions are given by

- BC1: By radial symmetry of the problem we require that $(\nabla_{\mathbf{r}}\bar{\phi})(0) = 0$.
- BC2: There is no free surface charge and no surface charge at the interface, therefore

$$\lim_{r\uparrow a}\epsilon(r)\nabla_{\mathbf{r}}\bar{\phi}(r) - \lim_{r\downarrow a}\epsilon(r)\nabla_{\mathbf{r}}\bar{\phi}(r) \quad = \quad 0.$$

- BC3: The electrostatic potential is continuous everywhere, therefore it is continuous at the interface, $\lim_{r\downarrow a}\bar{\phi}(r) = \lim_{r\uparrow a}\bar{\phi}(r)$.
- BC4: There is a surface charge $\sigma$ at $r = a + s$, therefore

$$\lim_{r\uparrow(a+s)}\nabla_{\mathbf{r}}\bar{\phi}(r) - \lim_{r\downarrow(a+s)}\nabla_{\mathbf{r}}\bar{\phi}(r) \quad = \quad \frac{4\pi\lambda_B\sigma}{\epsilon(a+s)}.$$

- BC5: The electrostatic potential is continuous everywhere, therefore it is continuous at $r = a + s$, $\lim_{r\downarrow(a+s)}\bar{\phi}(r) = \lim_{r\uparrow(a+s)}\bar{\phi}(r)$.
- BC6: The Wigner-Seitz cells are charge neutral, hence $(\nabla_{\mathbf{r}}\bar{\phi})(R) = 0$.

Using these boundary conditions we can in principle solve the Poisson Equation and find the equilibrium density profiles. Solving Eq. (9.7) is not possible algebraically and we therefore require approximation techniques, both algebraic and numeric. It is again possible to perform a planar limit approximation, in which the equation can be solved analytically if $s = 0$. The techniques employed in this approximation are similar to those described in Chapter 3. Numerical integration schemes similar to those of Chapter 4 can be applied to study the Poisson Equation in the spherical geometry.

## 9.4 Physical Quantities

### 9.4.1 The Surface Charge Shell

Before we begin describing the physical quantities one can determine in this type of emulsive system, we should first give some attention to the value of the surface charge on the shell, i.e. $\sigma$. Our calculations are based on a Wigner-Seitz cell model, which partitioned a volume $V$ into $N$ cells, since we assumed that there are $N$ droplets. The parameters $a$ and $R$ were chosen such that $V/N = 4\pi R^3/3$ and the oil : water volume fraction in a single cell is that of the emulsion. We assume that all the surfactant particles/colloids in the emulsion are evenly distributed over the oil-water interface and that they have charge $Z_c$. Let us also assume that there was an initially homogeneous colloid density, $\rho_c$, in the system before emulsification.

There are therefore $N_c = \rho_c V$ particles in the entire emulsion and $N_c/N = \rho_c R^3/a^3$ colloids per droplet. The surface charge is then given by

$$\sigma = \frac{Z_c \rho_c}{4\pi} \frac{R^3}{a^5}.$$

This form of the surface charge enables us to study the effect of varying the composition of the system under the constraint that the colloid density remains constant. This will prove useful when determining the thermodynamically favoured composition, by calculating the excess surface tension as a function of $x$ at constant $R$ and of $R$ at constant $x$.

### 9.4.2 Profiles and Quantities

The physical quantities one can determine are similar to those given in Chapter 4. Obviously we have the ion density profiles, Eq. 9.6, and the Grand Potential, Eq. 9.5. From this we may determine the excess surface tension $\gamma \equiv (\Omega[\bar{\rho}_\pm] - \Omega[\rho_{\text{bulk}}])/(4\pi a^2)$ due to charge effects. The surface tension becomes

$$\beta\gamma = \frac{(a+s)^2\sigma}{2a^2}\bar{\phi}(a+s) - \frac{1}{a^2}\sum_{i=\pm}\int_0^R \mathrm{d}r\; r^2 \left(\rho_i(r) - \rho_{\text{bulk}}(r) + \frac{1}{2}q_i\rho_i(r)\bar{\phi}(r)\right),$$

with $\rho_{\text{bulk}}(r) = \rho_{s,1}$ if $0 < r < a$ and $\rho_{\text{bulk}}(r) = \rho_{s,2}$ if $a < r < R$, see Chapter 2. Since our model is based on the assumption that the surface charge shell is a part of the droplet, we may define the droplet charge as

$$Z_1 = 4\pi(a+s)^2\sigma + \int_0^a \mathrm{d}\mathbf{r}\left\{\bar{\rho}_+(r) - \bar{\rho}_-(r)\right\}.$$

The medium will have charge

$$Z_2 = \int_a^R \mathrm{d}\mathbf{r}\left\{\bar{\rho}_+(r) - \bar{\rho}_-(r)\right\},$$

with $Z_1 = -Z_2$. Note that for these systems the DLVO potential, Eq. 4.7, can still be used as well as the plasma-parameter, Eq. 4.8, defined in the theory of Refs. [5, 9, 10]. Provided we use the ‘modified’ charge, i.e. the charge of the droplets including the charge on the shell, in determining $\Gamma$.

At this stage we are unable to show any numerical results for emulsions with this surface charge shell. Work on these emulsions in the planar limit is being carried out, but the results are too preliminary to be included in this thesis. There are early indications, though, that the excess surface tension can become sufficiently negative to modify the regular surface tension for certain parameter regimes within this model. However, we must stress the novelty of this approach and that it will be some time before the systems have been studied with the same rigour as saline emulsions in the spherical geometry have been in Part I.

# Chapter 10

# Theory for Colloidal Suspensions in Oil-Water Systems

## 10.1 Approach

In this chapter, we describe the statistical mechanical background required to treat Pickering Emulsions of homogenously charged colloidal particles as reported in Ref. [3]. We give the Grand Potential Functional of a generic Pickering Emulsion, using a Pieranski potential [16] to model wetting of the colloids at the interface. Next, we apply DFT to this Grand Potential to derive a self-consistent set of equations for the ionic and colloidal density profiles. From this set we may obtain the Poisson-Boltzmann equation for Pickering Emulsions with appropriate boundary conditions. We will also discuss solution schemes for the self-consistent equations and the numerical approximation techniques employed therein.

## 10.2 Pickering Emulsions Modelled

### 10.2.1 The Colloid Induced External Potential

The Pickering Emulsions of Ref. [3] are basically the emulsion of water and oil described in Part I with colloidal particles added. Therefore, we may recycle much of the theory discussed in Part I and we can concentrate on the effects of adding colloids. We consider an emulsion of total volume $V$ containing $N$ droplets with average radius $a$ and average inter droplet distance $R$, as measured from the centre-of-mass. We again partition the system into charge neutral Wigner-Seitz cells, which we conveniently symmetrise to the spherical geometry. The media are considered incompressible linear dielectrics, which means that the solvent background can be characterised by its dielectric constant alone. We course-grain the ions and colloids into ionic and colloidal density profiles, $\rho_\pm(r)$ and $\rho(r)$ respectively. The external potential for the ions in the Grand Potential is given by Eq. (2.1) or Eq. (2.3), depending on whether we are working with step self-energy potentials or weighted self-energy potentials respectively. The external potential for the colloids is related to the total regular surface energy of the system. By regular we mean the bare oil-water, oil-colloid and water-colloid surface energy/tension, where electrostatic effects are not taken into account.

In this section we follow Pieranski's geometric argument, see Ref. [16], to derive this external potential acting on the colloids. Henceforth we will call this potential the Pieranski potential. Let $a_c$ be the radius of the colloid and assume that the colloidal particles prefer area 1, i.e. the droplet. When a colloid is completely in area 1, i.e. $0 < r < a - a_c$, its total regular surface energy is given by

$$E_s \;=\; 4\pi a^2\gamma_{12} + 4\pi a_c^2\gamma_{1c},$$

where $\gamma_{12}$ is the regular area 1 - area 2 surface tension, which in our case will be the oil-water surface tension, and $\gamma_{1c}$ is the regular area 1 - colloid surface tension. Similarly, if the colloid is completely in area 2, i.e $a + a_c < r < R$, the total surface energy is given by

$$E_s \;=\; 4\pi a^2\gamma_{12} + 4\pi a_c^2\gamma_{2c},$$

with $\gamma_{2c}$ the area 2 - colloid surface tension. For $a - a_c < r < a + a_c$ we find that

$$E_s \;=\; \pi\left(4a^2 + \frac{a}{r}((r-a)^2 - a_c^2)\right)\gamma_{12} + \pi\frac{a_c}{r}(a^2 - (r-a_c)^2)\gamma_{1c} + \pi\frac{a_c}{r}((r+a_c)^2 - a^2)\gamma_{2c},$$

using a little geometry.

By now appropriately shifting the energies we find the following external potential

$$\beta V(r) \;=\; \begin{cases} 0 & \text{if } 0 < r < a - a_c; \\[1ex] \frac{\pi a}{r}((r-a)^2 - a_c^2)\gamma_{12} + \\ \frac{\pi a_c}{r}((r+a_c)^2 - a^2)\Delta_{\gamma c} & \text{if } a - a_c < r < a + a_c; \\[1ex] 4\pi a_c^2\Delta_{\gamma c} & \text{if } a + a_c < r < R, \end{cases}$$

if the colloids prefer area 1 and

$$\;=\; \begin{cases} 4\pi a_c^2\Delta_{\gamma c} & \text{if } 0 < r < a - a_c; \\[1ex] \frac{\pi a}{r}((r-a)^2 - a_c^2)\gamma_{12} - \\ \frac{\pi a_c}{r}((r-a_c)^2 - a^2)\Delta_{\gamma c} & \text{if } a - a_c < r < a + a_c; \\[1ex] 0 & \text{if } a + a_c < r < R, \end{cases} \tag{10.1}$$

if the colloids prefer area 2, where $\Delta_{\gamma c} = |\gamma_{2c} - \gamma_{1c}|$. Note that the Pieranski potential for the colloids only depends on the oil-water interfacial tension and the difference in colloid-water and colloid-oil interfacial tension. Typically, we will use $\gamma_{ow} = 10$ mN/m, $\gamma_{cw} = 10$ mN/m and $\gamma_{co} = 1$ mN/m, hence $\Delta_{\gamma c} = 9$ nN/m.

Note that the Pieranski potential, Eq. (10.1), has a deep minimum if $\Delta_{\gamma c} < \gamma_{12}$, located at

$$r^* \;=\; \sqrt{a^2 - a_c^2}\sqrt{\frac{a\gamma_{12} - a_c\Delta_{\gamma c}}{a\gamma_{12} + a_c\Delta_{\gamma c}}}$$

and

$$\;=\; \sqrt{a^2 - a_c^2}\sqrt{\frac{a\gamma_{12} + a_c\Delta_{\gamma c}}{a\gamma_{12} - a_c\Delta_{\gamma c}}} \tag{10.2}$$

respectively. If the potential has such a minimum the colloids will wet at the interface with wetting angle $\theta$ defined by $r^* - a \equiv a\cos(\theta)$. When $\Delta_{\gamma c} \geq \gamma_{12}$ the potential is monotonic and the system is non-wetting.

### 10.2.2 The Grand Potential in Carnahan-Starling Approximation

Using the external potential for the ions and the Pieranski potential for the colloids we find the following Grand Potential

$$\begin{aligned}
\beta\Omega[\rho,\rho_\pm] &= \beta\mathcal{F}[\rho,\rho_\pm] + \beta\int \mathrm{d}\mathbf{r}\rho(r)(V(r)-\mu) + \beta\sum_{i=\pm}\int \mathrm{d}\mathbf{r}\rho_i(r)(V_i(r)-\mu_i) \\
&= \sum_{i=\pm}\int \mathrm{d}\mathbf{r}\rho_i(r)\left(\log(\rho_i(r)\Lambda_i^3) - 1 + \frac{1}{2}q_i\phi(r,[\rho,\rho_\pm]) + \beta V_i(r) - \beta\mu_i\right) + \\
&\quad \int \mathrm{d}\mathbf{r}\rho(r)\left(\log(\rho(r)\Lambda^3) - 1 + \frac{1}{2}q\phi(r,[\rho,\rho_\pm]) + \beta V(r) - \beta\mu + \Psi(\bar{\eta}(r))\right) \\
&= \sum_{i=\pm}\int \mathrm{d}\mathbf{r}\rho_i(r)\left(\log\left(\frac{\rho_i(r)}{z_i}\right) - 1 + \beta V_i(r)\right) + \\
&\quad \int \mathrm{d}\mathbf{r}\rho(r)\left(\log\left(\frac{\rho(r)}{z}\right) - 1 + \beta V(r)\right) + \\
&\quad \int \mathrm{d}\mathbf{r}\left(\rho(r)\Psi(\bar{\eta}(r)) + \frac{1}{2}Q(r)\phi(r,[\rho,\rho_\pm])\right),
\end{aligned} \tag{10.3}$$

where $\mu$ is the chemical potential of the colloids, $\mu_i$ the chemical potential of the ions, $\Lambda_i$ the thermal wavelength of the ions, $\Lambda$ the thermal wavelength of the colloids, $z_i$ the fugacity associated with the ions, $z$ the colloid fugacity, $q$ the charge of the colloid in elementary charges, $q_\pm = \pm 1$ and

$$Q(r) \equiv q\rho(r) + q_+\rho_+(r) + q_-\rho_-(r)$$

the total local charge density. Again integration over the the entire Wigner-Seitz cell is implied by the integral symbol. To include the excess Free Energy caused by colloid-colloid interactions, we have used the Carnahan-Starling approximation to describe the hard-core colloid-colloid interactions in a non-local treatment. This Carnahan-Starling term is given by $\Psi(\bar{\eta}(r))$, with

$$\Psi(\bar{\eta}) = \frac{4\bar{\eta} - 3\bar{\eta}^2}{(1-\bar{\eta})^2},$$

where $\bar{\eta}$ is the weighted colloidal packing-fraction, to which we will come back in the next paragraph. The electric potential for Pickering Emulsions in Eq. (10.3) is given by

$$\phi(r,[\rho,\rho_\pm]) = \int \mathrm{d}\mathbf{r}' Q(r')G(r,r') \ ,$$

where $G(r',r)$ is a Greens function, such that the following Poisson Equation is satisfied

$$\nabla_\mathbf{r}\cdot(\epsilon(r)\nabla_\mathbf{r}G(r,r')) = -4\pi\lambda_B\delta(r-r').$$

### 10.2.3 Weighted Packing-Fraction

A non-local treatment of the hard-core interactions is necessary to describe the extremely localised absorbed colloidal monolayer in the case of wetting realistically. This non-locality can be taken into account by weighting the local colloidal packing-fraction. The local packing-fraction is defined in terms of the colloid density as

$$\eta(r) \;=\; \frac{4\pi a_c^3}{3}\rho_c(r).$$

The non-local packing-fraction, or weighted packing-fraction, is obtained from $\eta(r)$ by local integration with appropriate weight, i.e.

$$\bar{\eta}(r) \;=\; \int_{r-2a_c}^{r+2a_c} \mathrm{d}r' w(r,r')\eta(r')$$

is the weighted colloidal packing-fraction, with weight

$$w(r,r') \;=\; \frac{3r'}{32a_c^3 r}(4a_c^2-(r-r')^2). \tag{10.4}$$

The weight in Eq. (10.4) is determined as follows. In Ref. [17] the weight for a hard-sphere system given by Tarazona is

$$w_T(r) \;=\; \frac{3}{32\pi a_c^3}\theta(2a_c-|r|),$$

where in this case $r$ is the distance measured the origin of the colloid and $\theta$ is the Heaviside function. In the above discussion such a Heaviside function has been absorbed into the integration boundaries. We modify Tarazona's weight in the following way. The colloid distribution at a point $r$ is weighted with the surrounding colloidal distributions, within a sphere of radius $2a_c$. The choice of $2a_c$ is related to the excluded volume for a single colloid.

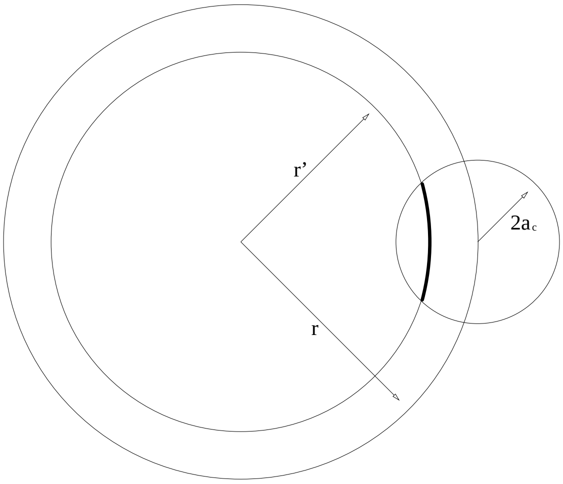

**Figure 10.1:** The surface area of a sphere with radius $r'$ centred around the origin enclosed by a sphere with radius $2a_c$ centred around $(r,0,0)$ indicated in bold. The sphere has been represented by a cut-through in the $x/z$-plane. The enclosed surface area, given by the surface of revolution of the bold line, is used in weighing the colloid density distribution at $r$.

The density at a point $r'$, contributes only if $r-2a_c < r' < r+2a_c$, according to the following scheme. The contribution is proportional to the surface area of the sphere with radius $r'$ centred at the origin, which is enclosed by the sphere of radius $2a_c$ centred at $r$. See fig. 10.1 for a picture of the geometry involved. We divide this surface area by $32\pi a_c^3/3$ to normalise the weight function, i.e.

$$\int_{r-2a}^{r+2a} \mathrm{d}r' w(r,r') \;=\; 1,$$

and obtain Eq. (10.4). It should be noted that this normalisation of the weight will only work a distance of $2a_c$ away from the boundaries of the Wigner-cell. That is to say, if $r \in [0, 2a_c]$ or $r \in [R-2a_c, R]$ the definition of weighting will need to change to compensate for the fact that we cannot weight with $\eta(r)$ outside of domain on which the packing-fraction is defined. In fact, weighting the packing-fraction should be done as follows

$$\bar{\eta}(r) \;=\; \frac{\int_{\max(0,r-2a_c)}^{\min(r+2a_c,R)} \mathrm{d}r' w(r,r')\eta(r')}{\int_{\max(0,r-2a_c)}^{\min(r+2a_c,R)} \mathrm{d}r' w(r,r')},$$

where obvious care needs to be taken when $r = 0$. We will not use this contrived notation, however, instead we will rely on the reader to judge when this form of weighting is appropriate.

## 10.3 Density Functional Theory

### 10.3.1 Poisson Equation

Now that we have formulated a Grand-Potential to model the behaviour of Pickering Emulsions, we can apply DFT to derive the self-consistent set of equations for the density profiles and the electrostatic potential. Using these equations, with appropriate boundary conditions, we can find the corresponding Poisson-Boltzmann Equation. Let $\bar{\rho}_\pm$ and $\bar{\rho}$ be the equilibrium ion density profiles and the equilibrium colloid density profile respectively. Minimising the Grand Potential Functional, Eq. (10.3), with respect to the density distributions we obtain

$$\left.\frac{\delta\beta\Omega[\rho,\rho_\pm]}{\delta\rho_i(r)}\right|_{\bar{\rho}_\pm,\bar{\rho}} \;=\; \log\left(\frac{\bar{\rho}_i(r)}{z_i}\right) + \beta V_i(r) + q_i\bar{\phi}(r) \;=\; 0;$$
$$\left.\frac{\delta\beta\Omega[\rho,\rho_\pm]}{\delta\rho(r)}\right|_{\bar{\rho}_\pm,\bar{\rho}} \;=\; \log\left(\frac{\bar{\rho}(r)}{z}\right) + \beta V(r) + q\bar{\phi}(r) + \bar{\mu}(r) \;=\; 0,$$

where $\bar{\phi}(r) = \phi(r,[\bar{\rho},\bar{\rho}_\pm])$ and $\bar{\mu}(r) = \mu(r)|_{\bar{\rho}_\pm,\bar{\rho}}$. The packing potential $\mu(r)$ is defined as

$$\mu(r) \;=\; \Psi(\bar{\eta}(r)) + \int_{r-2a}^{r+2a} \mathrm{d}r' w(r,r')\eta(r')\Psi'(\bar{\eta}(r')),$$

with

$$\Psi'(\bar{\eta}) \;=\; \frac{\mathrm{d}\Psi}{\mathrm{d}\bar{\eta}}(\bar{\eta}) \;=\; \frac{4-2\bar{\eta}}{(1-\bar{\eta})^3}.$$

Note that in $\mu(r)$ we weight $\eta(r')\Psi'(\bar{\eta}(r'))$ and therefore we should again take care near the edges of our Wigner-cell.

Using these equations we may write the equilibrium Grand Potential as

$$\beta\Omega[\bar{\rho},\bar{\rho}_\pm] \;=\; -\int \mathrm{d}\mathbf{r}\left\{\bar{\rho}(r)\left[1+\bar{\mu}(r)-\Psi(\bar{\eta}(r))\right]+\bar{\rho}_+(r)+\bar{\rho}_-(r)+\frac{1}{2}\bar{Q}(r)\bar{\phi}(r)\right\}, \qquad (10.5)$$

with $\bar{Q}(r) = Q(r)|_{\bar{\rho}_\pm,\bar{\rho}}$. We now define the salt density, $\rho_s \equiv z_\pm$, and the initial colloid packing-fraction $\eta_0 \equiv 4\pi a_c^3\rho_c/3$, with $\rho_c \equiv z$ the initial colloid density. Using these definitions in tandem with the minimisation condition on the density profiles, the equations for the equilibrium ionic and colloidal distributions may be written as

$$\begin{aligned} \eta(r) &= \eta_0 \exp\left(-\beta V(r) - q\bar{\phi}(r) - \bar{\mu}(r)\right) && (10.6)\\ \bar{\rho}_\pm(r) &= \rho_s \exp\left(-\beta V_\pm(r) \mp \bar{\phi}(r)\right)\;. && (10.7) \end{aligned}$$

These equations together with the form of the electrostatic potential yield the Poisson Equation for Pickering emulsions

$$\nabla^2_{\mathbf{r}}\bar{\phi}(r) \;=\; -\frac{4\pi\lambda_B}{\epsilon(r)}\bar{Q}(r), \qquad (10.8)$$

with the same boundary conditions as for the saline emulsions, see section 2.5.2. Let us repeat those here for clarity.

### 10.3.2 Boundary Conditions

The boundary conditions for the Poisson Equation describing Pickering Emulsions are given by

- BC1: By radial symmetry of the problem we require that

  $$(\nabla_{\mathbf{r}}\bar{\phi})(0) \;=\; 0,$$

  i.e. there is no cusp at the origin;

- BC2: There is no free surface charge

  $$\lim_{r\uparrow a}\epsilon(r)\nabla_{\mathbf{r}}\bar{\phi}(r) \;=\; \lim_{r\downarrow a}\epsilon(r)\nabla_{\mathbf{r}}\bar{\phi}(r);$$

- BC3: The electrostatic potential is continuous everywhere, therefore it is continuous at the interface, which implies

  $$\lim_{r\downarrow a}\bar{\phi}(r) \;=\; \lim_{r\uparrow a}\bar{\phi}(r);$$

- BC4: The Wigner-Seitz cells are charge neutral, hence

  $$(\nabla_{\mathbf{r}}\bar{\phi})(R) \;=\; 0.$$

These boundary conditions together with equations (10.6), (10.7) and (10.8) form a closed set for the unknown profiles $\eta(r)$, $\bar{\rho}_\pm(r)$ and $\bar{\phi}(r)$. We will discuss the techniques required to find a solution to these equations in the last section of this chapter, but before doing so we will treat the physical quantities one can encounter in Pickering Emulsions and how to determine them from $\eta(r)$, $\bar{\rho}_\pm(r)$ and $\bar{\phi}(r)$.

## 10.4 Physical Quantities

For Pickering Emulsions we can determine the equilibrium density profiles, $\bar{\rho}_\pm$ and $\bar{\rho}(r)$, with corresponding equilibrium packing- and weighted packing-fractions $\eta(r)$ and $\bar{\eta}(r)$ respectively. From these density profiles the total local charge distribution $\bar{Q}(r)$ can be derived. We also find the electrostatic potential $\bar{\phi}(r)$. Using these profiles and potential the corresponding Grand Potential, $\Omega[\bar{\rho}, \bar{\rho}_\pm]$, can be ascertained. By subtracting the bulk ion density, $\rho_{\text{bulk}}$, and the bulk colloid density, $\rho_{c,\text{bulk}}$, Grand Potential from the Grand Potential of the local ion densities and local colloid density respectively, the surface tension can be written as $\gamma \equiv (\Omega[\bar{\rho}, \bar{\rho}_\pm] - \Omega[\rho_{c,\text{bulk}}, \rho_{\text{bulk}}])/4\pi a^2$. The functional form of the surface tension can be found by applying the above procedure to Eq. (10.5). It has not been represented here, however, because it is extremely convoluted.

Note that the presence of colloidal particles adsorbed at/wetted to the interface renders the definition of droplet charge in Part I and consequently the concept of plasma-parameter useless. We can 'extend' the definition of the droplet charge in Part I to the following

$$Z_1 = \int_0^a \mathrm{d}\mathbf{r} \left\{\bar{\rho}_+(r) - \bar{\rho}_-(r)\right\} + \int_0^{a+a_c} \mathrm{d}\mathbf{r}\bar{\rho}(r).$$

In this definition we consider the colloids adsorbed to the droplet a part of the droplet structure. This compound object will then have charge $Z_1$. The medium will have charge

$$Z_2 = \int_a^R \mathrm{d}\mathbf{r} \left\{\bar{\rho}_+(r) - \bar{\rho}_-(r)\right\} + \int_{a+a_c}^R \mathrm{d}\mathbf{r}\bar{\rho}(r),$$

where charge neutrality of the Wigner-Seitz cell implies $Z_1 = -Z_2$. However, we should realise that this definition of the droplet charge implicitly assumes the presence of a sufficiently large depletion layer between the interface and the bulk colloid denstity/crystal. Only then can we say that the colloids absorbed to the interface and the droplet truly form a single object, in the case that colloids prefer area 2. If the colloids prefer area 1, i.e. the droplet, such a problem does not exist. We will not consider droplet-droplet interactions in the case of these Pickering Emulsions.

Colloids wetting to the surface of a droplet will decrease its surface area. This effect was taken into account in the Grand Potential. As a consistency check we can determine the total area excluded from the oil-water interface by the colloids. This area should be no greater than the total droplet surface area and in fact it should be slightly smaller, because Carnahan-Starling should factor in hard-core colloid-colloid interactions. For $r \in [a - a_c, a + a_c]$ we find that the surface area excluded by the presence of a colloid at position $r$ is given by $\pi a(a_c^2 - (a-r)^2)/r$. When we have a colloid density $\bar{\rho}(r)$, the total excluded surface area per unit volume is given by $\pi a(a_c^2 - (a-r)^2)\bar{\rho}(r)/r$. Integration over the area around the interface for which colloids can contribute to the excluded volume yields

$$\begin{aligned} S &= \int_{a-a_c}^{a+a_c} \mathrm{d}\mathbf{r}\frac{\pi a}{r}(a_c^2 - (a-r)^2)\bar{\rho}(r) \\ &= \pi a \int_{a-a_c}^{a+a_c} \mathrm{d}r(a_c^2 r - (a-r)^2 r)\bar{\rho}(r), \end{aligned} \tag{10.9}$$

with $S$ the total excluded volume. Note that we expect $S/(4\pi a^2) < 1$. Suppose that the colloid density is homogeneous in the entire Wigner-cell, i.e. $\bar{\rho}(r) = \rho_c$, then Eq. (10.9) reduces to

$$S = \frac{16a^2 a_c^3 \pi^2}{3}\rho_c < \pi a^2,$$

because $\bar{\eta} < 1 \Rightarrow \rho_c < 3/4\pi a_c^3$.

## 10.5 Numerical Methods

Now that we have set up a model to describe generic Pickering Emulsions of the type observed in Ref. [3], we can proceed to discuss the numerical techniques required to solve the self-consistent set of equations in the spherical geometry. Planar calculations are also possible, we refer the reader to Ref. [5] for more information on such a planar approximation. In the previous sections we have found that the behaviour of the system is determined by solving the set of self-consistent equations (10.6), (10.7) and (10.8), i.e.

$$\begin{aligned}
\eta(r) &= \eta_0 \exp\left(-\beta V(r) - q\bar{\phi}(r) - \bar{\mu}(r)\right); \\
\bar{\rho}_{\pm}(r) &= \rho_s \exp\left(-\beta V_{\pm}(r) \mp \bar{\phi}(r)\right); \\
\nabla^2_{\mathbf{r}}\bar{\phi}(r) &= -\frac{4\pi\lambda_B}{\epsilon(r)}\bar{Q}(r),
\end{aligned}$$

with appropriate boundary conditions, see section 10.3.2. We rewrite the four above equations to two equations by substituting the ion profiles into $\bar{Q}(r)$. Doing so yields

$$\begin{aligned}
\bar{\rho}(r) &= \rho_0 \exp\left(-\beta V(r) - q\bar{\phi}(r) - \bar{\mu}(r)\right); \\
\nabla^2_{\mathbf{r}}\bar{\phi}(r) &= \kappa^2(r)\sinh\left(\bar{\phi}(r) + \phi_c(r)\right) - \frac{4\pi\lambda_B}{\epsilon(r)} Z\bar{\rho}(r),
\end{aligned}$$

where the vacuum Bjerrum length, $\lambda_B$, the Debye-length profile, $\kappa(r)$, the dielectric profile, $\epsilon(r)$, and the ionic Donnan profile, $\phi_c(r)$, are the same as in Part I. The above Poisson Equation reduces to Eq. 2.16 when the colloid density is zero. Note that we have now expressed the problem of finding the three density distributions and electrostatic potential to finding one distribution and electrostatic potential.

Let us assume that we have a non-equidistant $r$-grid, with grid points labelled $r_i$, where $i \in \{0, \ldots, N\}$ for some $N$. Suppose that we also have $j \in \{0, 1, 2, \ldots\}$, with corresponding $\bar{\rho}_j(r)$ and $\bar{\phi}_j(r)$. Let $\bar{\rho}_0(r)$ and $\bar{\phi}_0(r)$, be the initial guesses for the colloid distribution and the electrostatic potential respectively. By plugging in these initial profiles in the above equation for $\bar{\rho}$ we obtain a new colloid density, namely $\bar{\rho}_1(r)$. We then use $\bar{\rho}_1(r)$, together with the boundary conditions in section 10.3.2 to determine a new electrostatic potential, namely $\bar{\phi}_1(r)$. We then repeat this procedure until self-consistency is achieved.

On our $r$-grid the above self-consistency equations are given by

$$\begin{aligned}
\bar{\rho}_{j+1}(r_i) &= \rho_0 \exp\left(-\beta V(r_i) - q\bar{\phi}_j(r_i) - \bar{\mu}_j(r_i)\right); \\
\bar{\phi}_{j+1}(r_{i+1}) &= \frac{r_i}{r_{i+1}}\frac{r_{i+1} - r_{i-1}}{r_i - r_{i-1}}\bar{\phi}_j(r_i) - \\
&\quad \frac{2\pi\lambda_B q}{\epsilon(r_i)}\frac{r_i}{r_{i+1}}(r_{i+1} - r_i)(r_{i+1} - r_{i-1})\bar{\rho}_{j+1}(r_i) +
\end{aligned}$$

$$
\begin{aligned}
&\frac{\kappa(r_i)^2}{2}\frac{r_i}{r_{i+1}}(r_{i+1}-r_i)(r_{i+1}-r_{i-1})\sinh\left(\bar{\phi}_j(r_i)+\phi_c(r_i)\right) - \\
&\frac{r_{i-1}}{r_{i+1}}\frac{r_{i+1}-r_i}{r_i-r_{i-1}}\bar{\phi}_j(r_{i-1}),
\end{aligned}
$$

or alternatively

$$
\begin{aligned}
\bar{\phi}_{j+1}(r_{i-1}) \quad = \quad &\frac{r_i}{r_{i-1}}\frac{r_{i+1}-r_{i-1}}{r_{i+1}-r_i}\bar{\phi}_j(r_i) - \\
&\frac{2\pi\lambda_B q}{\epsilon(r_i)}\frac{r_i}{r_{i-1}}(r_{i+1}-r_{i-1})(r_i-r_{i-1})\bar{\rho}_{j+1}(r_i) + \\
&\frac{\kappa(r_i)^2}{2}\frac{r_i}{r_{i-1}}(r_{i+1}-r_{i-1})(r_i-r_{i-1})\sinh\left(\bar{\phi}_j(r_i)+\phi_c(r_i)\right) - \\
&\frac{r_{i+1}}{r_{i-1}}\frac{r_i-r_{i-1}}{r_{i+1}-r_i}\bar{\phi}_j(r_{i+1}),
\end{aligned}
$$

where $\mu_j(r_i) \equiv \mu(r_i)|_{\bar{\rho}=\bar{\rho}_j}$ and we have used $\bar{\rho}_{j+1}$ in determining $\bar{\phi}_{j+1}$ to ensure $\bar{\phi}_{j+1} \neq \bar{\phi}_j$. Our algorithm is as follows. We start with $\bar{\rho}_0$ and $\bar{\phi}_0$ then apply the above equations, where after each iteration, we 'manually' put the following alterations into $\bar{\phi}_{j+1}$ to ensure that the boundary conditions are fulfilled. Let there be a $k \neq 0, N$ such that $r_k = a$ and $r_{k+1} = a$, then these modifications are

$$
\begin{aligned}
\bar{\phi}_{j+1}(r_0) &= \bar{\phi}_{j+1}(r_1); \\
\bar{\phi}'_{j+1}(r_{k+1}) &= \frac{\epsilon_1}{\epsilon_2}\frac{\bar{\phi}_{j+1}(r_k)-\bar{\phi}_{j+1}(r_{k-1})}{r_k-r_{k-1}}; \\
\bar{\phi}_{j+1}(r_{k+1}) &= \bar{\phi}_{j+1}(r_k); \\
\bar{\phi}_{j+1}(r_{k+2}) &= \bar{\phi}_{j+1}(r_{k+1}) + (r_{k+2}-r_{k+1})\bar{\phi}'_{j+1}(r_{k+1}); \\
\bar{\phi}_{j+1}(r_N) &= \bar{\phi}_{j+1}(r_{N-1}).
\end{aligned}
$$

In addition we determine $m_1 \equiv \max(|\bar{\phi}_{j+1} + \bar{\phi}_j|)$ and $m_2 \equiv \max(|\bar{\phi}_{j+1} + \bar{\phi}_j|/|\bar{\phi}_j|)$ after each iteration. We then use the criterion $m_1$ & $m_2 \leq \delta$, with $\delta$ some small parameter, to exit the self-consistency loop.

Although the above scheme seems straightforward it is not without its pitfalls. Especially the formation of a colloidal monolayer near the interface proves numerically extremely challenging. One of the most difficult steps is to arrive at suitable initial guesses. We use the Donnan potential as the initial guess for the electrostatic potential and a step-function for the colloid density distribution, i.e. $\bar{\rho}_0(r) = \rho_c$ or 0 in area 1 or area 2, depending on which area the colloids prefer. This initial guess does give problems with the deep potential minimum in the Pieranski potential, i.e. the Boltzmann factor in the equation for $\bar{\rho}$ becomes positive and very large. To eliminate the numerical difficulties in working with such a large exponent, it proves necessary to apply a root-finding algorithm to points for which the exponent 'diverges'. Such divergences can occur for several self-consistency steps, not just the first one. Let us assume that we want to 'repair' the density distribution for the $j$-th iteration. Let $r_i$ be a grid point for which the exponent diverges during the $j$-th iteration. We keep $\bar{\phi}_j(r_i)$ fixed and solve the following equation for $\bar{\rho}_j(r_i)$

$$
\log\left(\frac{\bar{\rho}_{j+1}(r_i)}{\rho_0}\right) + \beta V(r_i) + q\bar{\phi}_j(r_i) + \bar{\mu}_j(r_i) \quad = \quad 0,
$$

by means of a false-position method root-finding algorithm. The false-position algorithm combines the secant and bisection methods to achieve relatively rapid convergence. In addition this method can be used to impose the constraint that $\forall r, \bar{\eta}(r) < 1$.

Unfortunately, repairing the density profile in this way is very time consuming, and there is no guarantee that the procedure described here will work for all system configurations. Some modifications to the initial guess can be made to increase the rate of convergence and the stability of the algorithm. Introducing a 'delta-like' spike in the initial colloid density at the location of the Pieranski potential minimum $r^*$, Eq. (10.2), for instance, will reduce the divergences our algorithm. Another way to increase stability, is to mix old and new profiles before entering another self-consistency cycle, e.g. $\bar{\phi}_{j+1} := \alpha\bar{\phi}_{j+1} + (1-\alpha)\bar{\phi}_j$, with $\alpha \in [0, 1]$. However, determining a completely stable algorithm to solve the set of self-consistent equations for reasonable system parameters is still very much an open problem in the planar geometry as well as the spherical geometry. At this point the research for the spherically geometric systems has not progressed to the point that the results in Ref. [5] can be reproduced in this geometry.

# Chapter 11

# Outlook

In the previous chapters we have formulated two models to describe Pickering Emulsions in the spherical geometry. These models are tailored to different experimentally studied systems, i.e. those of Refs. [2, 6] in the first chapter and those of Ref. [3] in the second. Of primary concern is to generate results for both of these models and examine the effects of the spherical geometry w.r.t. the planar geometry. There are theoretical avenues still left unexplored in this thesis though, in this chapter we will mention a few.

For the emulsions described in Refs. [2, 6] we can extend the model presented here to include more ion species. It is hypothesised by the group of prof. Kegel that self-dissociation of the oil in these experiments will bring the total number of ion species up to four. This will complicate matters both numerically and physically, especially when we consider a system with finite shell-parameters, $s_{\pm}$. Another effect we can discern from figure 8.1 (right B), is that for low colloid surface concentrations the colloids tend to cluster. On the one hand this means that our spherically symmetric calculation is a drastic simplification of the actual processes. Therefore, it may be interesting to investigate these systems in a non-spherical geometry, for a non-spherical surface charge distribution on the shell at $r = a + s$. Also, it can be worth while to examine the colloid-colloid interactions in the monolayer itself, to try to explain the observed clustering. Calculations for such 2D effects have been carried out, but the effects of curvature in tandem with the dielectric jump experienced by colloids wetted at the interface is yet to be investigated.

There are several improvements that can be made to make the model which describes the experiments in Ref. [3] more accurate. One of these improvements is to allow the charge of the colloids to dependent on its surroundings. In this scenario the colloid is initially charge neutral and becomes charged by being introduced in the emulsion. It is likely that the colloids become charged due to the interaction of certain molecular groups on their surface with the medium. These surface groups may, for instance, dissociate when they come in contact with the background medium, i.e. break into two charged pieces, one of which is attached to the colloid and the other is introduced into the emulsion. Such a dissociative reaction is often a chemical equilibrium, for which the surroundings determine the level of dissociation. The colloid charge can depend on the local charge density as well as the medium in which it is suspended. This type of effect has been taken under consideration in planar theory. However, doing so will add another layer of complexity to an already complicated problem.

# Bibliography

[1] S. Pickering. Emulsions. *J. Chem. Soc.*, 92:2001, 1907.

[2] S. Sacanna*, et al.* Thermodynamically Stable Pickering Emulsions. *Phys. Rev. Lett.*, 98: 158301, 2007.

[3] M. Leunissen*, et al.* Electrostatics at the Oil-Water Interface, Stability, and Order in Emulsions and Colloids. *PNAS*, 104:2585, 2007.

[4] M. Van der Heijden. Soms mengen olie en water wel, en fysici uit Utrecht weten waarom. NRC Handelsblad : Wetenschapsbijlage 04, November, 2007.

[5] J. Zwanikken and R. Van Roij. Destructed Double-Layer and Ionic Charge Separation Near the Oil-Water Interface. *Phys. Rev. Lett.*, 99:178301, 2007.

[6] S. Sacanna*, et al.* Spontaneous Oil-in-Water Emulsification Induced by Charge-Stabilized Dispersions of Various Inorganic Colloids. *Langmuir*, 23:10486, 2007.

[7] M. Bier, J. Zwanniken, and R. Van Roij. Private communication. Unpublished, 2008.

[8] M.E. Leuniss*, et al.* Ion partitioning at the Oil-Water Interface as a Source of Tunable Electrostatic Effects in Emulsions with Colloids. *Langmuir*, 24:110, 2008.

[9] S. Hamaguchi*, et al.* Triple Point of Yukawa Systems. *Phys. Rev. E*, 56:4671, 1997.

[10] O.S Vaulina and S.A. Khrapak. Scaling Law for the Fluid-Solid Phase Transition in Yukawa Systems (Dusty Plasmas). *J. Exp. and Theor. Phys.*, 90:287, 2000.

[11] D. Hornek and R. Netz. Specific Ion Adsorption at Hydrophobic Solid Surfaces. *Phys. Rev. Lett.*, 99:226104, 2007.

[12] W. Kung*, et al.* Thermodynamics of Ion Solvation and Differential Adsorption at Liquid-Liquid Interfaces and Membranes. arXiv:0710.0369v2, 2007.

[13] L. Onsager and N.N.T. Samaras. The Surface Tension of Debye-Hückel Electrolytes. *J. Chem. Phys.*, 2:528, 1934.

[14] W.L. Guest and W.C.M. Lewis. The Effect of Electrolytes upon the Interfacial Tension between Water and Dekalin (Trans-Decahydronaphthalene). *Proc. Roy. Soc. A*, 170:501, 1939.

[15] E.J.W. Verwey and J.Th.G. Overbeek. *Theory of the Stability of Lyophobic Colloids.* Elsevier Pub. Co., 1948.

[16] P. Pieranski. Two-Dimensional Interfacial Colloidal Crystals. *Phys. Rev. Lett.*, 45:569, 1980.

[17] P. Tarazona. Free-Energy Density Functional for Hard Spheres. *Phys. Rev. A*, 31:2672, 1985.

# Appendix A

# Additional Planar 106-Isolines

We have included fig. A.1 to show the construction of a plasma-parameter 106-envelope from the corresponding isolines in the planar geometry for a different droplet volume fraction than was used in the main text. As one can see, crystallisation can occur in a much larger area of parameter space for $x = 0.1$ compared to $x = 0.001$, see fig. 6.5. For the ion size ratio $a_-/a_+ \approx 0.83$ used in this thesis $\Gamma > 106$ is readily achieved in case $x = 0.1$, whereas planar theory does not predict crystallisation for $x = 0.001$. However, it should be noted that this close droplet packing is not what was observed in Ref. [3].

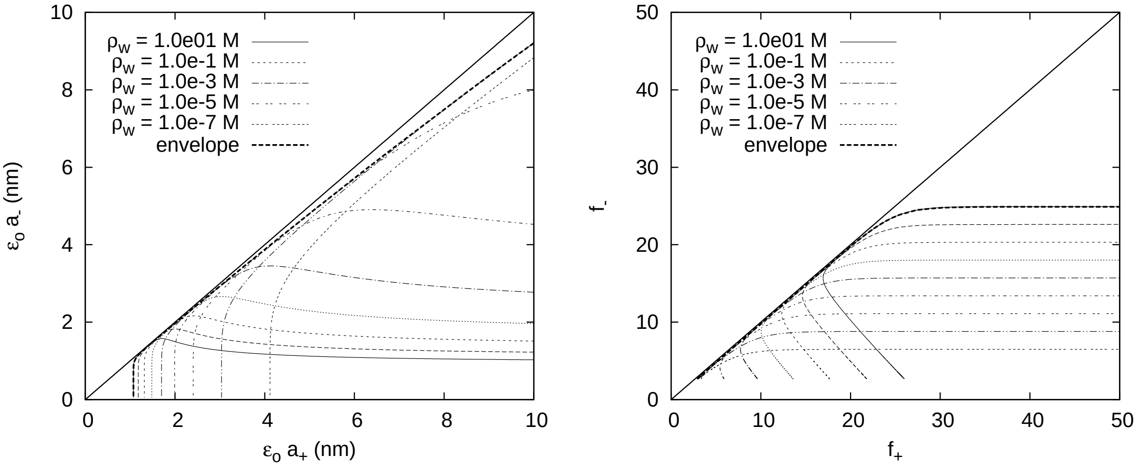

**Figure A.1:** The planar $\Gamma = 106$ isolines for $R = 10.0$ $\mu$m, $x = 0.1$ and $\epsilon_o = 5$ as a function of $a_\pm$ and $\rho_w$ (left), and as a function of the $f_\pm$ corresponding to $a_\pm$ (right). The crystallisation can occur in the area underneath each curve (left) or in the area enclosed by the curve and $f_+$-axis (right).

For completeness we have added graphs of the convex envelopes for $R = 5.0$ and $R = 15.0$ $\mu$m in fig. A.2. Note that there is no substantial difference in the behaviour of these envelope-curves w.r.t. those found in fig. 6.6. Granted, they are slightly translated, but this was to be expected. Unfortunately, allowing the Wigner-cell radius to deviate from $R = 10.0$ $\mu$m in the physically acceptable domain $[5, 15]$ $\mu$m does not produce a situation where crystallisation can occur for $a_+ = 3.6$ Å and $a_- = 3.0$ Å.

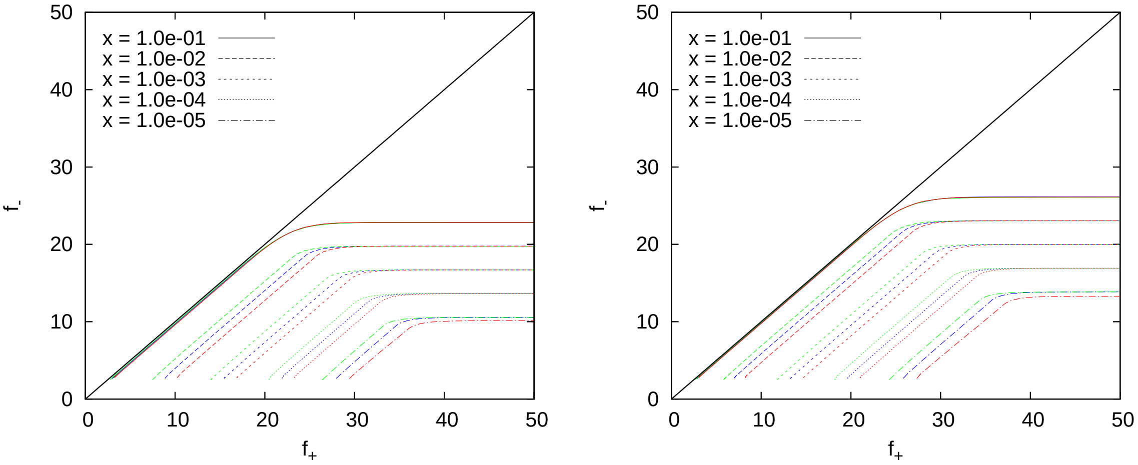

**Figure A.2:** The convex envelopes of the $\Gamma = 106$ lines for $R = 5.0$ $\mu$m (left), $R = 15.0$ $\mu$m (right), $10^{-7} < \rho_w < 10$ M, $\epsilon_o = 2.5$ (red), $\epsilon_o = 5$ (blue) and $\epsilon_o = 10$ (green) in the planar geometry. Note that there are only minor differences between the left and right graph.